



HAL
open science

Étude des volumes du liquide cérebrospinal

Alain Lebret

► **To cite this version:**

Alain Lebret. Étude des volumes du liquide cérebrospinal. Autre. Université Paris-Est, 2013. Français.
NNT : 2013PEST1088 . tel-00939308

HAL Id: tel-00939308

<https://theses.hal.science/tel-00939308>

Submitted on 30 Jan 2014

HAL is a multi-disciplinary open access archive for the deposit and dissemination of scientific research documents, whether they are published or not. The documents may come from teaching and research institutions in France or abroad, or from public or private research centers.

L'archive ouverte pluridisciplinaire **HAL**, est destinée au dépôt et à la diffusion de documents scientifiques de niveau recherche, publiés ou non, émanant des établissements d'enseignement et de recherche français ou étrangers, des laboratoires publics ou privés.



ÉCOLE DOCTORALE "MATHÉMATIQUES ET SCIENCES ET TECHNOLOGIES
DE L'INFORMATION ET DE LA COMMUNICATION"

Thèse présentée pour obtenir le grade de
Docteur de l'Université Paris-Est

Spécialité : **Signal, Image, Automatique**

Alain LEBRET

STUDY ON THE CEREBROSPINAL FLUID VOLUMES
Étude des volumes du liquide cérebrospinal

05 décembre 2013

Membres du jury :

M.	Olivier BALÉDENT	MCU-PH, Université de Picardie	(Examineur)
Mme	Isabelle BLOCH	Professeur, Télécom ParisTech	(Rapporteur)
M.	Philippe DECQ	Professeur, Université Paris 7	(Examineur)
M.	Nicolas PASSAT	Professeur, Université de Reims	(Rapporteur)
M.	Éric PETIT	Professeur, Université Paris-Est Créteil	(Directeur de thèse)

To my family

Title Study on the cerebrospinal fluid volumes

Abstract This work aims to contribute to computational methods for medical image analysis and diagnosis, especially for the study of cerebrospinal fluid volumes. In the first part, we focus on the volume assessment of the fluid spaces, from whole body images, in a population consisting of healthy adults and hydrocephalus patients. To help segmentation, these images, obtained from a recent “tissue-specific” magnetic resonance imaging sequence, highlight cerebrospinal fluid, unlike its neighborhood structures. We propose automatic segmentation and separation methods of the different spaces, which allow efficient and reproducible quantification. We show that the ratio of the total subarachnoid space volume to the ventricular one is a proportionality constant for healthy adults, to support a stable intracranial pressure. However, this ratio decreases and varies significantly among patients suffering from hydrocephalus. This ratio provides a reliable physiological index to help in the diagnosis of hydrocephalus.

The second part of this work is dedicated to the fluid volume distribution analysis within the superior cortical subarachnoid space. Anatomical complexity of this space induces that it remains poorly studied. We propose two complementary methods to visualize the fluid volume distribution, and which both produce two-dimensional images from the original ones. These images, called relief maps, are used to characterize respectively, the fluid volume distribution and the fluid network, to classify healthy adults and patients with hydrocephalus, and to perform patient monitoring before and after surgery.

Keywords medical image computing, shape analysis, classification, visualization, cerebrospinal fluid, hydrocephalus

Titre Étude des volumes du liquide cébrospinal

Résumé Cette thèse entend contribuer à l'élaboration d'outils informatiques pour l'analyse d'images médicales et le diagnostic, en particulier en ce qui concerne l'étude des volumes du liquide cébrospinal.

La première partie concerne la mesure du volume des compartiments du liquide à partir d'images corps entier, pour une population composée d'adultes sains et de patients atteints d'hydrocéphalie. Les images sont obtenues à partir d'une séquence IRM développée récemment et mettant en évidence le liquide par rapport aux structures voisines, de manière à faciliter sa segmentation. Nous proposons une méthode automatique de segmentation et de séparation des volumes permettant une quantification efficace et reproductible. Le ratio des volumes des compartiments sous-arachnoïdien et ventriculaire est constant chez l'adulte sain, ce qui permet de conserver une pression intracrânienne stable. En revanche, il diminue et varie fortement chez les patients atteints d'hydrocéphalie. Ce ratio fournit un index physiologique fiable pour l'aide au diagnostic de la maladie.

La seconde partie de la thèse est consacrée à l'analyse de la distribution du liquide dans le compartiment sous-arachnoïdien intracrânial supérieur. Il convient de souligner que ce compartiment, particulièrement complexe d'un point de vue anatomique, demeure peu étudié. Nous proposons deux techniques de visualisation de la distribution du volume liquidien contenu dans ce compartiment, qui produisent des images bidimensionnelles à partir des images d'origine. Ces images permettent de caractériser la distribution du volume liquidien et de son réseau, tout en distinguant les adultes sains des patients souffrant d'hydrocéphalie.

Mots-clés analyse d'images médicales, analyse de formes, classification, visualisation, liquide cébrospinal, hydrocéphalie

WORKPLACE

This work was conducted at:

Laboratoire Images, Signaux et Systèmes Intelligents (LISSI – EA 3956)

Université Paris-Est Créteil

61 avenue du Général de Gaulle

94010 Créteil Cedex

France

This work is also the result of a fruitful collaboration which resulted in several meetings with Dr. Jérôme Hodel (radiologist, Hôpital Saint-Joseph, Paris), and Professors Philippe Decq (neurosurgeon, Hôpital Beaujon, Clichy) and Alain Rahmouni (radiologist, Hôpital Henri Mondor, Créteil).

ACKNOWLEDGMENTS

First, I would like to express my deepest gratitude to Pr. Éric Petit for his invaluable support and patience while supervising my doctoral studies.

I want to thank Pr. Isabelle Bloch from Télécom ParisTech (UMR CNRS 5141 LTCI) and Pr. Nicolas Passat from Université de Reims Champagne-Ardennes (EA3804 CReSTIC) for having accepted to be my PhD thesis referees. I am equally grateful to Pr. Philippe DECQ from Université Paris VII (Hôpital Beaujon, Clichy / service de neurochirurgie) and Dr. Olivier Balédent from Université de Picardie Jules Vernes (Centre Hospitalier, Amiens / laboratoire BioFlow Image) for being my thesis committee members.

My thanks also belong to the members and ex-members of the LISSI laboratory who encouraged me and supported me in various ways.

Finally, this work would not have been possible without the friendly collaboration and the medical expertise from Dr. Jérôme Hodel, Pr. Philippe Decq and Pr. Alain Rahmouni.

CONTENTS

CONTENTS	xi
LIST OF FIGURES	1
LIST OF TABLES	3
1 INTRODUCTION	5
1.1 MEDICAL BACKGROUNDS AND MOTIVATIONS OF THIS WORK	5
1.2 CONTRIBUTIONS AND CONTENTS OF THIS THESIS	7
2 CEREBROSPINAL FLUID AND ITS IMAGING	9
2.1 BACKGROUNDS ON CEREBROSPINAL FLUID	11
2.1.1 Historical viewpoint	11
2.1.2 Anatomical structure of cerebrospinal fluid spaces	13
2.1.3 Physiology of the cerebrospinal fluid	16
2.2 HYDROCEPHALUS	18
2.3 IMAGING OF CEREBROSPINAL FLUID	20
2.3.1 Magnetic resonance imaging	20
2.3.2 3D-SPACE magnetic resonance imaging sequence	23
2.4 CONCLUSION	26
3 ASSESSMENT OF THE CEREBROSPINAL FLUID VOLUMES	27
3.1 INTRODUCTION	29
3.2 SEGMENTATION OF THE ENTIRE CEREBROSPINAL FLUID	30
3.2.1 Topological model of the cerebrospinal fluid	30
3.2.2 Segmentation of the entire cerebrospinal fluid volume	31
3.3 SEPARATION INTO THE CEREBROSPINAL FLUID VOLUMES	33
3.3.1 Separation of spinal and intracranial spaces	35
3.3.2 Intracranial volume separation	37
3.4 CEREBROSPINAL FLUID VOLUMES ANALYSIS	42
3.4.1 Volume assessment	42
3.4.2 Statistical analysis of volumes	44

3.5	CONCLUSION	48
4	FLUID DISTRIBUTION IN THE CORTICAL SUBARACHNOID SPACE	51
4.1	INTRODUCTION	53
4.2	RELATED WORK	53
4.3	VOLUMETRIC RELIEF MAP	54
4.3.1	Automatic positioning of a hemisphere	55
4.3.2	Voxel distribution on a hemisphere	56
4.3.3	Volumetric relief map as a two-dimensional image	56
4.3.4	Properties of volumetric relief maps	58
4.4	FLUID VOLUME DISTRIBUTION ANALYSIS	59
4.4.1	Volumetric relief map generation	60
4.4.2	Moment-based analysis of the fluid distribution	65
4.4.3	Descriptive discriminant analysis	69
4.4.4	Monitoring of patients	72
4.5	CONCLUSION	72
5	FLUID NETWORK OF THE CORTICAL SUBARACHNOID SPACE	77
5.1	INTRODUCTION	79
5.2	VOXEL LABELING BY GEODESIC PROPAGATION FROM SEEDS	80
5.3	FLUID PATHWAYS FROM SEEDS AS “FLUID SOURCES”	81
5.3.1	Seeds setting and geodesic propagation	81
5.3.2	Visualization using volumetric relief map	83
5.4	DISTRIBUTION OF DEEP FLUID PATHWAYS FROM HOMOGENEOUSLY DIS- TRIBUTED SEEDS	87
5.4.1	Seeds setting	88
5.4.2	Generating a geodesic relief map	89
5.4.3	Deep fluid pathways distribution analysis	90
5.5	CONCLUSION	93
6	CONCLUSION AND PERSPECTIVES	97
6.1	CONTRIBUTIONS	97
6.2	LIMITATIONS	98
6.3	PERSPECTIVES	98
	INDEX	100
	BIBLIOGRAPHY	103

LIST OF FIGURES

2.1	Ancient illustrations of cerebral ventricles	12
2.2	Cerebral ventricular space within brain lobes	14
2.3	Sketch of the cerebral ventricular space	15
2.4	Roof of the fourth ventricle	15
2.5	Representation of a section across the top of the cranium showing an arachnoid granulation	16
2.6	Midsagittal sketch of the ventricles, subarachnoid space, cisterns, and “bulk flow” of the cerebrospinal fluid	19
2.7	Images of the head using different magnetic resonance imaging sequences	24
2.8	Axial, coronal and sagittal cross sections of cerebrospinal fluid using the 3D-SPACE sequence	24
2.9	Whole body images using the 3D-SPACE sequence	25
3.1	Cerebrospinal fluid pathway	31
3.2	Example of simple point	33
3.3	Whole body cerebrospinal fluid segmentation process	34
3.4	Separation of intracranial and spinal regions	36
3.5	Proximity of the interpeduncular cistern to the infundibular recess of the third ventricle	37
3.6	Detection of the cerebral aqueduct in the region of interest	39
3.7	Ventricular space retrieving	40
3.8	Partial three-dimensional surface renderings of cerebrospinal fluid spaces	41
3.9	Photography of a synthetic resin phantom	43
3.10	Volume assessment for phantoms	43
3.11	Residual plots from the linear regression on clinical data	46
3.12	Distribution of the entire subarachnoid space volume relative to the ventricular volume	47
3.13	Linear discriminant analysis on $V_S \sim V_V$ for healthy adults	49

4.1	Positioning of the hemisphere	55
4.2	Steps of the volumetric relief map generation	57
4.3	Distorsion of the Lambert azimuthal equal-area projection	57
4.4	Three disks and their Gaussian digitizations	58
4.5	Volumetric relief map of a filled hemisphere	59
4.6	Preprocessing of image segmentation	60
4.7	Example of colored volumetric relief map for a healthy adult	61
4.8	Volumetric relief maps for communicating and non-communicating hydrocephalus patients	62
4.9	Volumetric relief maps for a patient before and after a surgery	63
4.10	Examples of the fluid distribution depths along some sulci	64
4.11	Examples of synthetic volumetric relief maps	66
4.12	Distribution of the centers of mass for synthetic volumetric relief maps	67
4.13	Distribution of skewnesses for synthetic volumetric relief maps	67
4.14	Distribution of the centers of mass for the clinical dataset	70
4.15	Evolution of the skewness coefficients	71
4.16	Monitoring of the centers of mass	73
4.17	Monitoring of the skewness coefficients	74
5.1	Comparison of two synthetic images with their respective colored volumetric relief maps	79
5.2	Geometric and geodesic distances between two points in the cerebrospinal fluid.	80
5.3	Voxel labeling using geodesic propagation	81
5.4	Seeds initialization	82
5.5	Single seed propagation within cerebrospinal fluid for a healthy adult	84
5.6	Multi-seeds propagation within cerebrospinal fluid for a healthy adult	84
5.7	Single seed propagation within cerebrospinal fluid for a hydrocephalus patient before and after surgery	85
5.8	Multi-seeds propagation within cerebrospinal fluid for a hydrocephalus patient before and after surgery	86
5.9	Propagation of the centers of mass	87
5.10	Propagation of orientations	88
5.11	Steps of the geodesic relief map generation	90
5.12	Comparison of the two colored geodesic relief maps of synthetic images	91
5.13	Example of colored geodesic relief map for a healthy adult	92
5.14	Geodesic relief maps for a patient before and after surgery	92

5.15	Volumetric relief maps fused with deep fluid pathways for a patient before and after surgery	93
5.16	Distribution of the centers of mass for the clinical dataset	94

List of Tables

2.1	Estimated values of $T1$ and $T2$ relaxation constants for several tissues	22
3.1	Comparison of cerebrospinal fluid volumes from different authors .	45
3.2	Optimal linear regression model for healthy adults	46
4.1	Depths of cerebrospinal fluid in main cerebral sulci	63
4.2	Orientations calculated from synthetic volumetric relief maps	68
4.3	Low order moment-based features calculated from clinical volumetric relief maps	69
5.1	Low order moment-based features calculated from clinical geodesic relief maps	93

INTRODUCTION



1.1 MEDICAL BACKGROUNDS AND MOTIVATIONS OF THIS WORK

It is widely accepted that intracranial pressure depends on the balance among the three components contained in the cranium: brain tissue, arterial and venous blood, and the cerebrospinal fluid [3]. At the end of the eighteenth century, Alexander Monro (1773–1859) described the cranium as a non expandable volume that encloses the brain considered itself as essentially incompressible [123]. He hypothesized the blood volume within the cranium remains constant. This assumption was experimentally supported in 1824 by George Kellie (1758–1829) [81]. Cerebrospinal fluid volume contribution to the intracranial equilibrium as its relationship with blood volume variations is proposed in 1848 by George Burrows (1801–1887) [17]. Nonetheless, it was not until 1926 that Harvey Cushing (1869–1939) formulated the current Monro-Kellie hypothesis, which stipulates that the sum of the brain, intracranial blood and cerebrospinal fluid volumes remains constant [29]. Except for newborn children, the adult cranium bone has low compliance [137], therefore, any sufficient volume alteration of one of the intracranial components that is not compensated by others, leads to a large change in the intracranial pressure, and may cause severe damages to brain tissues and induces various brain malfunctions.

Causes that lead to an intracranial pressure rise, called intracranial hypertension, can result from: (1) a brain volume expansion induced by an increased intracranial mass such as a tumor or cerebral edema; (2) a total blood volume increasing caused by an occlusion such as venous thrombosis, or blood effusion outside vessels, *i.e.*, hemorrhagic stroke; (3) a cerebrospinal fluid volume increasing due to an excessive production of fluid (*e.g.*, from choroid plexus papilloma) or an insufficient resorption of its outflow [163]. Similarly, an intracranial pressure fall, called intracranial hypotension, may be observed when the cerebrospinal fluid leaks from the spinal canal [152] or when spontaneous rhinorrhoea [82] or otorrhoea. Among pathologies that may cause intracranial hypertension, hydrocephalus, which results

from a disorder of the cerebrospinal fluid physiology, leads to symptomatic volume enlargement of the cerebral ventricles [134]. This said, Marmarou et al. [114] showed that the cerebrospinal fluid volume increase which induces intracranial overpressure, accounted for approximately one-third of patients.

Intracranial pressure is normally 7–15 mmHg for a supine adult at rest [1]. Its measurement is an invasive process which is performed usually by placing an intraventricular drain connected to an external pressure transducer, or by doing a lumbar puncture to collect cerebrospinal fluid and to get access to intracranial pressure variations [30, 133]. Numerous non-invasive and non traumatic techniques have been proposed in the last decade, but they remain limited to estimate the intracranial pressure [141, 147, 184].

Appeared at the end of the nineteenth century with radiography, medical imaging techniques have revolutionized the practice of medicine through advances in physics, technology and computer science. From the last three decades, medical imaging offers a great deal of information to specialists and is now closely inter-related to the clinical diagnosis of several pathologies, as well as in monitoring of therapeutic treatments [35]. For instance, the diagnosis of hydrocephalus is confirmed using imaging techniques, such as computer tomography, magnetic resonance imaging or pressure monitoring methods, to detect the enlarged ventricles and any obstruction in the fluid pathway [116, 175, 51]. In routine clinical practice, those techniques are mainly limited to the intracranial region and may require different sequences to identify a ventricular enlargement or highlight an obstruction [175]. On the other hand, the volume assessment of cerebrospinal fluid spaces is seldom achieved for many reasons: the tortuous anatomy of fluid spaces, particularly within the subarachnoid space, the complicated segmentation required when using conventional magnetic resonance imaging sequences, and thus the unreproducible results as well as a gold standard lack [144]. In particular, the subarachnoid space, *i.e.*, intracranial and spinal compartments, known to play a significant role in the regulation mechanism of intracranial pressure, is poorly studied in clinical practice [144]. Furthermore, only a few non-reproducible semi-quantitative indices, such as the index proposed by Williams Evans in 1942, are used to check the ventricular dilation [41].

Finally, the massive use of modern medical imaging techniques causes specialists to have less time for analysis as they have to handle an increasing amount of large three-dimensional image datasets [2]. Although three-dimensional images supply an impressive amount of information, their interpretation and processing

may be laborious and time-consuming when objects to analyze have a complicated shape, such as the cerebrospinal fluid within its spaces.

1.2 CONTRIBUTIONS AND CONTENTS OF THIS THESIS

This work aims to contribute to computational methods for medical image analysis and diagnosis, especially for the study of cerebrospinal fluid volumes. Concerning the input images, we use a whole body magnetic resonance imaging sequence highlighting the entire cerebrospinal fluid and recently proposed by Jérôme Hodel [67, 69]. This sequence has helped to overcome this deficiency. Until recently, no tissue-specific magnetic resonance imaging sequence have allowed to visualize the entire cerebrospinal fluid, *i.e.*, intracranial and spinal spaces. Therefore, methods based on conventional sequences usually require significant post-processing to remove surrounding structures such as cranium and brain, resulting in less reliable segmentation of the cerebrospinal fluid, especially for the subarachnoid space.

In this thesis, several methods are proposed to address previous limitations by using whole body magnetic resonance images of the cerebrospinal fluid generated from the sequence described in [67]. First, to overcome the absence of reliable methods that perform segmentation of the entire cerebrospinal fluid and support processing of large datasets, we present a robust automatic method that considers image properties and a topological constraint on the fluid shape to assess the fluid volumes. We also suggest a reliable index to describe the intracranial pressure steady state from previous volumes measurements. This part is already published in [68, 98, 96].

Secondly, the subarachnoid space has been recently considered from its dynamics viewpoint in limited regions of interest [60, 72, 91, 102], but it remains, to our knowledge, insufficiently studied from a structural point of view. To address the deficiency of studies on this space, particularly within its cortical region, we propose a fast two-dimensional visualization technique to analyze, at a glance, the fluid volume distribution within this space, which is as well applied to clinical diagnosis of hydrocephalus. This part is likewise published in [97]. We lastly complete the previous visualization technique, as such method disregards topological characteristic of the fluid, particularly within the cerebral sulci network. This additional method focuses on the fluid network within the superior cortical subarachnoid space.

This thesis is organized in five chapters. The next chapter consists of the neces-

sary background to understand the contributions of this work. We first introduce some elementary anatomical and physiological notions about the cerebrospinal fluid, and we define hydrocephalus pathology. Then, we briefly describe the whole body magnetic resonance imaging sequence that highlights the fluid and was used to produce the clinical images dataset.

The first part of this work is dedicated to the volume analysis of the cerebrospinal fluid spaces and their relationship. It corresponds to Chapter 3. We first describe methods for the entire cerebrospinal fluid segmentation and its separation into sub-volumes. Then we discuss the relationship between volumes to characterize steady state in healthy adults.

After having discussed a method to quantify the fluid volume within cortical subarachnoid space in Chapter 3, we present in the second part of this work, in Chapters 4 and 5, contributions to visualize and characterize the cerebrospinal fluid volume distribution within this space. In Chapter 4, we describe a method to visualize and analyze the cerebrospinal fluid volume distribution in the superior cortical subarachnoid space. In Chapter 5, we discuss a complementary method to study the fluid network within this space.

The conclusion and perspectives are developed in Chapter 6.

CEREBROSPINAL FLUID AND ITS IMAGING

2

CONTENTS

2.1	BACKGROUNDS ON CEREBROSPINAL FLUID	11
2.1.1	Historical viewpoint	11
2.1.2	Anatomical structure of cerebrospinal fluid spaces	13
2.1.3	Physiology of the cerebrospinal fluid	16
2.2	HYDROCEPHALUS	18
2.3	IMAGING OF CEREBROSPINAL FLUID	20
2.3.1	Magnetic resonance imaging	20
2.3.2	3D-SPACE magnetic resonance imaging sequence	23
2.4	CONCLUSION	26

IN this chapter we present the state of the art about the cerebrospinal fluid and its imaging. After describing the cerebrospinal fluid from a historical, anatomical and physiological viewpoint in Section 2.1, we then briefly define the hydrocephalus pathology in Section 2.2. Finally, in Section 2.3, we introduce the magnetic resonance imaging sequence developed to highlight cerebrospinal fluid, which we use in the following chapters.

2.1 BACKGROUNDS ON CEREBROSPINAL FLUID

Cerebrospinal fluid is a clear colorless solution that bathes the central nervous system, *i.e.*, the brain and the spinal cord. It fills the cavities within the brain called ventricles and the peripheral area of the brain and spinal cord called the subarachnoid space. The fluid circulates from ventricles where it is produced to the subarachnoid space where it is resorbed into the circulatory system [150]. Cerebrospinal fluid plays an active role in the homeostasis of central nervous system [125].

2.1.1 Historical viewpoint

A “liquid”, other than blood and which bathes the brain, is already known from ancient physicians [55, 62, 101, 126, 130]. The cerebrospinal fluid is first mentioned in the Edwin Smith surgical papyrus around 1700 BC [15]. Over a thousand years later, Hippocrates (460 BC–370 BC) described the “water” in the brain during its observations about hydrocephalus [55]. In the second century AD, the Greco-Roman physician Claudius Galenus (AD 129–*ca.* 216), also known as Galen of Pergamon, proposed a detailed description of the four ventricles and choroid plexuses, mainly from domestic animal experiments such as oxen for his brain observations, as human dissections were prohibited at this time [56]. Cerebral ventricles are then considered the seat of the mind, and the cerebrospinal fluid is assumed to transport the “pneuma”, a hypothetical vital force [28].

Anatomical studies by Galen were not challenged before the sixteenth century. Around 1504, Leonardo da Vinci (1452–1519) sketched out the ventricular space using wax injections [55, 129]. However, the first precise anatomical observations were conducted by Andreas Vesalius (1514–1564) who published *De humani corporis fabrica*, an illustrated description of human dissections [177]. Vesalius provided a more detailed description of the ventricular space and choroid plexuses as shown in Fig. 2.1, and he noted that a clear liquid collects in the ventricles [101]. In 1664, Thomas Willis (1621–1675) suggested the liquid secretion by the choroid plexuses within the ventricles [101] and postulated the fluid should drain into the venous system [4].

The modern rediscovery of cerebrospinal fluid in its entirety is credited to Emanuel Swedenborg (1688–1772) who referred to the fluid as a “spirituous lymph”. He commented on the ventricles, subarachnoid space, choroid plexuses as the fluid production sites, and fluid circulation [49, 54, 165]. Unfortunately, his accurate descriptions about cerebrospinal fluid, written around 1741–1744, were

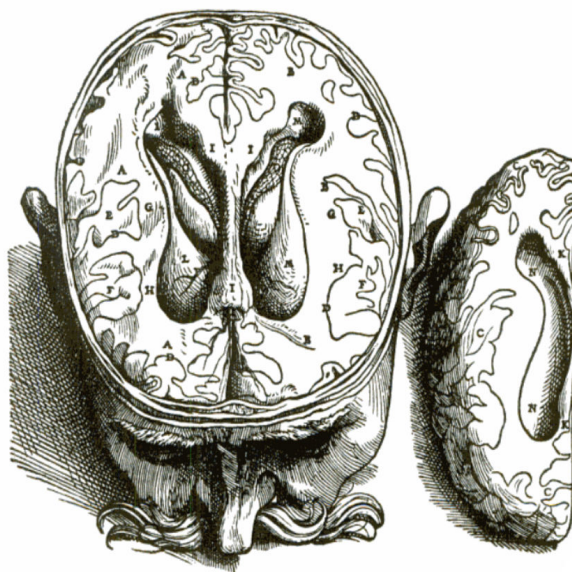


Figure 2.1 – Ancient illustrations of lateral ventricles (L,M) with the choroid plexuses (O) drawn by Andreas Vesalius in the book VII of *De humani corporis fabrica* [177].

published over a century after his death. In 1747, Albrecht von Haller (1708–1777) depicted the fluid circulation from ventricles to the venous system and to the base of the cranium and spinal cord when excess [101]. The spinal subarachnoid space was formally described in 1764 by Domenico Cotugno (1736–1822) who also showed that ventricular and spinal spaces were connected. A most accurate description of the ventricular space and its connecting pathways to the subarachnoid space was proposed by François Magendie (1783–1855) in 1827. He discovered the median aperture, also called the foramen of Magendie, on the roof of the fourth ventricle, but he stated erroneously on the flow direction of the fluid [107]. Faivre in 1854 [42] and Hubert von Lushka (1820–1875) in 1855 [174], unaware of earlier observations by Swedenborg, both suggested the choroid plexuses as sources for the fluid production; this assumption was experimentally supported in 1913 by Walter Dandy (1886–1946) [33]. Resorption of the cerebrospinal fluid through the dural venous sinuses *via* arachnoid granulations was discussed in 1876 by Ernst Key (1832–1901) and Magnus Retzius (1842–1919) [83]. However, neither choroid plexuses, nor arachnoid granulations, may be considered the only production sources, respectively resorption sites, as detailed in Section 2.1.3.

In 1891, Heinrich Quincke (1842–1922) carried out the first lumbar puncture and introduced the cerebrospinal fluid pressure notion [139], opening the way to further biophysical, biochemical and bacteriological studies on the cerebrospinal fluid [130]. Accordingly, in 1911, William Mestrezat (1883–1928) first established the accurate biochemical composition of the fluid in his doctoral thesis [120]. In 1943, John O’Connell performed the first intracranial pressure measurement by

connecting a pressure gauge to the output of a lumbar tap [127]. He noted the relationship between cerebral arterial pulsations and pulsatile movement of the cerebrospinal fluid and referred to a “cerebrospinal fluid pump.”

Radiography techniques emerged with the use of X-rays [146] under clinical conditions [77]. Coupled with other techniques such as gaseous, iodized or isotopic contrast agent injections using lumbar puncture, first radiographies allowed prodigious neuroradiological investigations in this early twentieth century. However, most techniques are highly invasive and traumatic, such as ventriculography, developed by Dandy in 1918, which consists in taking a radiography of the ventricles, emptied of their fluid, and filled with air [32].

Most of these invasive and traumatic methods were abandoned for the benefit of new imaging techniques such as magnetic resonance imaging. Between 1946 and 1950, Bloch, Purcell and Hahn established general principles of magnetic resonance imaging by using the magnetic properties of aqueous structures [13, 61, 138], and in 1955, Obledad verified its application to biological tissues [128].

2.1.2 Anatomical structure of cerebrospinal fluid spaces

The cerebrospinal fluid is divided into an internal space, *i.e.*, the ventricular space and the central canal, and an external one called the subarachnoid space. The thin epithelial membrane that lines the inner wall of the cavity is sealed, forming a biological barrier between the liquid and nervous tissues.

Ventricles

The ventricular space consists of a series of cavities within the brain, lined by ependyma and filled with cerebrospinal fluid. It includes four cerebral ventricles, namely, the two lateral ventricles, the third ventricle and the fourth ventricle.

The two lateral ventricles are symmetric cavities in both cerebral hemispheres. Each lateral ventricle has a central part above the thalamus and three horns: the frontal horn in the frontal lobe, the temporal horn in the temporal lobe and the occipital horn in the occipital lobe as depicted in Fig. 2.2. Paired lateral ventricles communicate with the midline third ventricle through the two interventricular foramina (or *Monro foramina*), which are on each side in front of the two thalamus as illustrated in Fig. 2.3.

The third ventricle is a cavity laterally clamped between the thalamus and hypothalamus. One can see the supraoptic and infundibular recesses at its frontal part and the suprapineal and pineal recesses at its posterior part. It communicates

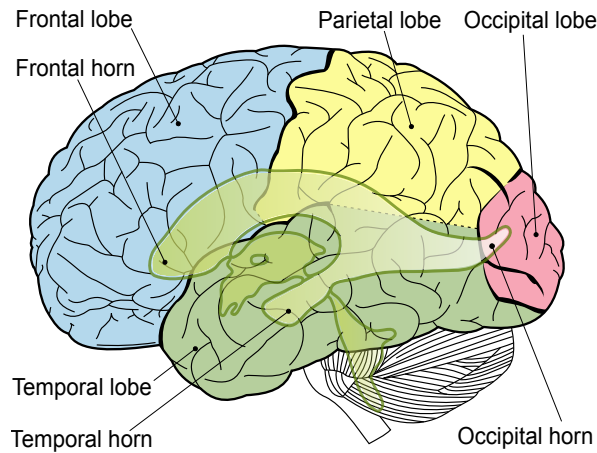


Figure 2.2 – *Cerebral ventricular space within the brain lobes (Modified from Henri Gray. Anatomy of the Human Body. Lea & Febiger, Philadelphia, 1818 [53]).*

with the fourth ventricle through the cerebral aqueduct (or aqueduct of Sylvius). The cerebral aqueduct is a thin “tubular structure” (diameter: 1 to 3 mm; length: around 14 mm) which connects the third ventricle to the superior corner of the fourth ventricle as illustrated in Fig. 2.3 [78]. Because of its narrowness and surrounding structures as shown in Fig. 2.4, the aqueduct is a weak point of the ventricular space because any constriction may affect the cerebrospinal fluid circulation.

The fourth ventricle, posterior to the pons, is covered with the cerebellum on its posterior part as illustrated in Fig. 2.4. The ventricle is connected to several cisterns of the subarachnoid space through the median aperture (or foramen of Magendie) that is posterior to the pons [20], and through the two smaller symmetric openings called lateral apertures (or foramina of Luschka). In direct contact with the cerebellum, the fourth ventricle is submitted to the cerebellum expansion in case of tumor, it can be also compressed or obstructed.

Subarachnoid space

The pia mater inside and the arachnoid mater outside delimit the subarachnoid space as illustrated in Fig. 2.5. The space is narrow over the brain convexity and it has several wider regions, called cisterns, at the base of the brain. The larger cistern is the posterior cerebellomedullary cistern (or cisterna magna) enclosed between the cerebellum and the dorsal surface of the medulla oblongata as shown in Fig. 2.4. This cistern drains the cerebrospinal fluid from the fourth ventricle through the median aperture. The pontocerebellar cistern is on the ventral aspect of the pons and receives cerebrospinal fluid from the fourth ventricle through both lateral apertures. The corner formed by the diencephalic floor, cerebral peduncles

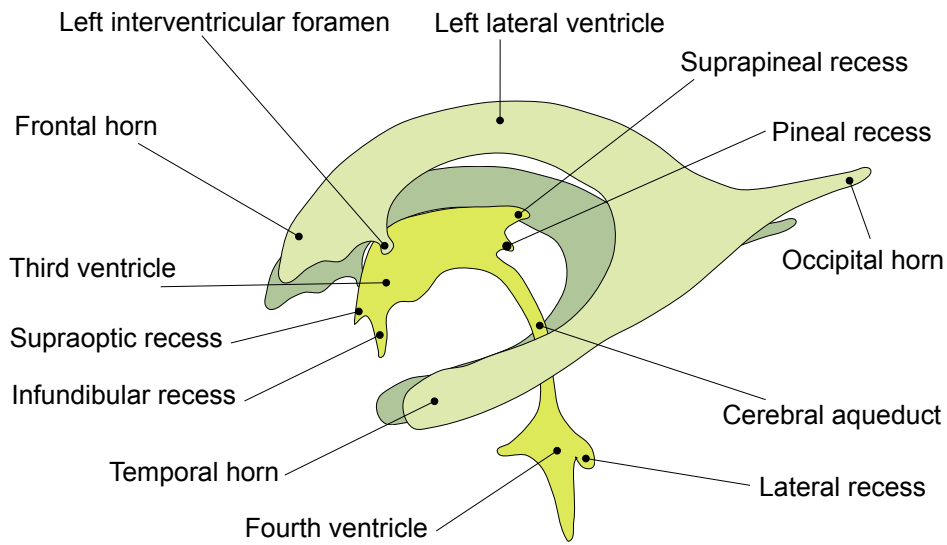


Figure 2.3 – Sketch of the cerebral ventricular space.

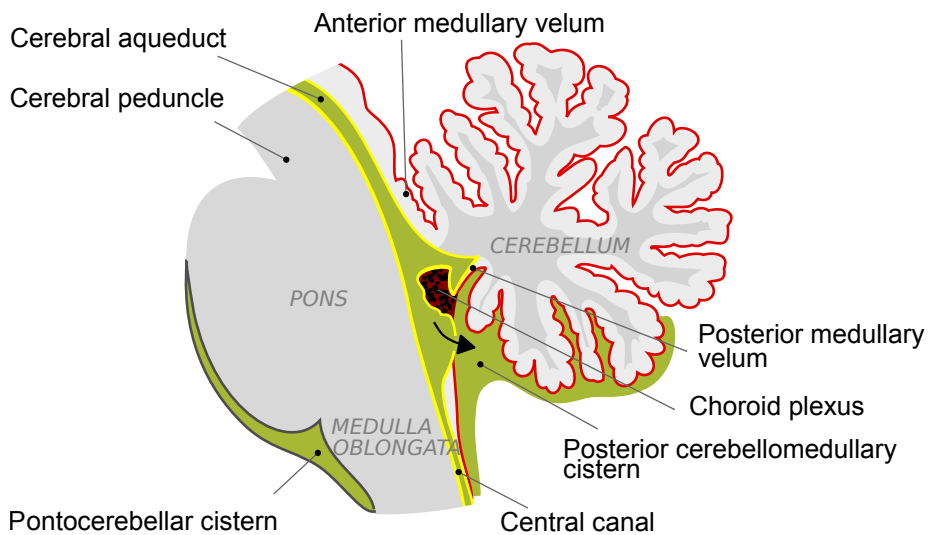


Figure 2.4 – Roof of the fourth ventricle (Modified from Henri Gray. *Anatomy of the Human Body*. Lea & Febiger, Philadelphia, 1818 [53]). The ependymal lining of fourth ventricle appears in yellow, and the arrow indicates the median aperture.

and pons, locates the interpeduncular cistern as illustrated in Fig. 2.6. The cerebellar surface, the quadrigeminal plate and the pineal body, delimit the quadrigeminal cistern as shown in Fig. 2.6 [66]. Arachnoid granulations that protrude through the dura mater into the intradural vein or superior sagittal sinus finally take part to the resorption of the cerebrospinal fluid to the venous system as illustrated in Fig. 2.5 and 2.6.

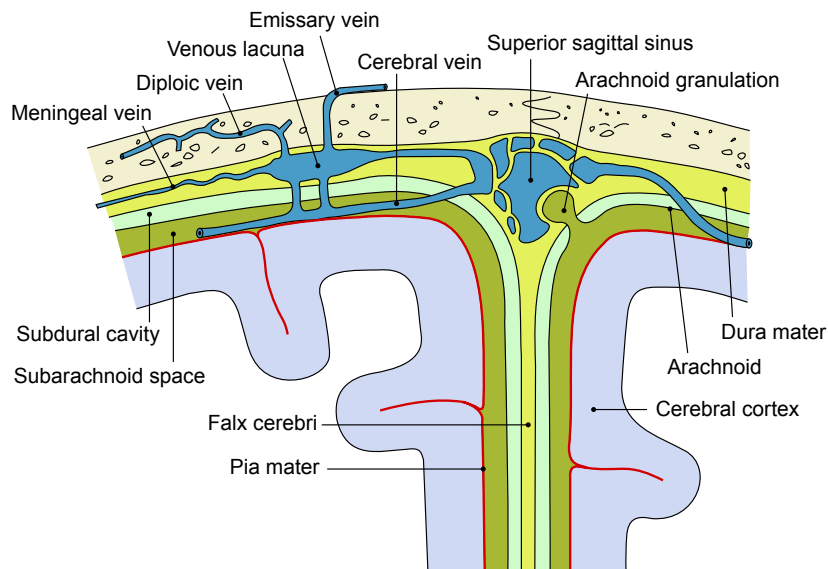


Figure 2.5 – Representation of a section across the top of the cranium, showing membranes around the brain and an arachnoid granulation (Modified from Henri Gray. *Anatomy of the Human Body*. Lea & Febiger, Philadelphia, 1818 [53]).

2.1.3 Physiology of the cerebrospinal fluid

Functions

The cerebrospinal fluid behaves as a viscous fluid with a density ($\simeq 1000 \text{ kg/m}^3$) and a viscosity ($\simeq 1,02 \cdot 10^{-3} \text{ Pa}\cdot\text{s}$) close to those of water. Thus, the fluid acts as a buoyant support to the central nervous system as it reduces the effective weight of the brain ($\simeq 1400 \text{ g}$) to approximately 25 g [125].

Cerebrospinal fluid has also a mechanical protection function. By encompassing the central nervous system in its entirety, the fluid protects the brain from direct contact with the cranium, especially in case of impact. On the other hand, in the spinal region, the fluid rather supplies as a lubricant that facilitates movements of the spine.

In addition, the cerebrospinal fluid has a transporter role. In direct contact with the meninges and ependyma, the fluid provides them nutrient and participates in their excretion by being renewed every six to eight hours each day. The fluid also

contributes to the transit of lymphocytes, plasmocytes and immunoglobulins, as well as hormones and neuromediators [160] involved in immune and hormonal functions of the central nervous system.

Lastly, the cerebrospinal fluid operates as a homeostasis controller. The fluid contacting the interstitial fluid through cell barriers acts as a lymphatic circuit that filters nutrients from the blood and carries them into the cells of the brain and spinal cord, and *vice versa* [76, 150].

Composition

Cerebrospinal fluid is a watery solution composed of 99% of water which carries electrolytes (Na^+ , K^+ , Ca^{2+} , Mg^{2+} , Cl^- , HCO_3^-) and molecules such as urea, glucose (60–80% of blood glucose), amino acids, and various proteins [125]. The spinal composition of cerebrospinal fluid presents a higher protein concentration due to the greater permeability of the blood brain barrier in the lumbar region and a lower glucose one [176].

Disease modifies the cerebrospinal fluid biochemistry and enables its analysis [76, 130, 176]. For instance, the distinction of different types of meningitis can be completed by analyzing variations of glucose levels [176] and levels of tau proteins are correlated with Alzheimer's disease [12].

Volume of the cerebrospinal fluid

In 1839, Magendie indicated that the total cerebrospinal fluid weight varies between two and five ounces, which corresponds to range from 57 to 142 g, *i.e.*, a volume range from 57 to 142 cm³. These measurements were obtained from dissections a few hours after death and without specifying whether they were adults or not [107].

Current values in the literature show that, in humans, the total cerebrospinal fluid volume is estimated to about 40–50 cm³ in neonates, 65–140 cm³ in children and 140–170 cm³ in young adults [26]. We will see in Section 3.4.1 that using modern imaging techniques have significantly expanded ranges of the total fluid volume in adults. Finally, several authors confirm that the ratio of cerebrospinal fluid volume to brain volume increases in aging [76, 89, 117, 118, 124, 159, 167, 169], and most predominantly in the subarachnoid space than in ventricles [169].

Production and resorption of cerebrospinal fluid

A dynamic balance between the cerebrospinal fluid production by choroid plexuses and the resorption through arachnoid granulations maintains the total volume of cerebrospinal fluid constant. The cerebrospinal fluid flow from production to resorption sites is called “bulk flow”. This flow has to be distinguished from the fast pulsatile flow of the fluid, which is related to the cerebral arterial pulsations [127] and to the pulsed expansion and contraction of the choroid plexuses [9]. Since observations by O’Connell in 1943, numerous studies have considered pulsatile movements of the cerebrospinal fluid [91, 103, 180]. However, we will restrict our considerations to the bulk flow in the present work. Figure 2.6 illustrates the bulk flow of the cerebrospinal fluid from the ventricular space to the subarachnoid space.

The cerebrospinal fluid has a slow circulatory movement from ventricles to the cortical subarachnoid space. The spinal subarachnoid space can be considered as a “flushing chamber” [5] that is involved in approximately 32% of the system compliance by the elastic capacity of the epidural venous system [115], and participates to around one-fourth to the cerebrospinal fluid clearance [14].

For most authors, choroid plexuses are the principal production sites of the fluid for about two-thirds of the total production [76]. However, relative contributions of extrachoroidal sources remain controversial [131]. At the spinal level, most authors agree on the lack of sources. Similarly, there are several resorption sites. However, arachnoid granulations are recognized as the central site for the cerebrospinal fluid resorption [79].

It is estimated that $0.35\text{--}0.40\text{ cm}^3/\text{min}$ or approximately $500\text{ cm}^3/\text{day}$ of cerebrospinal fluid is produced, resulting in the complete renewal of the fluid about four to five times a day in young adults [76, 150]. A reduction of this turnover rate to three times a day can be observed in the elderly, mainly due to brain atrophy and increased total volume of cerebrospinal fluid [150].

2.2 HYDROCEPHALUS

It is widely accepted that hydrocephalus refers to an abnormal accumulation of cerebrospinal fluid within the cerebral ventricles [26, 132, 142]. Since classification proposed by Dandy and Blackfan [33] in 1913, most authors agree to the two main types of hydrocephalus: “communicating” and “obstructive or non-communicating”. Both types of hydrocephalus are related to a fluid flow restriction

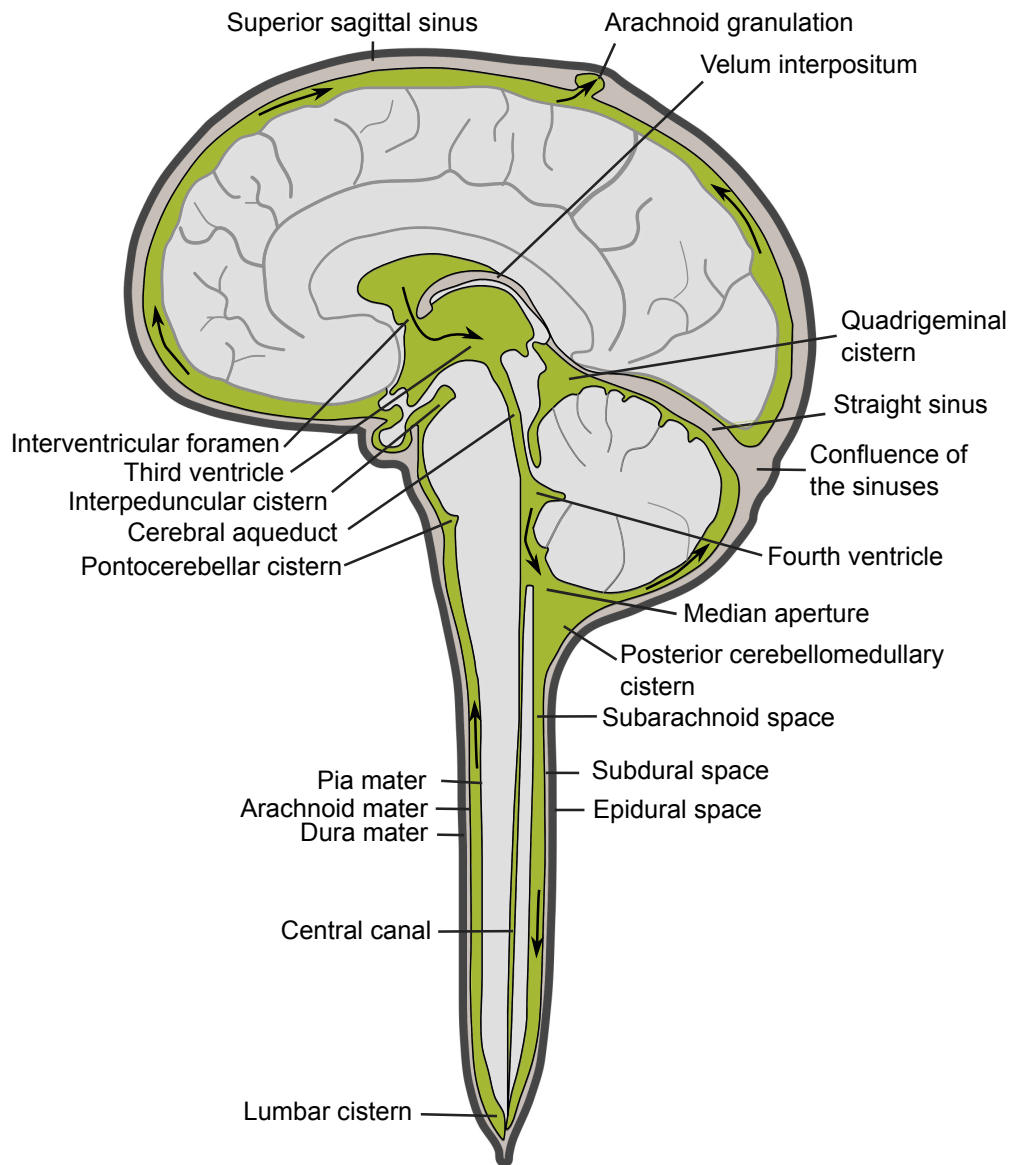


Figure 2.6 – Midsagittal sketch of the ventricles, subarachnoid space, and cisterns. Arrows indicate the normal direction of the cerebrospinal fluid “bulk flow”.

between secretion sites and resorption ones, which usually leads to increasing of the total ventricular volume.

Communicating hydrocephalus is characterized by disturbance of the flow in the subarachnoid space. However, cerebrospinal fluid communicates freely between ventricular and subarachnoid spaces. This may be caused by an obstruction in pathways which follow cisterns (*e.g.*, after acute inflammation of meningeal origin), or in resorption sites (*e.g.*, arachnoid granulation fibrosis). First described by Hakim and Adams [63], normal pressure hydrocephalus, or “idiopathic adult hydrocephalus syndrome”, is a communicating hydrocephalus related to age. It is defined by the association of a cerebral ventricles dilation and suggestive symptoms such as gait disturbance, dementia and urinary incontinence [158]. However, its pathophysiology is still debated.

By contrast, non-communicating hydrocephalus is characterized by an obstruction in the ventricular space that prevents the cerebrospinal fluid from passing into the subarachnoid space, and causes an important intracranial overpressure [26]. This may result from an intraventricular obstruction associated with a tumor development or an aqueductal stenosis.

While hydrocephalus cases were regularly described since Hippocrates, the first effective therapy was proposed in 1882 by Carl Wernicke (1848–1905) who pioneered sterile ventricular puncture and external cerebrospinal fluid drainage to treat hydrocephalus [4]. Most modern techniques currently used to treat hydrocephalus, carry out the installation of an external ventricular drain in an emergency, and that of a ventriculo-peritoneal shunt in other cases [26, 116, 175].

2.3 IMAGING OF CEREBROSPINAL FLUID

Magnetic resonance imaging is the reference technique for the cerebrospinal fluid imaging. After reminding some basis, we introduce the sequence used to produce whole body images of cerebrospinal fluid.

2.3.1 Magnetic resonance imaging

Magnetic resonance imaging is a non-invasive imaging technique primarily used in the medical field, which produces high quality images of the human body. Based on the nuclear magnetic resonance principle [52], magnetic resonance imaging occurred in the latter half of the seventies, following works of Lauterbur and Mansfield (using of a gradient field for spatial localization) [95, 112], Ernst (using Fourier

transform for image reconstruction) [90] and Damadian (making his investigations in the medical field) [31]. Magnetic resonance imaging allows to observe various tissues, with an high contrast, by using several types of sequences. For further details about magnetic resonance imaging, readers should refer to Bushberg et al. [18] for physical issues and to Kastler et al. [80] for more technical ones.

Principle

The principle of magnetic resonance imaging is to expose biological tissues to a strong magnetic field (usually 1.5 T or 3 T) to measure their magnetization, and then to build an image from these measurements. Magnetization is mainly induced by magnetic properties of hydrogen atoms, *i.e.*, protons in their ionic state, found abundantly in each biological tissue.

The strong magnetic field is used to align initially the hydrogen atoms magnetization (“spins”) in a common direction. Then, a radio frequency signal produced by an external antenna shifts magnetization by a flip angle with respect to the common direction (excitation step). When the radio frequency signal is turned off, spins return to their original position by emitting a radio frequency signal, which can be recovered by the same antenna (relaxation step).

The nuclear magnetic resonance signal cannot directly locate sources because the dimensions of objects of interest are usually smaller than the signal wavelength (a few meters for a magnetic field of 1.5 T or 3 T). Spatial position of the atoms is then obtained by adding a directional magnetic field gradient. Use of this gradient provides different relaxation steps for “slices” of protons which depend on gradient. Finally, signal processing techniques based on fast Fourier transform algorithms are used to locate sources (*i.e.*, their spatial frequency information, frequency and phase, are stored in the k -space) to build an image [50].

T_1 and T_2 modalities

One defines repetition time (TR) as the time between two excitation steps, and the echo time (TE) as the time between excitation and the nuclear magnetic resonance signal. After excitation, nuclei tend to return to their equilibrium position (relaxation step). This relaxation step can be divided into two phenomena: the longitudinal relaxation time (T_1), which indicates the time required to regain longitudinal magnetization, and the transverse relaxation time (T_2), which measures the time for the resonating protons to remain coherent after the radio frequency pulse. These relaxation times vary according to the specific physicochemical water organization in tissues.

A magnetic resonance imaging sequence is a set of excitation pulses whose parameters (TE , TR) are adjusted to get well-contrasted images by modifying values of $T1$ and $T2$. Thus, in $T1$ -weighted images ($TE=10\text{--}20$ ms and $TR=400\text{--}600$ ms), fat tissues appear hyperintense (bright grayscale) and water appears hypointense. By contrast, in $T2$ -weighted images ($TE > 80$ ms and $TR > 2000$ ms), water appears hyperintense while fat tissues are darker than water. Table 2.1 summarizes estimated values of $T1$ and $T2$ for different tissues.

Tissue	$T1$ in 0.5 T (ms)	$T1$ in 1.5 T (ms)	$T2$ in 1.5 T (ms)
cerebrospinal fluid	1800	2400	160
gray matter	650	900	100
white matter	500	780	90
fat	210	260	80
muscle	550	870	45

Table 2.1 – Estimates values of $T1$ and $T2$ relaxation constants for several tissues (from Bushberg *et al.* The essential physics of medical imaging. Lippincott Williams & Wilkins, Philadelphia, 2nd edition, 2002).

Sequences

Most of the magnetic resonance imaging sequences are based on gradient echo and spin echo sequences. Gradient echo sequences allow fast imaging and low flip angle that is well-adapted to the $T1$ -weighted modality, and require less radio-frequency power. However, they are inappropriate to generate well $T2$ -weighted contrast and are sensitive to the main magnetic field inhomogeneities as to susceptibility effects. By contrast, spin echo sequences have a high signal to noise ratio and are truly $T2$ -weighted, although they are less fast for scanning and more power-consuming.

First described by Erwin Hahn [61] in 1950, the spin echo sequence consists in refocusing spin magnetization using pulses. The sequence includes a “slice selective” 90° pulse applied in conjunction with a “slice selection” gradient, followed by one or more 180° refocusing pulses. Turbo spin echo is a conventional spin echo variant in order to save time by a given factor which is determined by the “turbo factor” parameter. In recent works, turbo spin echo sequences were used with variable refocusing angles [19], which allow large echo trains, with shorter inter-echo spacing and higher turbo factors, to produce thin slices within a short time [119].

2.3.2 3D-SPACE magnetic resonance imaging sequence

One aim of the doctoral work by Jérôme Hodel [67, 68, 69] was to achieve a fast whole body tissue-specific imaging sequence that highlights the cerebrospinal fluid, and is as insensitive as possible to vascular and cerebrospinal fluid flows.

The magnetic resonance sequence used to generate the clinical “whole body” image dataset is a $T2$ -weighted turbo spin echo sequence variant using variable flip-angles, called 3D-SPACE (Sampling Perfection with Application optimized Contrast using different flip-angle Evolution). Unlike fixed refocusing pulses of 180° of the conventional fast spin echo sequence, the 3D-SPACE sequence uses a pulse train with variable angles of refocusing pulses.

High values of TE are required to obtain a liquid-weighted signal. However, by increasing TE , signal drops and motion artifacts increase. The optimal TE was chosen at 762 ms as the best compromise between signal intensity and sensitivity to motion artifacts.

Magnetic resonance “whole body” images used for the assessment of fluid volumes in Chapter 3 were acquired in the sagittal plane on a 1.5 T system (Magnetom Avanto; Siemens Medical Solutions, Erlangen, Germany). The sequence was configured as follow: repetition time TR (ms)/echo time TE (ms) of 2400/762; turbo factor of 141; 250×250 mm field of view; 256×256 acquisition matrix; voxel size (mm^3) of $1 \times 0.98 \times 0.98$; number of excitations 1.4 (only central region of the three-dimensional k -space was resampled for the second time, and this second acquisition only covered 40% of the entire k -space); 160 slices for head station that may be reduced to 70 slices for each spinal station to accelerate acquisition; acquisition time, 9 to 12 min according to the heart rate for the whole body acquisition. More controls and patient acquisitions, limited to the intracranial region, were also performed using the same sequence configuration (acquisition time: 3 min) to analyze the cortical subarachnoid space in Chapters 4 and 5.

Figure 2.7 shows midsagittal cross-sections of magnetic resonance images using conventional $T2$ -weighted sequence (a) and 3D-SPACE sequence (b). Both images can highlight the cerebrospinal fluid, but for the conventional $T2$ -weighted sequence, neighboring structures of the fluid provide many details and require more complicated segmentation than the 3D-SPACE one.

Different intracranial cross-sections of the 3D-SPACE sequence are shown in Fig. 2.8, and a whole body midsagittal cross-section image example is presented in Fig. 2.9. The contrast-enhanced view in Fig. 2.9(b) brings out deficiencies of the sequence, which has the disadvantage of being sensitive to noise and artifacts, especially motion artifacts.

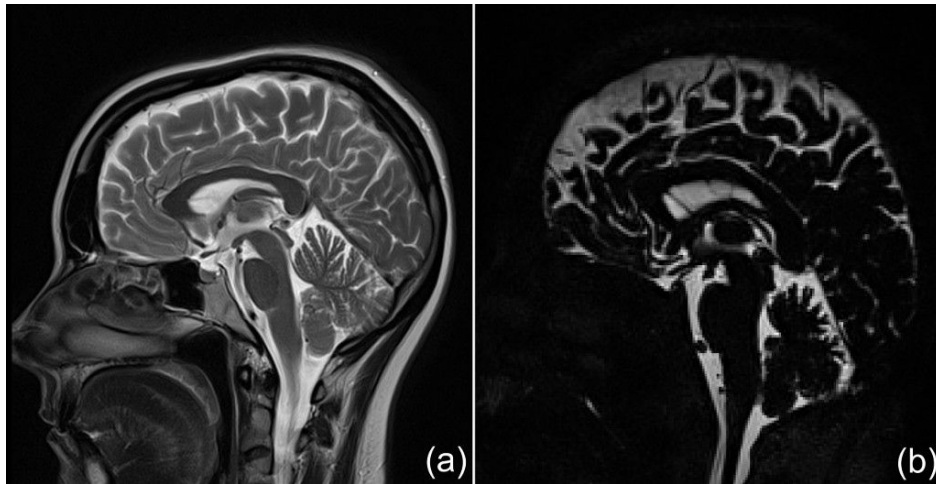


Figure 2.7 – Comparison of images of the head (midsagittal cross-section) by using different magnetic resonance imaging sequences: (a) conventional T2-weighted sequence; (b) 3D-SPACE sequence

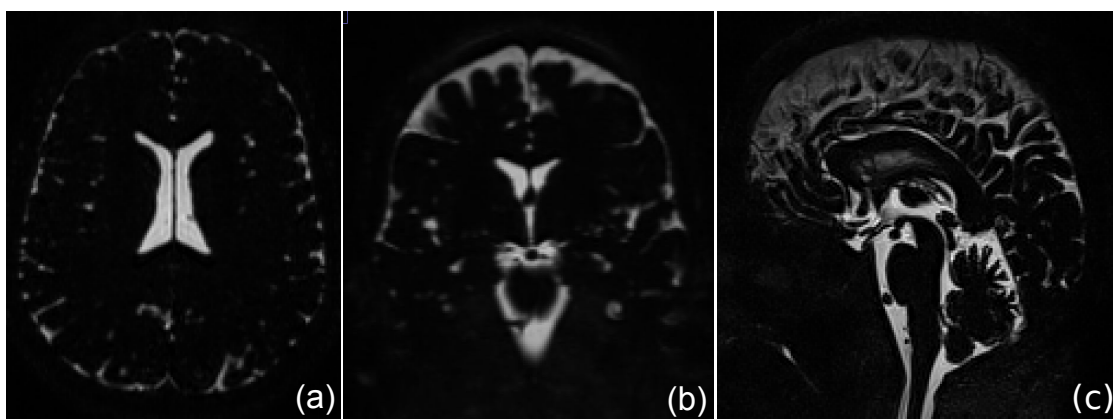


Figure 2.8 – Intracranial images using the 3D-SPACE sequence (axial, coronal and sagittal cross-sections). Note the extremely low signal from structures other than cerebrospinal fluid.



Figure 2.9 – Whole body images (sagittal view) using the 3D-SPACE sequence: (a) original image; (b) contrast-enhanced image.

2.4 CONCLUSION

In this chapter, we have introduced cerebrospinal fluid as a watery solution contained within the cavities of the brain, called ventricles, and in the subarachnoid space that surrounds the entire central nervous system. Fluid circulates from ventricles to the subarachnoid space, and any impediment in its circulation may result in a significant increase of the intracranial pressure and hydrocephalus. We have also presented the magnetic resonance imaging sequence that highlights the fluid. This sequence has allowed clinical “whole body” and intracranial images we use in the following chapters.

ASSESSMENT OF THE CEREBROSPINAL FLUID VOLUMES

CONTENTS

3.1	INTRODUCTION	29
3.2	SEGMENTATION OF THE ENTIRE CEREBROSPINAL FLUID	30
3.2.1	Topological model of the cerebrospinal fluid	30
3.2.2	Segmentation of the entire cerebrospinal fluid volume	31
3.3	SEPARATION INTO THE CEREBROSPINAL FLUID VOLUMES	33
3.3.1	Separation of spinal and intracranial spaces	35
3.3.2	Intracranial volume separation	37
3.4	CEREBROSPINAL FLUID VOLUMES ANALYSIS	42
3.4.1	Volume assessment	42
3.4.2	Statistical analysis of volumes	44
3.5	CONCLUSION	48

IN this chapter we present segmentation and separation methods of the cerebrospinal fluid volumes from whole body magnetic resonance images of the fluid previously introduced.

The work exposed in this chapter was presented during the SPIE Medical Imaging 2012 conference, held in San Diego, CA, USA. A conference article was published in [98] and an extended version was published in Computerized Medical Imaging and Graphics [96].

3.1 INTRODUCTION

As mentioned in previous chapters, the measurement of cerebrospinal fluid volumes is an indirect way to evaluate intracranial pressure. Thus, since the use of modern imaging techniques such as magnetic resonance imaging, many studies have attempted to quantify the fluid volumes in a reproducible manner.

Several intracranial fluid volume quantifications were carried out over the last 25 years, mostly using $T2$ -weighted magnetic resonance imaging sequences and semi-manual methods. Cerebrospinal fluid volume were assessed for healthy adults using $T2$ -weighted magnetic resonance imaging sequences in [11, 24, 69, 87, 117, 167, 173, 186], $T1$ -weighted sequences in [89, 99] and a multi-modality technique in [106]. Volume assessments were performed for patients with various types of hydrocephalus using $T2$ -weighted sequences in [24, 69, 87, 117, 173, 186], whereas it was limited to normal pressure hydrocephalus in [85, 135]. However, all of them are restricted to the intracranial region while Edsbagge et al. [38] shown that the spinal subarachnoid space volume may also provide some clues in hydrocephalus analysis, and is nevertheless poorly analyzed [38, 70, 164]. Moreover, except in [24, 69] images reveal most cerebral structures, which do not facilitate segmentation of the fluid itself in a routine way. We summarize and discuss these results in Table 3.1, Section 3.4.1.

The aim of this first part is to provide both a method to assess volumes of the entire cerebrospinal fluid in order to provide reference values for future studies, and an aid to diagnose hydrocephalus. To quantify the fluid volumes from the whole body images introduced in Chapter 2, we propose automatic segmentation of the entire cerebrospinal fluid and its separation into spinal subarachnoid, cortical subarachnoid and ventricular spaces. We also show the ability of this volume assessment to be exploited to perform statistical analyses, which lead to a functional parameter calculated by the ratio of the entire subarachnoid space volume to the ventricular one. We assume this parameter could be efficient to discriminate healthy adults from patients affected by communicating and non-communicating hydrocephalus. Furthermore, this approach only requires a single imaging sequence and an automatic image processing for each patient.

Concerning the segmentation method, we should consider the complex geometry of the cerebrospinal shape and its human variability, the presence of noise and artifacts, especially motion artifacts [39], and the possible obstructed fluid pathway, which results in a disconnection of the fluid spaces in non-communicating hydrocephalus cases. To overcome these problems, we introduce a topological assumption on the entire cerebrospinal fluid shape. This property, used as a refine-

ment constraint, brings both accuracy and robustness to the segmentation method, particularly for pathological cases. The separation method of the previously segmented total fluid volume involves a region of interest defined from eyeballs. Spinal and intracranial spaces are separated by detecting a topological change of the fluid in the bottom part of the region of interest. Then, the ventricular space is separated from the intracranial space by reconstructing the ventricles from a particular tubular structure. All these steps are configured with default values that we specified and can be chained without requiring any user interaction. Some steps may be even parallelized (*e.g.* the two separation methods).

3.2 SEGMENTATION OF THE ENTIRE CEREBROSPINAL FLUID

Input whole body images produced by using 3D-SPACE sequence appear to be binary due to the poor dynamic of the luminance perception of the human visual system but, in fact, they are not as shown in Fig. 2.9(b) and 3.3(a). Images only partially attenuate neighboring structures and they are disturbed with Rician noise [58] and motion artifact residues [162]. However, Rician noise removal methods [27, 182] remain inappropriate to filter such images since they remove a lot of information and tend to disconnect the fluid in several thin regions. We thus use image properties and a topological assumption on the fluid shape for segmenting the entire cerebrospinal fluid volume.

3.2.1 Topological model of the cerebrospinal fluid

Numerous studies have demonstrated the effectiveness to integrate topological constraints in medical image processing, particularly in neuroimaging [6, 7, 36, 64, 108, 110, 122, 148, 154]. For instance, most brain structures have the topology of a filled or hollow sphere while their geometry is complex. We consider the entire fluid to be topologically equivalent to a filled sphere that is compliant with the fluid flow as illustrated in Fig. 3.1. Various authors use advanced models such as a hollow sphere in Rueda et al. [148], nested concentric spheres in Mangin et al. [110], Miri et al. [122], or a more complex object with two internal handles caused by the two lateral apertures in Bazin and Pham [7]. Models closest to reality as in [7] are well adapted to address problems such as surface correction. Nonetheless, the two lateral apertures remain disconnected from the fourth ventricle or the pontocerebellar cistern when we perform the initialization step in Section 3.2.2. The filled sphere model is, therefore, a suitable compromise which significantly sim-

plifies and accelerates the initialization step compared to that of a hollow sphere while the difference between the two resulting volumes is negligible ($< 0.33\%$ of the total volume in the worst case). Furthermore, it introduces neither unexpected cavity nor handle despite the noise and artifacts, and is also more efficient and consistent for hydrocephalus patients for whom the fluid do not fit a hollow sphere anymore.

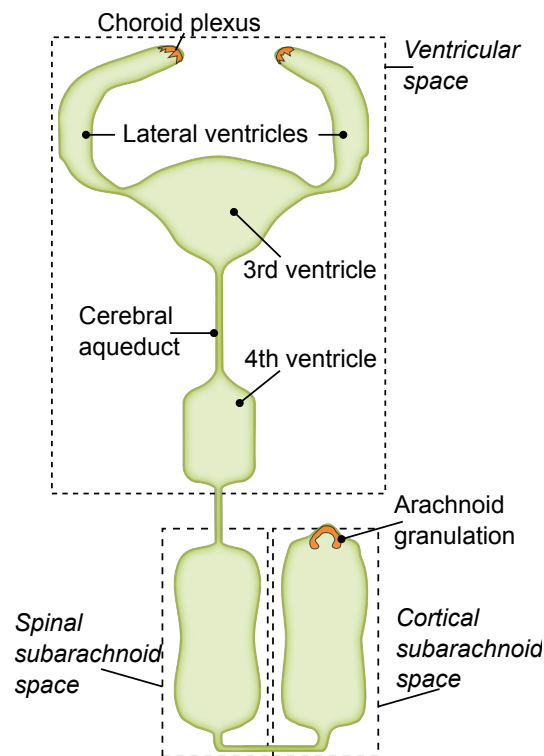


Figure 3.1 – Cerebrospinal fluid circulates from ventricles where it is produced to the subarachnoid space where it is resorbed. The fluid flows through the different encountered spaces from the ventricles to the cortical subarachnoid space (Modified from Rekte [143]).

3.2.2 Segmentation of the entire cerebrospinal fluid volume

Segmentation consists in homotopically thicken an inner object (C_{inner}), which is within the entire cerebrospinal fluid and is topologically equivalent to a filled sphere. This transformation, which preserves the topology of the inner object, is guided by a priority function based on a distance criterion. The inner object can be defined interactively or automatically since it has the correct topology.

To speed up significantly the processing time, we propose to initialize the inner object automatically as close as possible to the border of the cerebrospinal fluid. We also initialize an outer object of the cerebrospinal fluid (C_{lim}), which includes the entire fluid but do not necessarily have the same topology. Thus, guiding the thickening by the priority function is limited to the region between C_{inner} and C_{lim} .

Initialization of inner and outer objects

An inner object C_{inner} is initialized by applying the moment-preserving thresholding described in Tsai [172] on the initial image, followed by a larger connected component extraction as illustrated in Fig. 3.3(b). The moment-preserving thresholding is a histogram-based thresholding technique which is suited to “binary nature” images with low contrast [156]. The moment preservation assumes that statistical moments on initial and thresholded images are identical. Therefore, this method becomes more efficient than conventional clustering-based or entropy-based methods when the histogram presents an excessive overlapping between classes [156]. Since the thresholded image contains several objects, a connected component labeling [157, Chapter 3] is performed to extract the three largest connected components, which correspond to the inner object C_{inner} and both eyeballs E_1 and E_2 . E_1 and E_2 are retained to define a region of interest in Section 3.3.1. By extracting the largest components, residual noise as well as other small objects such as salivary ducts are also removed. If C_{inner} has holes, (see [86, Chapter 5] for a hole characterization) then the threshold is adjusted automatically by increasing its value until the topological assumption on C_{inner} is satisfied; E_1 and E_2 are not affected by this operation due to their intensity.

To initialize an outer object C_{lim} , another histogram-based thresholding method is carried out on the initial image as described in Zack et al. [188]. The triangle thresholding algorithm in [188] is suitable for bimodal images for which the object to extract has a small amplitude and a large variance relatively to the background. It is followed by a largest connected component extraction to retrieve an outer object of the fluid (C_{lim}) as shown in Fig. 3.3(c).

Priority function

The priority function $\Psi = \{\psi_x\}$ controls the order in which voxels are processed and eventually added to C_{inner} . This function uses a Euclidean distance map denoted by $D = \{d_x\}$, which is defined for each voxel $x \in \bar{C}_{\text{inner}}$ as the distance to the nearest voxel of C_{inner} ; it is calculated by the linear algorithm proposed in Saito and Toriwaki [149]. The value ψ_x of each voxel x is then given by:

$$\psi_x = \begin{cases} d_x & \text{if } x \in C_{\text{lim}}, \\ +\infty & \text{otherwise.} \end{cases} \quad (3.1)$$

Euclidean distance transform was preferred to others because it improves selection of points that should be tested while the thickening process.

Guided homotopic thickening

Guided by the previous priority function Ψ , a homotopic thickening is applied to the inner object C_{inner} by adding simple points.

A point is simple if its addition to or its removal from a binary object C does not change the topology of the object and that of the background. Therefore, adding or removing simple points does not change the number of connected components and holes (cavities and/or handles) of C and its complement \bar{C} . Figure 3.2 illustrates the notion of simple point: the center point in the cubic grid is simple in (a) because the topology of C remains unchanged if the point is removed, while it is not simple in (b) as a hole is created.

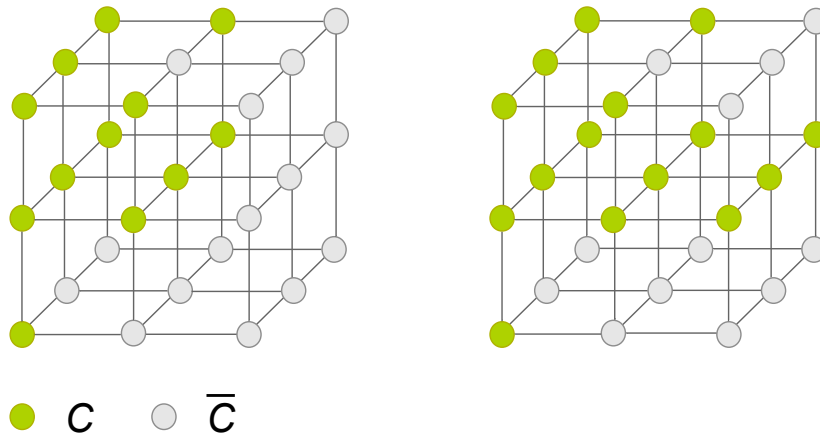


Figure 3.2 – Example of simple point. (a) simple point; (b) non simple point.

Bertrand and Malandain [10] showed that a simple point x is locally characterized by two local topological numbers. An efficient computation of these numbers that only involves the 26-neighborhood is also described in [10].

Let $\partial\bar{C}_{\text{inner}}$ denotes the boundary of C_{inner} such that $\partial\bar{C}_{\text{inner}} = \{x \in \bar{C}_{\text{inner}} \cap C_{\text{lim}} \mid N_6(x) \cap C_{\text{inner}} \neq \emptyset\}$, where $N_6(x)$ is the 6-neighborhood of x . The thickening process consists in adding to C_{inner} simple points from $\partial\bar{C}_{\text{inner}}$ as presented in Algorithm 1. It shows that boundary points (*i.e.*, voxels) of $\partial\bar{C}_{\text{inner}}$ are chosen iteratively, according to their priorities, and are incorporated into C_{inner} if they are simple.

The resulting thickened object has the same topology as C_{inner} . It is illustrated in Fig. 3.3(d).

3.3 SEPARATION INTO THE CEREBROSPINAL FLUID VOLUMES

Separation of the cerebrospinal fluid spaces is required to analyze the relationship between the entire subarachnoid and ventricular volumes. First, the spinal and in-

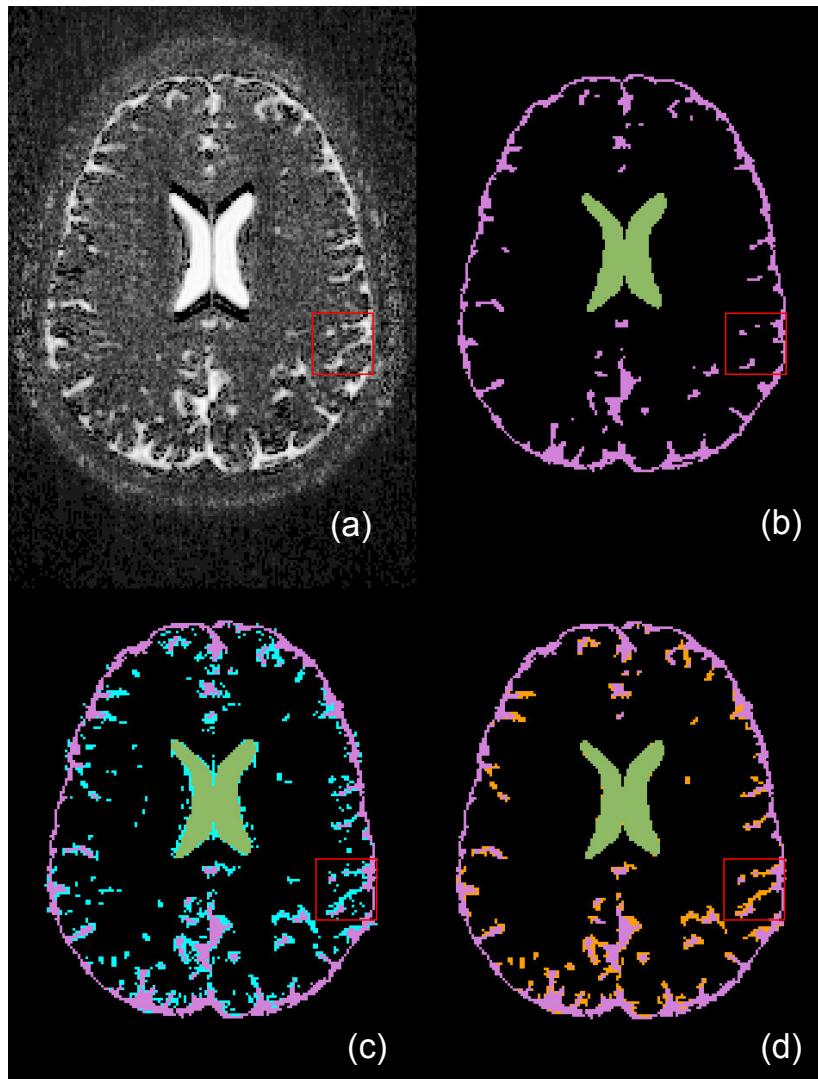


Figure 3.3 – Segmentation process (axial cross-section), which is easily observed in the red square region. (a) contrast-enhanced original image; (b) inner object image C_{inner} (ventricular and cortical subarachnoid spaces are represented respectively in green and magenta); (c) outer region image C_{lim} (voxels of $C_{lim} \setminus C_{inner}$ are represented in cyan); (d) homotopic thickened image (voxels added to C_{inner} are represented in orange).

Algorithm 1: Guided homotopic thickening

Input: C_{inner}, Ψ **Output:** C_{inner} Initialize $\partial\bar{C}_{\text{inner}}$;Make a priority queue \mathcal{Q} of all $x \in \partial\bar{C}_{\text{inner}}$ using ψ_x in the ascending order ;**while** $\mathcal{Q} \neq \emptyset$ **do** Poll x from \mathcal{Q} ; **if** x is simple for C_{inner} **then** $C_{\text{inner}} \leftarrow C_{\text{inner}} \cup \{x\}$; Modify $\partial\bar{C}_{\text{inner}}$; Insert new points of $\partial\bar{C}_{\text{inner}}$ around x to \mathcal{Q} ; **end if****end while**

tracranial regions are separated using a topological property of the cerebrospinal fluid at their interface. Second, to retrieve the volume of the ventricular space from that of the cortical subarachnoid one, the cerebral aqueduct must be detected because we use it as a morphological reconstruction marker.

3.3.1 Separation of spinal and intracranial spaces

Specialists usually perform the disconnection of the spinal and intracranial spaces by tracking the foramen magnum (the hole in the bottom of the cranium through which the spinal cord passes in order to be connected to the brain), which is, even for an expert, difficult to detect on this image. The separation into spinal and intracranial spaces requires to locate the closest axial cross-section plane to that of the foramen magnum. Thus, the disconnection is achieved by browsing the planar connected component on each axial plane from the spinal part, and by detecting any change in its topology (see the axial cross-section in Fig. 3.4). A region of interest is first determined to reduce the processing time as well as to improve the robustness.

Determination of the region of interest

A region of interest \mathcal{R} is used to retrieve the cerebral aqueduct in order to separate the intracranial space into its ventricular and subarachnoid spaces (see Section 3.3.2). Apart from pathological cases, eyeballs typically face the cerebral aque-

duct in the axial plane. We consider the region forming a rectangular cuboid, each of whose edge is parallel to one of the i -, j -, k -axes of the image, such that:

- the region is located in the i -axis direction between the coronal plane that passes through the maximum posterior boundary of eyeballs, and the last coronal plane that still contains non-zero voxels;
- setting D as the larger diameter of both eyeballs, the height of the region is set empirically to be $8D$, such that the top face of the region is located with the distance $2D$ above the eyeballs and the bottom face is located with the distance $5D$ below the eyeballs. The height is chosen in agreement with an expert so as to contain all the necessary structures for the separation step. It may also be interactively resized to fit human variations;
- the depth is determined by the two sagittal planes between the medial boundaries of eyeballs.

Determination of the cutoff plane

Planar connected components are counted on each axial plane from the bottom to the top of the region of interest \mathcal{R} . The first axial plane that shows a change in the number of connected components is the plane just above that of the searched cutoff as shown in Fig. 3.4.

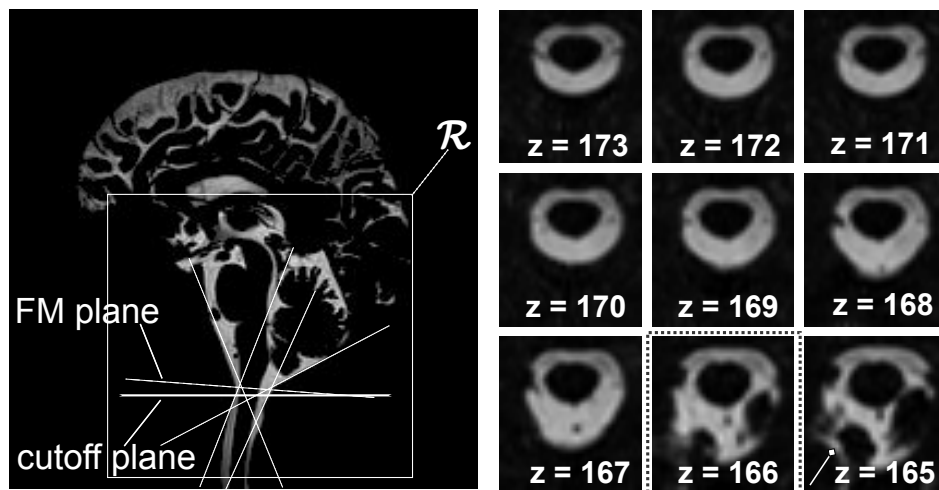


Figure 3.4 – Separation of intracranial and spinal regions in the region of interest \mathcal{R} . The resulting cutoff plane ($z = 166$) is close to that goes through the foramen magnum (FM plane). The axial cross-sections around the cutoff plane are also illustrated (right).

3.3.2 Intracranial volume separation

The process to extract the ventricular space may fail because of some subarachnoid regions that are very close to the third and fourth ventricles. Figure 3.5 shows, for instance, the proximity between the interpeduncular cistern and the infundibular recess of the third ventricle.

To overcome this problem we first detect the cerebral aqueduct that is a thin tubular structure (see Section 2.1) located in the most median sagittal planes, which connects the third and fourth ventricles. It is also the longest tubular structure with the highest intensity range in the most median sagittal planes of the region of interest \mathcal{R} . Its enhancement is performed by a vessel segmentation method [100]. Finally, ventricles are recovered by a morphological reconstruction [179] using the cerebral aqueduct as a marker.

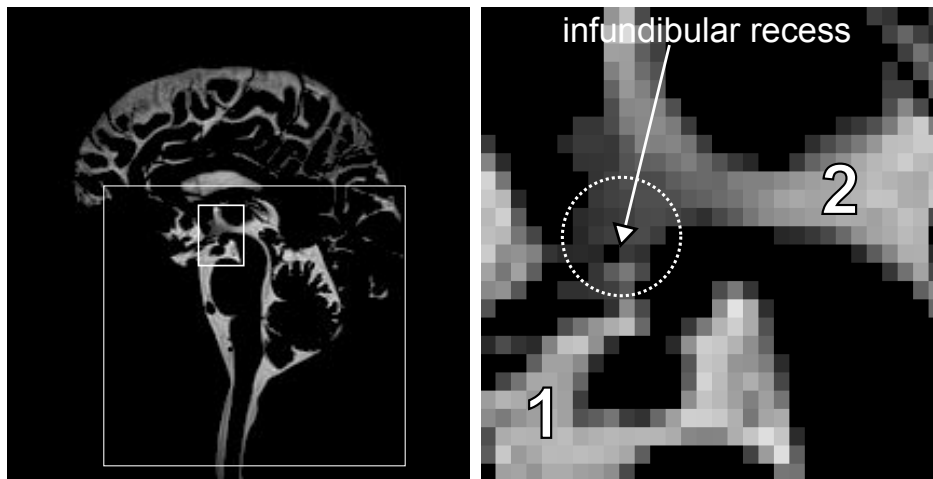


Figure 3.5 – Proximity of the interpeduncular cistern (1) to the infundibular recess of the third ventricle (2). The small rectangular part in the left figure is zoomed in the right figure.

Detection of the cerebral aqueduct

Various methods to enhance vessel like structures in grayscale images are reviewed in Lesage et al. [100]. Among these methods, several efficient methods are based on properties of eigenvalues of the Hessian matrix \mathcal{H} [48, 88, 105, 111, 151, 166]. These multiscale methods operate in a Gaussian scale space on which they calculate second-order derivatives, build the Hessian matrix \mathcal{H} and decompose it depending on its eigenvalues λ_1 , λ_2 and λ_3 such that $|\lambda_1| < |\lambda_2| < |\lambda_3|$. The eigenvalues are analyzed to determine the likelihood for each voxel x to belong to a curvilinear structure. This analysis is based on the following assumptions: (1) $\lambda_1 \approx 0$; (2) $\lambda_2 \approx \lambda_3 < 0$; and (3) $|\lambda_1| \ll |\lambda_2|$.

The tubular structure filter implemented by Frangi et al. [48] allows to dissociate strict tubular structures from others. We use it here to enhance the cerebral aqueduct. Let $F_\sigma = \{f_x^\sigma\}$ the filter in [48] such that:

$$f_x^\sigma = \begin{cases} 0 & \text{if } \lambda_2 > 0 \text{ or } \lambda_3 > 0, \\ (1 - e^{-\frac{\mathcal{R}_A^2}{2\alpha^2}})e^{-\frac{\mathcal{R}_B^2}{2\beta^2}}(1 - e^{-\frac{\mathcal{S}^2}{2c^2}}) & \text{otherwise,} \end{cases} \quad (3.2)$$

where $\mathcal{R}_A = |\lambda_2| / |\lambda_3|$, $\mathcal{R}_B = |\lambda_1| / \sqrt{|\lambda_2\lambda_3|}$, $\mathcal{S} = \sqrt{\lambda_1^2 + \lambda_2^2 + \lambda_3^2}$, with some weights $\alpha \in [0, 1]$, $\beta \in [0, 1]$ and $c \in [0, 500]$.

Figure 3.6 compares extracted curvilinear structures in the region of interest \mathcal{R} using methods from Sato et al. [151] (Fig. 3.6(b)) and Frangi et al. [48] (Fig. 3.6(c)). It shows that in contrast with filter proposed in [151], the filter defined in [48] allows to dissociate strict tubular structures from others. The cerebral aqueduct part has more highlighted values in Fig. 3.6(c) by adjusting the filter with a higher weight to detect lines ($\alpha = 0.7$). The aqueduct is the longest connected component found in the most median sagittal planes.

Ventricles reconstruction

Considering the cerebral aqueduct part as the marker, we aim to reconstruct the ventricular space. For this problem, methods such as fast marching and level set introduced by Sethian [155] or active contour models proposed by Cohen [22] are well known. However, the following two problems may hinder the reconstruction by the above methods: (1) the cerebral aqueduct part is not a large enough marker to initialize a model; (2) motion artifacts can generate significant intensity inhomogeneities even in the ventricular space.

Geodesic reconstruction introduced by Vincent [179] is a very useful operator from mathematical morphology that provides satisfactory results here.

Let $\delta_{f, B_d}^{(1)}(g)$ be the elementary geodesic dilation of a grayscale image g inside f (g is called the marker image and f is the mask) such that $\delta_{f, B_d}^{(1)}(g) = (g \oplus B_d) \wedge f$, where \wedge stands for the point-wise minimum and $g \oplus B_d$ is the geodesic dilation of g by an isotropic structuring element B_d chosen as a flat ball of radius $r_d = 1$. The geodesic dilation of size $n \geq 0$ is obtained by:

$$\delta_{f, B_d}^{(n)}(g) = \underbrace{\delta_{f, B_d}^{(1)} \circ \delta_{f, B_d}^{(1)} \circ \dots \circ \delta_{f, B_d}^{(1)}}_{n \text{ times}}(g). \quad (3.3)$$

The grayscale reconstruction by dilation $\rho_{f, B_d}(g)$ of f from g is calculated by iterating geodesic dilations of g inside f until idempotence such that:

$$\rho_{f, B_d}(g) = \bigvee_{n \geq 1} \delta_{f, B_d}^{(n)}(g), \quad (3.4)$$

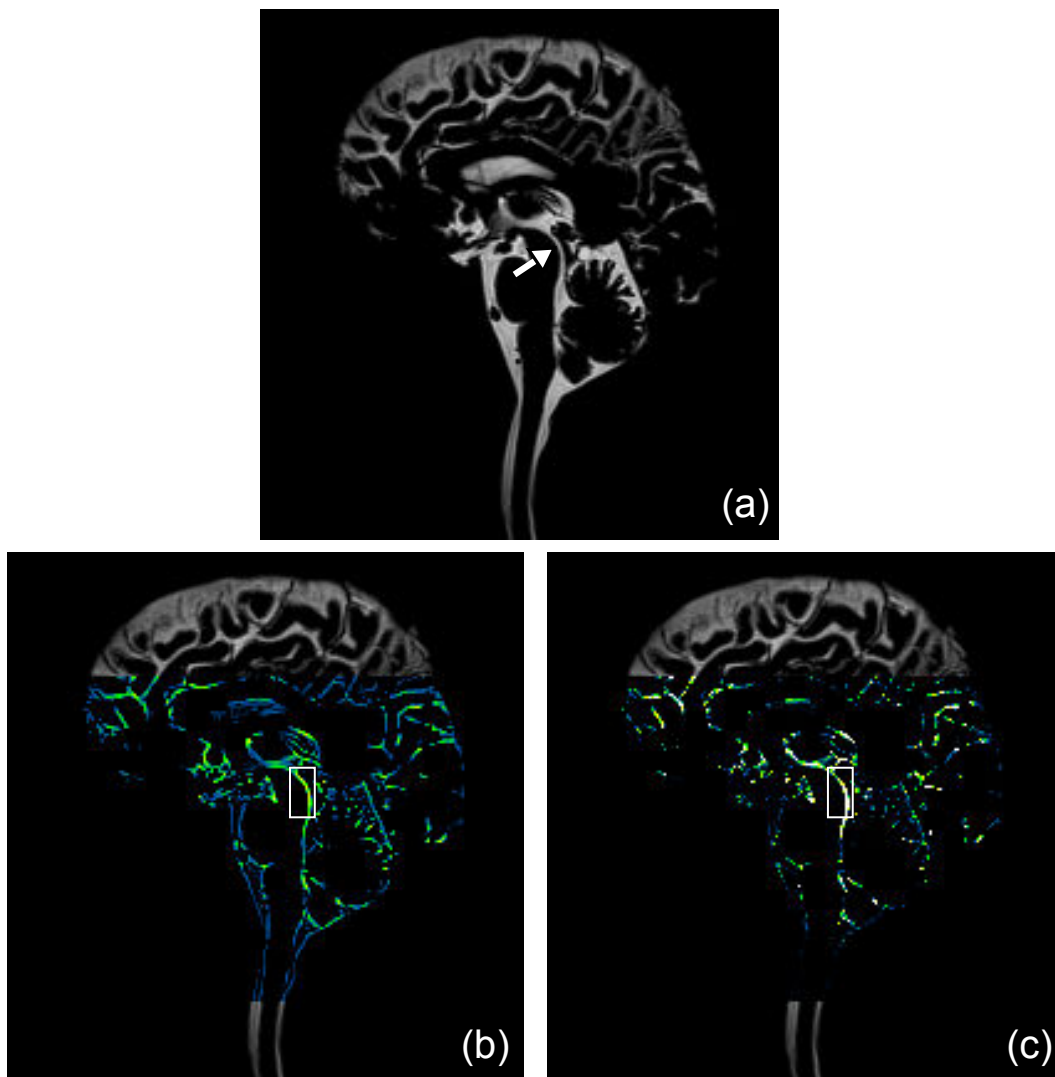


Figure 3.6 – Detection of the cerebral aqueduct in the region of interest \mathcal{R} (midsagittal plane cross-section). From left to right: (a) original thickened image; (b) filtered image with method in Sato et al. [151] ($\sigma = 0.5$); (c) filtered image with method in Frangi et al. [48] using 5 scale spaces σ from 0.4 to 0.9 and with $\alpha = 0.7$, $\beta = 0.2$ and $c = 200$.

where \vee stands for the point-wise maximum.

The geodesic reconstruction of the previously detected cerebral aqueduct used as the marker image is restricted to the region of interest. It generates an image composed of *regional maxima* due to the threshold decomposition used in [179]. The ventricular space is the union of the regional maxima whose intensities are greater than or equal to those which constitute the cerebral aqueduct. A *h-dome* transform [179] allows to keep these regional maxima only. Figure 3.7 shows the result of such a reconstruction for a healthy adult by using a flat ball of radius $r_d = 1$.

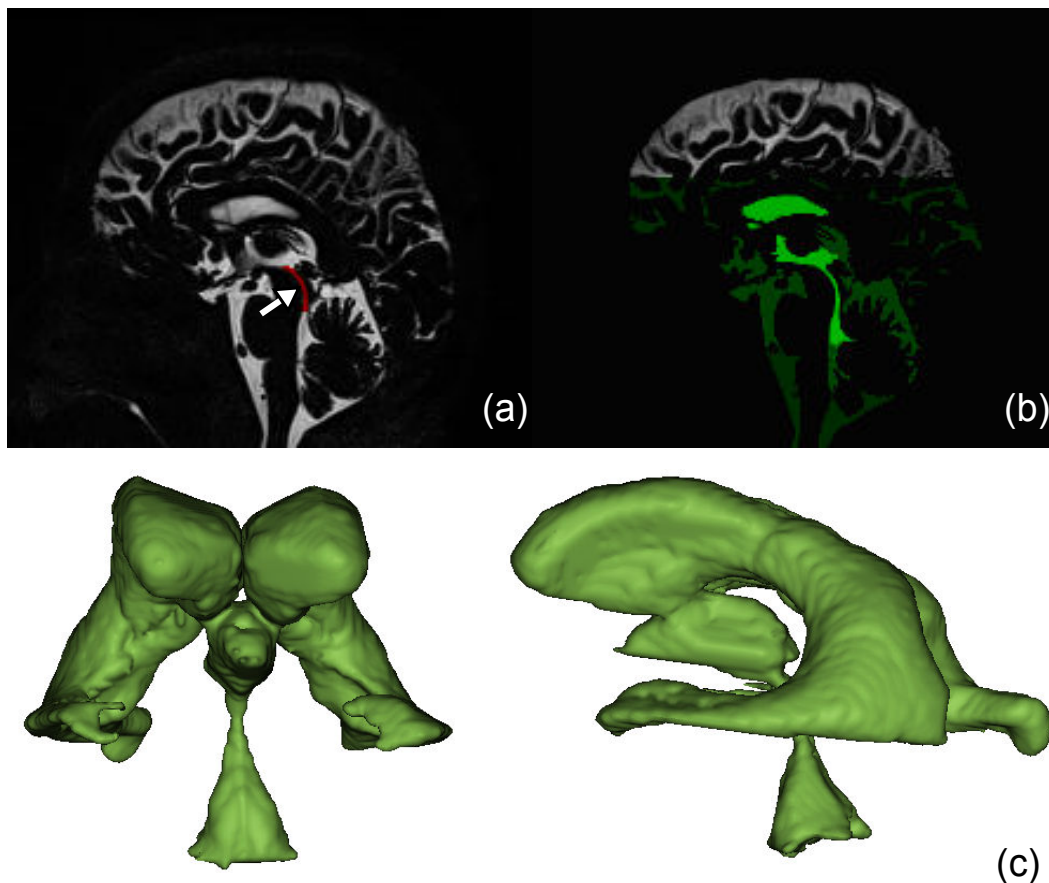


Figure 3.7 – Ventricular space retrieving using a grayscale reconstruction by dilation of the cerebral aqueduct inside the original image: (a) the initial image (the mask) and the cerebral aqueduct (the marker) colored in red; (b) result of the grayscale reconstruction with regional maxima colored in different tons of green; (c) frontal (left) and sagittal (right) views of the ventricular space for a healthy adult using a grayscale reconstruction by dilation of the cerebral aqueduct inside the region of interest \mathcal{R} .

Figure 3.8 shows a three-dimensional visualization of a part of the cerebrospinal fluid spaces obtained by our method; a healthy adult (left) and a non-communicating hydrocephalus patient (right).

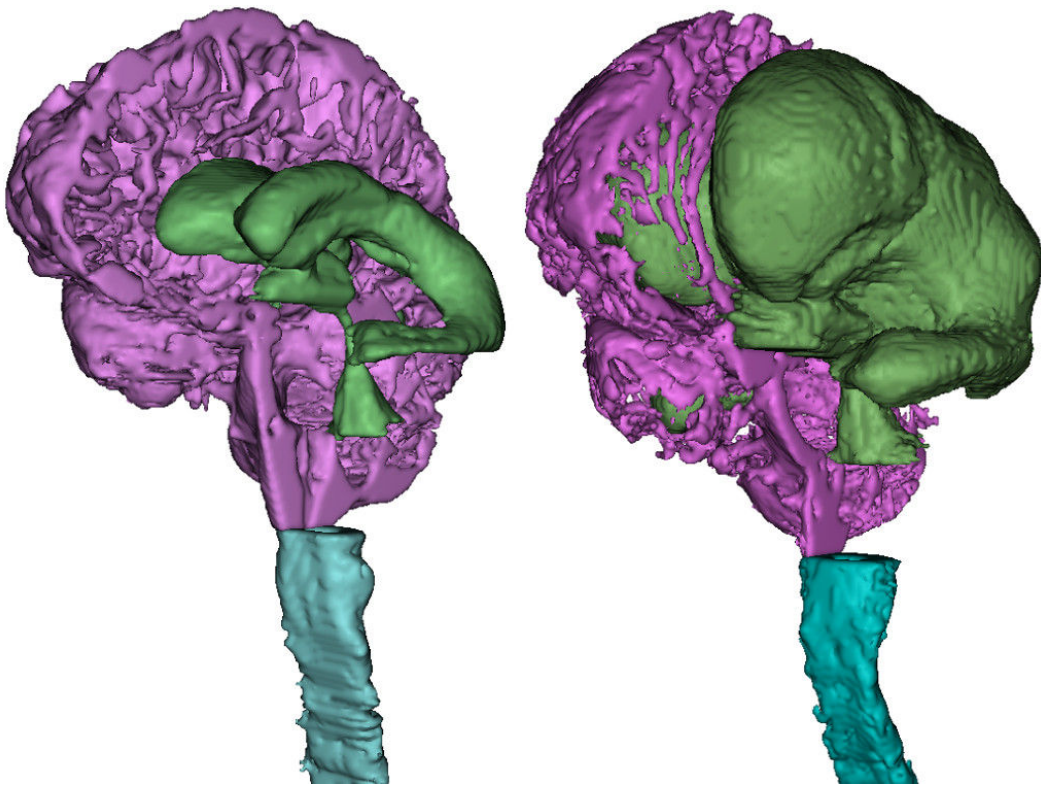


Figure 3.8 – Partial three-dimensional surface renderings of segmented cerebrospinal fluid spaces (the cortical subarachnoid space was cut along the midsagittal plane). Ventricular, cortical subarachnoid and spinal subarachnoid spaces are respectively colored in green, magenta and cyan. Left: a healthy adult; right: a non-communicating hydrocephalus patient.

3.4 CEREBROSPINAL FLUID VOLUMES ANALYSIS

We first present experiments we have carried out to assess volumes of the cerebrospinal fluid spaces from whole body magnetic resonance images in two stages: (1) the segmentation method has been tested on phantoms of known volume; (2) the segmentation and separation steps have been performed on a clinical dataset. 12 healthy controls and 26 patients have been processed; no manual intervention was required for any of them.

We then statistically analyze the distribution of the subarachnoid space volumes relative to the ventricular ones. More specifically we apply a linear regression on the healthy adults subset, as well as a linear discriminant analysis on the clinical dataset distribution to classify healthy and pathological cases.

3.4.1 Volume assessment

Experiments for volume assessment were carried out on 5 phantoms of known volume (image size: 128 slices of 250×250 in the sagittal plane; range of volumes: 294–1500cm³) and 38 clinical images (image size: 160 slices of around 260×790 in the sagittal plane). Processing took place on a conventional PC (Intel Pentium Dual Core 1.60 GHz / 4 GB main memory, Linux 2.6 operating system), and the application was implemented in the Java programming language using the Fiji software [153]. The overall time to assess volumes is 20 min or less for each patient: 12 min or less for the image acquisition and approximately 6 min for its processing. Clearly, this computation time could be dramatically reduced by using a computer with an architecture dedicated to three-dimensional image processing.

Entire volume assessment validation

The segmentation method for the entire volume assessment was validated first on phantom images using the same sequence. Images were acquired from synthetic resin phantoms mimicking the cerebral sulci with various shapes and volumes as shown in Fig. 3.9. The segmentation method on phantoms has resulted in accuracy of $98.5\% \pm 1.8$ against $94.6\% \pm 4.0$ for the semi-manual segmentation by an expert using the method proposed in [69]. Figure 3.10 resumes volume assessments for each phantom using different methods.

Clinical dataset images were evaluated by a physician expert. First the expert ensured that anatomical structures except for cerebrospinal fluid were removed correctly. Second, the accuracy of the segmentation process was assessed by comparing the fluid boundaries using the segmented images and the original images.



Figure 3.9 – Photography of a synthetic resin phantom (volume: 1494cm^3) mimicking the cerebral sulci used to validate the entire cerebrospinal fluid volume segmentation method. Right: cross-section of the corresponding magnetic resonance image.

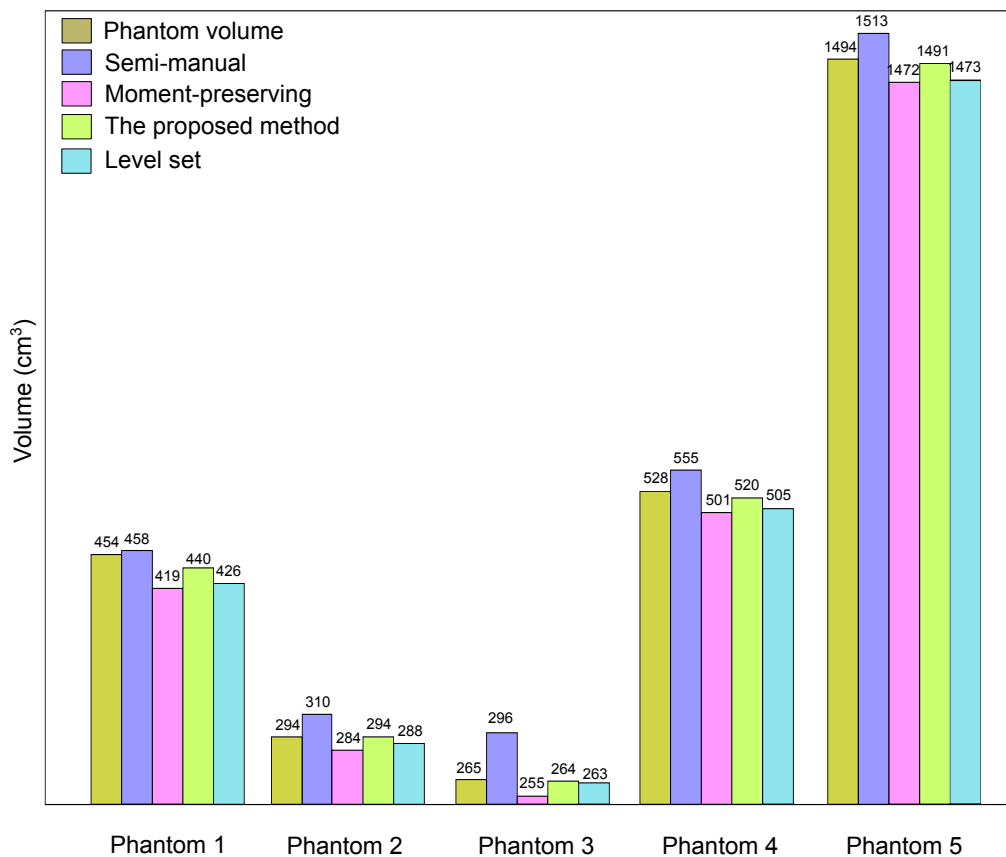


Figure 3.10 – Comparisons of the total volume assessment for phantoms using different methods with the ground truths: the semi-manual segmentation by an expert as described in [69]; the moment-preserving method to extract the initial inner object (see Section 3.2.2); the proposed method (guided homotopic thickening in Section 3.2.2); the level set method [155].

Spaces volume assessment

The obtained volumes of the cerebrospinal fluid spaces are summarized in Table 3.1 where they are matched with previous results from the literature [24, 167, 117, 186, 106, 173, 135, 38, 69] for healthy adults, communicating and non-communicating hydrocephalus classes. In Table 3.1, results vary slightly depending on the articles. The reason is not only due to the difference among methods, but also because of different data and image resolutions. Results on the spinal subarachnoid space confirm the assumption in Edsbacke et al. [38] that the spinal subarachnoid volume assessment is important to discriminate between hydrocephalus patients, *i.e.*, communicating and non-communicating hydrocephalus classes.

The expert ensured that the accuracy of the separation process was assessed by comparing the fluid boundaries using the segmented images and the native clinical images.

3.4.2 Statistical analysis of volumes

Clinical images were acquired from different subjects between 23 and 91 years old: 12 healthy volunteers and 26 patients among which 20 communicating hydrocephalus and 6 non-communicating hydrocephalus. The software package R [140] was used for statistical analysis.

Linear regression for healthy adults

Observing the distribution of the subarachnoid volume relative to the ventricular one (see Fig. 3.12) has provided us the idea of applying a linear regression analysis to the healthy people subset [94, 178]. Let V_V and V_S the respective volumes of the ventricular and entire subarachnoid spaces. We use the linear model for fitting to the healthy people volume pair (V_V, V_S) set: $V_S = \beta_0 + \beta_1 V_V + \epsilon$, and optimize the intercept β_0 and the slope β_1 by minimizing the residual error ϵ . We obtain $\beta_0 = 0$ and $\beta_1 = 10.73$, namely:

$$V_S = 10.73V_V \quad (3.5)$$

Table 3.2 includes some statistics about the model: (1) the coefficient of determination R^2 ($= 88.83\%$) indicates that the predictor explains rather well the answer with 95% of significance; (2) the Fischer's F -statistic ($= 87.51$) and the p -value ($= 1.43e - 06 \ll 0.05$) show further that the null hypothesis ($\beta_1 = 0$) can be re-

Table 3.1 – Comparison of our cerebrospinal fluid volumes with the previous results from literature, for healthy adult people, communicating (CH) and non-communicating hydrocephalus patients (NCH). Each value is represented by a mean \pm standard deviation..

Cerebrospinal fluid volumes (cm ³)										
Author	Modality	Voxel size (mm ³)	Method	Class	Ventricles	Cortical sub.	Spinal sub.			
Condon <i>et al.</i> [24] (1986)	MRI/0.5T/T2-weighted	1 × 1 × 18	semi-manual	controls	25.3 ± 4.6	97.6 ± 6.6	–			
				CH	83.4	108.5	–			
				NCH	606.6	174.1	–			
Tanna <i>et al.</i> [167] (1991)	MRI/1.5T/T2-weighted	NA	semi-manual	controls	31.9 ± 17.8	132.6 ± 43.2	–			
Matsumae <i>et al.</i> [117] (1996)	MRI/1.5T/T2-weighted	1 × 1 × 3	semi-manual	controls	17 ± 9	89 ± 27	–			
				CH	116 ± 42	133 ± 42	–			
				NCH	253 ± 96	172 ± 63	–			
Yoshihara <i>et al.</i> [186] (1998)	MRI/1.5T/3D-FASE	1 × 1 × 1.5	semi-manual	controls	14.9 ± 5.84	127.5 ± 43.04	–			
				CH	67.2 ± 15.81	125.8 ± 50.65	–			
Lundervold <i>et al.</i> [106] (2000)	MRI/1.5T/Mixing	1 × 1 × 1.5	semi-manual	controls	12.6 ± 5.5	146.5 ± 23.22	–			
Tsunoda <i>et al.</i> [173] (2000)	MRI/1.5T/3D-FASE	1 × 1 × 1.5	semi-manual	controls	24 ± 10	177 ± 57	–			
				CH	76 ± 19	203 ± 56	–			
Palm <i>et al.</i> [135] (2006)	MRI/1.5T/T2-weighted	0.6 × 0.6 × 6	semi-manual	CH	156 ± 46	201 ± 37	–			
Edsbagge <i>et al.</i> [38] (2011)	MRI/1.5T/T2-weighted	1.5 × 1.9 × 1.5	semi-manual	controls	–	–	81 ± 13			
Hodel <i>et al.</i> [69] (2011)	MRI/1.5T/3D-SPACE	1 × 0.98 × 0.98	semi-manual	controls	34 ± 19	261 ± 129	–			
				CH	199 ± 56	374 ± 110	–			
				NCH	397 ± 165	234 ± 133	–			
the proposed method [96]	MRI/1.5T/3D-SPACE	1 × 0.98 × 0.98	automatic	controls	28 ± 10	222 ± 84	76 ± 23			
				CH	154 ± 58	269 ± 62	65 ± 18			
				NCH	340 ± 127	154 ± 59	99 ± 27			

jected with a strong presumption and that our model is significant. In addition, the graphical residuals analysis reinforces the linear regression assumptions (Fig. 3.11).

Table 3.2 – Optimal linear regression model on the healthy adult subset from the clinical dataset.

Model	R^2	σ^2	Standard Error	F	p-value
$V_S = 10.73V_V$	0.8883	10.24	0.0088	87.51	$1.43e - 06$

Figure 3.11 shows the distribution of volumes of the entire subarachnoid and ventricular spaces with the model obtained from (3.5).

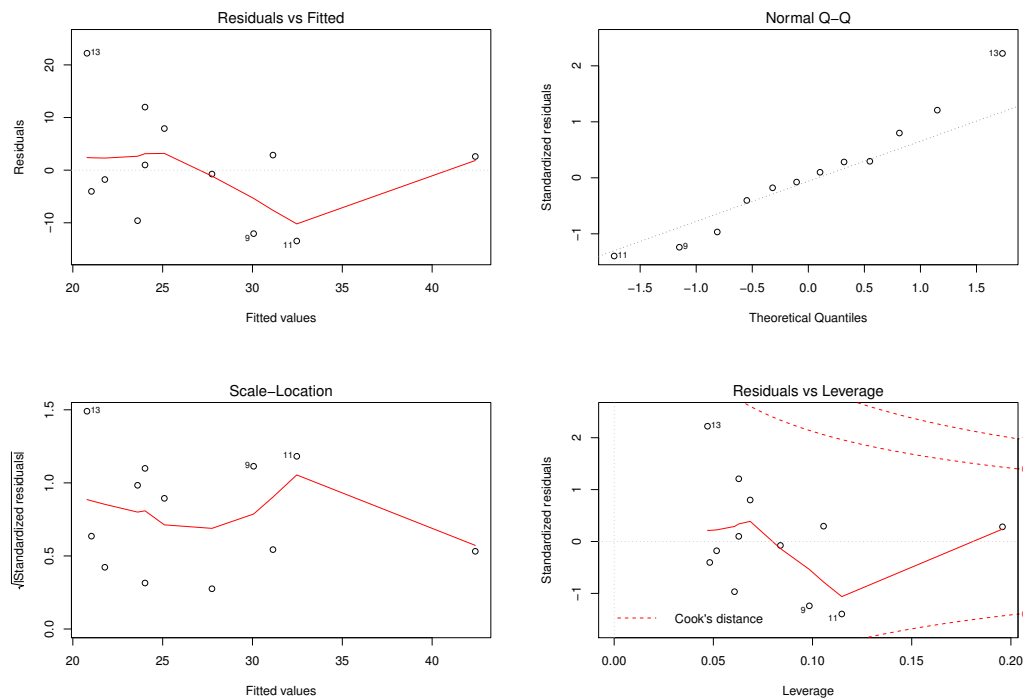


Figure 3.11 – Residual plots from the linear regression on clinical data.

This linear regression analysis indicates that the ratio of the entire subarachnoid space volume to the ventricular space volume is a proportionality constant equal to 10.73 for healthy adults. This proportionality constant ensures a steady-state intracranial pressure.

Classification of clinical data

A linear discriminant analysis [65] was performed on the clinical dataset using volumes of the entire subarachnoid and ventricular spaces as the input variables.

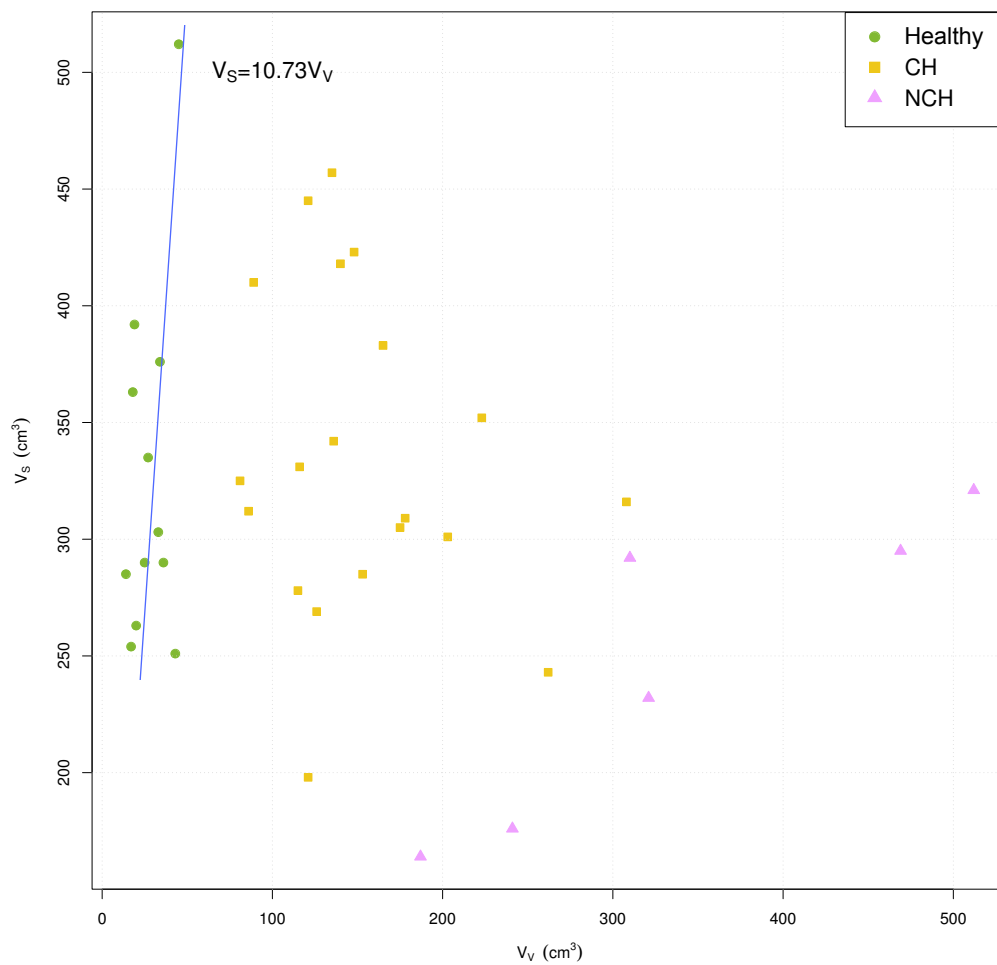


Figure 3.12 – Distribution of the entire subarachnoid space volume V_S relative to the ventricular volume V_V of the clinical dataset. Note the resulting linear regression between volumes of the entire subarachnoid and ventricular spaces for the healthy adults subset such that: $V_S = 10.73V_V$.

We consider three classes: “healthy adults, communicating hydrocephalus and non-communicating hydrocephalus”. Let TP , FP , TN and FN the respective numbers of true positives, false positives, true negatives and false negatives. The sensitivity S_e and the specificity (or recall) S_p are respectively defined as $S_e = TP/(TP + FN)$ and $S_p = TN/(TN + FP)$. The additional F_1 -score metric is also used to validate the classifier. It is defined as $F_1 = 2pS_e/(p + S_e)$ where p stands for the precision, defined by $p = TP/(TP + FP)$.

The predicted classification between healthy adults and pathological cases results in a sensitivity S_e of 100%, a specificity S_p of 100% and a F_1 -score of 100%, which is efficient to discriminate between classes, especially to distinguish elderly healthy adults from elderly patients with communicating hydrocephalus. The predicted classification of non-communicating hydrocephalus results in a sensitivity S_e of 83.33%, a specificity S_p of 91.66% and a F_1 -score of 76.92%, which is a suitable result to suspect a non-communicating hydrocephalus (Fig. 3.13). By considering the spinal subarachnoid volume only, the predicted classification of non-communicating hydrocephalus results in a sensitivity S_e of 83.33%, a specificity S_p of 95.24% and a F_1 -score of 90.90%, which may show some interest of the spinal subarachnoid volume assessment to suspect a non-communicating hydrocephalus; this remains to be confirmed with a larger number of data.

3.5 CONCLUSION

This work uses a recent whole body magnetic resonance imaging sequence that significantly highlights the cerebrospinal fluid. It provides a volume assessment of the fluid spaces. The volumes are automatically retrieved through segmentation and separation steps. These steps use image properties, anatomical and geometrical features, as well as a topological assumption on the entire fluid shape. We made statistical analyses on entire subarachnoid and ventricular volumes. The results show that the ratio of the entire subarachnoid space volume to the ventricular space volume is a proportionality constant ($= 10.73$) for healthy adults in order to maintain a stable intracranial pressure. Indeed, communicating hydrocephalus patients have ratios in the range $[0.93, 4.61]$ and non-communicating hydrocephalus patients have ratios in the range $[0.63, 0.93]$. This result may confirm that this ratio can be an efficient functional index to distinguish healthy adult people from pathological cases, especially to distinguish elderly healthy adults from elderly patients with communicating hydrocephalus.

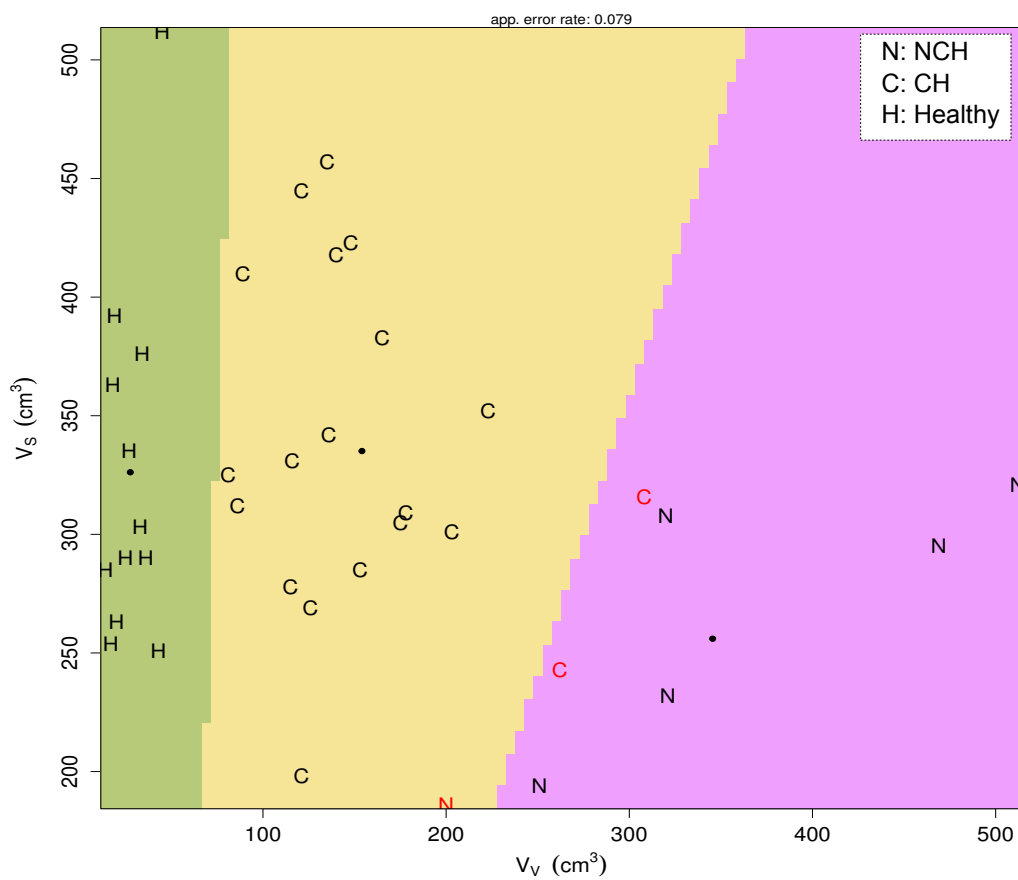


Figure 3.13 – Resulting partition plot on clinical data by using a linear discriminant analysis considering three classes: “healthy (H), communicating hydrocephalus (C) and non-communicating hydrocephalus (N)”.

FLUID DISTRIBUTION IN THE CORTICAL SUBARACHNOID SPACE

CONTENTS

4.1	INTRODUCTION	53
4.2	RELATED WORK	53
4.3	VOLUMETRIC RELIEF MAP	54
4.3.1	Automatic positioning of a hemisphere	55
4.3.2	Voxel distribution on a hemisphere	56
4.3.3	Volumetric relief map as a two-dimensional image	56
4.3.4	Properties of volumetric relief maps	58
4.4	FLUID VOLUME DISTRIBUTION ANALYSIS	59
4.4.1	Volumetric relief map generation	60
4.4.2	Moment-based analysis of the fluid distribution	65
4.4.3	Descriptive discriminant analysis	69
4.4.4	Monitoring of patients	72
4.5	CONCLUSION	72

IN this chapter, we present planar representations called *volumetric relief maps*, which are generated from three-dimensional pre-segmented images of the cerebrospinal fluid within the cortical subarachnoid space. Such maps are visually interpreted at once and serve to characterize fluid distributions. They may help experts to provide a diagnosis and monitor patients instantly.

The work exposed in this chapter was presented during the CARS 2013 conference, held in Heidelberg, Germany. A conference article was published in [97].

4.1 INTRODUCTION

While three-dimensional images provide an abundance of information, their interpretation and processing may be difficult and time-consuming. For example, analysis of cerebrospinal fluid spaces on magnetic resonance images requires from experts to browse various slices according to different spatial planes, and occasionally using several magnetic resonance imaging sequences. As reported in [2], experts have less time for analysis because they have to manipulate a large amount of image datasets and more patients, which should necessitate more efficient and effective work environments. In order to help them perform effective diagnosis and patient monitoring, we propose a two-dimensional image representation, called *volume relief map*. Such a map can be visually interpreted with less difficulty and automatically processed faster, compared with its associated three-dimensional image. It immediately reports to experts about the cerebrospinal fluid distribution within cortical subarachnoid space, and is used to estimate its variation compared with a reference value.

In order to generate such a map, the following three steps are mainly required: (1) setting an analytically defined surface (*i.e.*, a hemisphere here) that encloses the object to analyze, and (2) projecting some features of the object (*i.e.*, its volume here) on the surface; (3) transforming point positions on the surface into those on a plane. This new representation provides not only qualitative information on the object volume distribution (visually speaking) but also quantitative one (by using two-dimensional shape analysis techniques). For characterization of object volume distributions, we propose to perform a moment-based shape analysis, which will be routinely exploited and leads to functional parameters. We also show that these parameters are efficient to discriminate healthy adults from patients affected by communicating or non-communicating hydrocephalus, and thus verifying at a glance that the fluid distribution has returned to a “normal state” after a surgery.

4.2 RELATED WORK

Production of a two-dimensional map from a three-dimensional object requires the following two ingredients: (1) an analytically defined surface that encloses the object to analyze and on which are projected some features; (2) a map projection technique from the surface to a plane.

Concerning the first ingredient, a sphere or an upper hemisphere is often used for brain analyses thanks to its shape similarity [71, 74, 145, 171]. Features projected

on a sphere or a hemisphere are, for example, gray values of the external cerebral cortex that are retrieved in [71] by using a ray casting method [47, Chapter 13], while cortex surface curvatures or depths are projected by using a conformal map in [145, 171].

For the second ingredient, various methods have been studied for a sphere in cartography, *i.e.*, for generating maps or representing the Earth on a flat surface (see [16] for a complete description of map projection techniques). In the medical field, for example, an azimuthal equidistant projection has been applied in [71] for generating a “cartography” of the cerebral cortex surface. In fact, the azimuthal equidistant projection simplifies superposition on the map of data extracted from electroencephalography and magnetoencephalography measurements. Such a map is then used as an anatomical reference as all points on it are at proportionally correct distances and directions from the center point.

In this work, we also use an upper hemisphere as enclosing surface, but we consider the volume of the object projected on surface points, instead of the gray value of the object [71] or the surface curvature or depth [74, 145, 171]. We then use a map projection technique that preserves areas, instead of distances, as it preserves the volume distribution information on the surface (see Section 4.3.3 for more details).

4.3 VOLUMETRIC RELIEF MAP

Suppose the cortical subarachnoid space is pre-segmented, for example, by using the method presented in Chapter 3. Given its volume data, *i.e.*, a three-dimensional voxel set, its associated volumetric relief map is generated in the following two steps. In the first step, we consider an upper hemisphere which is automatically positioned, such that it encloses the superior part of the segmented cortical subarachnoid space. Every voxel is then projected on the hemisphere so that the inside voxel distribution can be observed on the surface of the hemisphere. In the final step, we generate a two-dimensional image by projecting every point on the hemisphere onto a plane. Note that the chosen projection preserves a point distribution in a similar way between the original one on the hemisphere and the new one on the plane. The key point is that we preserve the total amount of fluid volume after the two projections above, and thus in the volumetric relief map. Each step is explained in details as follows. At the end, some properties of volumetric relief maps are also presented.

4.3.1 Automatic positioning of a hemisphere

The aim of the positioning is to prevent any rotation of the cortical subarachnoid space during image acquisition. First, the hemisphere center is positioned at the top rear of the cerebral aqueduct, which is a visible structure in the “fluid specific” magnetic resonance images used in the clinical dataset [69] and whose top rear position is closest to the posterior commissure. This latter contains the pineal gland, which is considered as the geometric center of the brain [40]. Thus, what we need is to locate the cerebral aqueduct automatically from an initial magnetic resonance image. The method described in Chapter 3 is specific to these images. Note that it allows us to locate not only the cerebral aqueduct, but also the eyeballs, which will be used below to set the anatomical reference axes.

After having set the hemisphere center c , its radius is calculated such that it is superior to the maximum distance from c to voxel points of the cerebrospinal fluid volume as illustrated in Fig. 4.1.

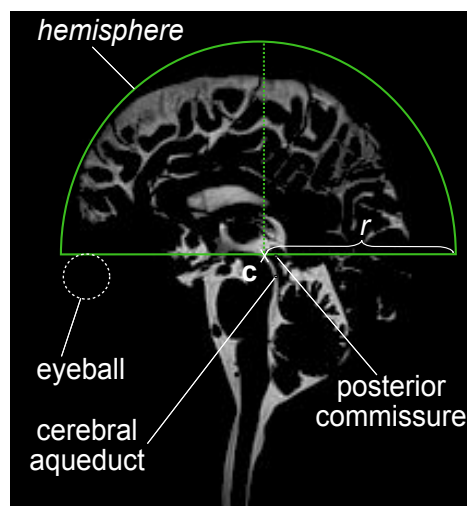


Figure 4.1 – Positioning of the upper hemisphere of center c and radius r to cover the superior cortical subarachnoid space. Position of eyeballs is also indicated (with dashed circle).

Finally, the base of the hemisphere is set to match the plane that passes through the hemisphere center and the tops of the eyeball boundaries.

In order to generate a volumetric relief map, we additionally need two orthogonal axes crossing at the hemisphere center on its base, which will correspond to vertical and horizontal axes in a volumetric relief map. The vertical axis is then determined as the intersection between the hemispherical base plane and the bisector of the tops of the two eyeball boundaries. In practice, the bisector is included in the longitudinal cerebral fissure and the base corresponds to an axial plane as illustrated in Fig. 4.1. Alternatively to this automatic positioning, certainly the manual setting by experts is also possible for its refinement.

4.3.2 Voxel distribution on a hemisphere

Once we set the upper hemisphere as above, we generate a voxel distribution on it as follows. The main idea is that each voxel is considered to have the unit fluid volume, and this unit quantity is represented by the voxel center. With this consideration, the fluid distribution can be replaced by the voxel center distribution so that we only need to project voxel centers to the hemisphere.

Let \mathbf{c} be the center of the projection hemisphere and r be its radius. We project each voxel center point \mathbf{v} to the hemisphere by drawing a three-dimensional ray [47, Chapter 14] starting at \mathbf{c} and going in a direction $(\mathbf{v} - \mathbf{c})$ to obtain its intersection with the hemisphere. This intersection corresponds to the single projected point of \mathbf{v} on the hemisphere, denoted by $\mathbf{p}(\mathbf{v})$ as illustrated in Fig. 4.2(a). Note that different \mathbf{v} can have the same projected points $\mathbf{p}(\mathbf{v})$ if they are collinear.

4.3.3 Volumetric relief map as a two-dimensional image

All voxel-center points projected on the hemisphere, $\mathbf{p}(\mathbf{v})$, are now mapped on a two-dimensional plane as illustrated in Fig. 4.2(b). As mentioned above, we intend to keep the fluid distribution information, *i.e.*, the distribution of $\mathbf{p}(\mathbf{v})$ during this mapping. Therefore, the Lambert azimuthal equal-area projection is chosen as it has the following interesting properties: bijection, diffeomorphism, direction preservation from the point of tangency and area preservation [16, Chapter 3]. In particular, area preservation is essential since it indicates that we may be able to have the same number of projected points on the plane in a unit surface area as that of the original points on the hemisphere in a unit area. The Lambert projection preserves neither angle nor distance, and thus shapes can be distorted in the plane by moving away from the point of tangency. However, such distortion is less observed if the projection is restricted to the hemisphere centered at the point of tangency (*i.e.* the upper hemisphere in this paper) as illustrated in Fig. 4.3 [84].

More concretely, the following formulas are applied for each point $\mathbf{p}(\mathbf{v}) = (x, y, z)$ on the hemisphere, such that $(x - c_x)^2 + (y - c_y)^2 + (z - c_z)^2 = r^2$ and $z \geq c_z$, in order to obtain the single two-dimensional point $\mathbf{P}(\mathbf{v}) = (X, Y)$ in the disc with center at the origin and radius $\sqrt{2}r$:

$$\begin{aligned} X &= \sqrt{\frac{2r}{r + z - c_z}}(x - c_x), \\ Y &= \sqrt{\frac{2r}{r + z - c_z}}(y - c_y). \end{aligned}$$

To generate a volumetric relief map which is a two-dimensional image, we digitize the disc obtained by the Lambert projection. Suppose that the disc is digitized

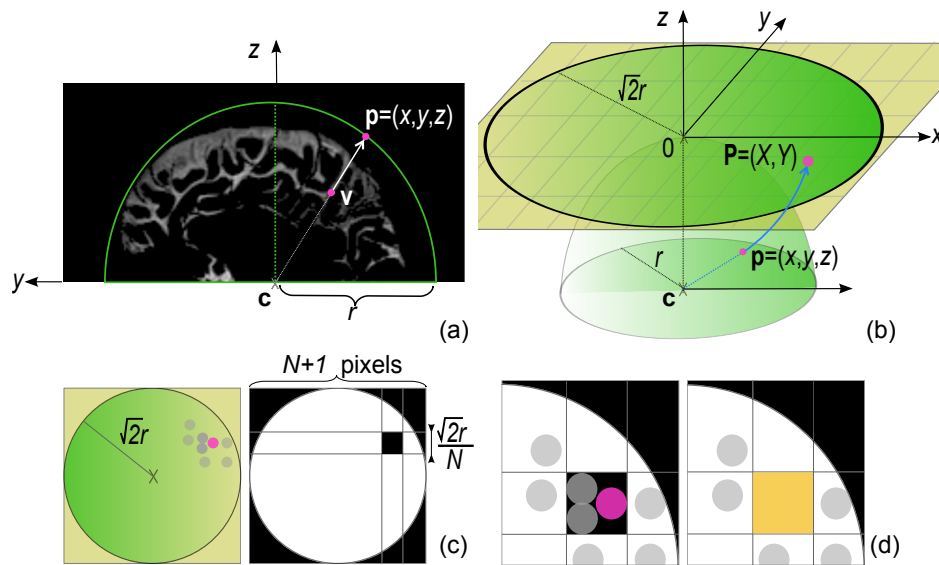


Figure 4.2 – Steps of the volumetric relief map generation: positioning the hemisphere of center c and radius r to cover the three-dimensional object (here the superior cortical subarachnoid space) and projecting each voxel v to its corresponding point p onto the hemisphere using a ray tracing method (a); mapping each p to its corresponding point P on the two-dimensional plane using the Lambert azimuthal equal-area projection (b); digitizing the disc [86] in the two-dimensional grid $(N + 1) \times (N + 1)$ (c); voting each P for a pixel of the disc, then add up the number of associated voxels for each pixel (d).

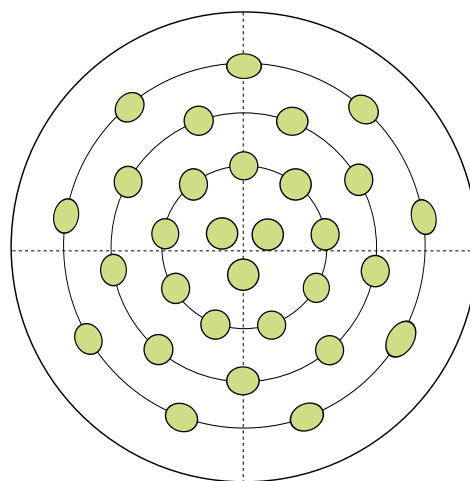


Figure 4.3 – Distortion of Tissot's circles in a relief map using the Lambert azimuthal equal-area projection.

with a square grid of pixel size $\sqrt{2}r/N$ by using the Gaussian digitization (*i.e.*, a pixel is considered in the digitized disc if the center point is in the original disc as illustrated in Fig. 4.4) [86, Chapter 2].

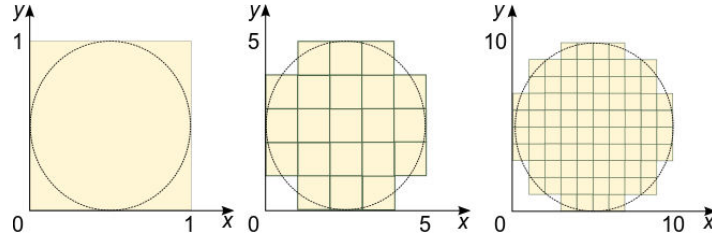


Figure 4.4 – Three disks (dashed) and their colored Gaussian digitizations.

The obtained two-dimensional image containing this digitized disc thus has the support of size $(N + 1) \times (N + 1)$ as illustrated in Fig. 4.2(c).

For each voxel center \mathbf{v} , its projected point $\mathbf{P}(\mathbf{v})$ then votes for the pixel that contains $\mathbf{P}(\mathbf{v})$ itself as illustrated in Fig. 4.2(d). The voting procedure associates each projected point to a single pixel. After this voting procedure for all projected points, we add up for each pixel the number of its associated voxels, *i.e.*, its associated fluid volume quantity. Each pixel value of a volumetric relief map corresponds to the amount of fluid between the chosen center of the cortical subarachnoid space, *i.e.*, the top rear of the cerebral aqueduct, and the associated point on the hemisphere. Briefly speaking, it gives an idea to approximate depths within the subarachnoid space, *e.g.*, depths of cerebral sulci.

4.3.4 Properties of volumetric relief maps

A volumetric relief map has the following interesting properties:

Property 4.1 *Each voxel of a given voxel set is associated to exactly one pixel in the volumetric relief map.*

Property 4.2 *The total amount of pixel values in a volumetric relief map is equal to the total volume of the initial three-dimensional voxel set.*

Property 4.2 is straightforwardly obtained from Property 4.1, which is also directly induced by the voting procedure explained in Section 4.3.3.

Note that the volumetric relief map may be influenced by the two- or three-dimensional space digitizations. As a matter of fact, the Lambert equal-area projection helps each pixel to have a similar voxel quantity for a digitized solid-hemispherical object centered at (c_x, c_y, c_z) if we do not set N to be too large for the relief map size, with respect to the resolution of the original volumetric image.

Let us consider a digitized hemisphere with radius R (unit voxels), whose volume is thus $\frac{2}{3}\pi R^3$ (unit voxels). Suppose that we make a volumetric relief map with the same radius R (unit pixels, instead of unit voxels), then Property 4.2 leads us to the conclusion such that each pixel must be associated to $\frac{2}{3}R$ (unit voxels), as the digitized circle region on the volumetric relief map contains πR^2 (unit) pixels approximately. Figure 4.5 illustrates an example for a digitized hemisphere with radius $R = 40$, and its volumetric relief map whose values are around 26.7 almost everywhere in the digitized circle. In practice, digitization causes some variations of this value. However, such a digitization influence can be reduced in a volumetric relief map by applying a Gaussian filter with a small window to the map.

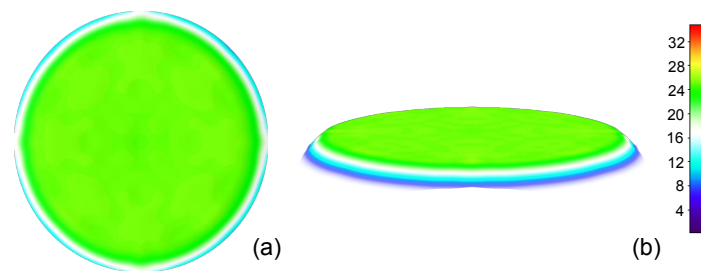


Figure 4.5 – Volumetric relief map (with size 81×81) of a filled hemisphere with radius $R = 40$.

From this experience, the following observation can be made.

Observation 4.1 *The projections of voxel centers in a voxel space are uniformly distributed in the volumetric relief map if the pixel size of the map is sufficiently large with respect to the voxel size.*

In practice, the pixel size of a volumetric relief map is set not to be excessively smaller than the voxel size of the original three-dimensional image. Otherwise, we will have empty pixels in a volumetric relief map, to which no voxel is associated due to the image digitization.

4.4 FLUID VOLUME DISTRIBUTION ANALYSIS

First are described experiments we have carried out to generate volumetric relief maps in order to visualize the fluid distribution within the superior cortical subarachnoid space. Then, we analyze the fluid distribution from the generated maps using a moment-based approach. Finally, we perform a statistical analysis on those fluid distribution results and give some observations on monitoring patients.

4.4.1 Volumetric relief map generation

Clinical dataset

Volumetric relief maps have been generated from a clinical dataset composed of 74 different subjects (median age: 48 years old; range: 18–91 year olds): 44 healthy volunteers and 30 patients with hydrocephalus, among which there are 25 communicating hydrocephalus and 5 non-communicating hydrocephalus. Moreover, eight of the patients had another image acquisitions after their surgery.

Map generation

After the pre-processing of segmentation of the superior cortical subarachnoid space as illustrated in Fig. 4.6, we applied to each image of the dataset the method presented in Section 4.3. The volumetric relief map generation process took place on a conventional computer (Intel Pentium Dual Core 2.70 GHz / 8 GB main memory, GNU/Linux 3.8 operating system), and the application was implemented in the Java programming language using the Fiji software [153].

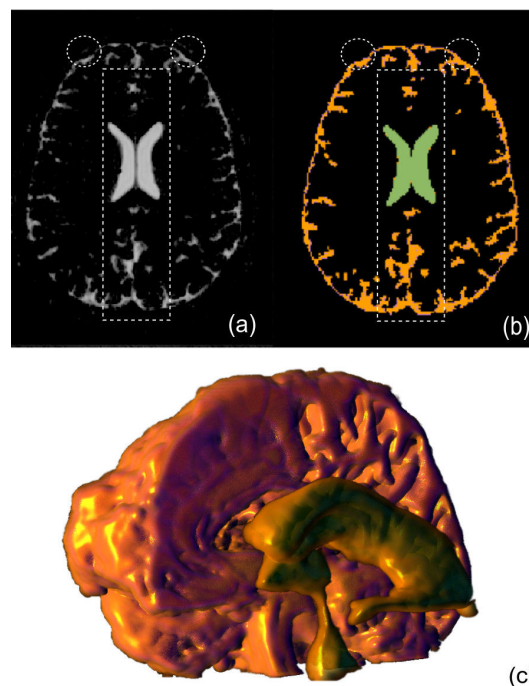


Figure 4.6 – Three-dimensional image pre-processing, by setting a region of interest (illustrated as a dashed-line rectangle) based on the positions of eyeballs (in dashed circles), for separating ventricular and subarachnoid spaces: (a) an axial cross-section of an original image; (b) the cross-section of the segmented ventricular and cortical subarachnoid spaces, represented respectively in green and orange; (c) a partial three-dimensional surface rendering of the cortical cerebrospinal fluid (the subarachnoid space was cut along the midsagittal plane).

Volumetric relief maps were initialized with a width of 203 pixels, and the radius of the hemisphere was set to 100 mm. The overall time of image acquisition including the pre-processing and the map generation is less than 4 min for each patient: 3 min for the image acquisition, 50 seconds for the pre-processing and 1 second or less for the map generation.

Figure 4.7 shows a volumetric relief map example for a healthy volunteer. The acquisition in the sagittal plane and the choice of the hemisphere center, both serve to fix the longitudinal cerebral fissure with the vertical axis and the projection of the top rear of the cerebral aqueduct with the center of the map. For almost every healthy adult, the fluid distribution is well distributed on the entire volumetric relief map with well-filled sulci. The longitudinal cerebral fissure stretches over most of the height of the map with a high intensity, separating the map in two balanced regions. Furthermore, the central cerebral sulcus can be located closely to the horizontal axis and the lateral cerebral fissure is visible near the frontal boundary of the map with a substantial intensity.

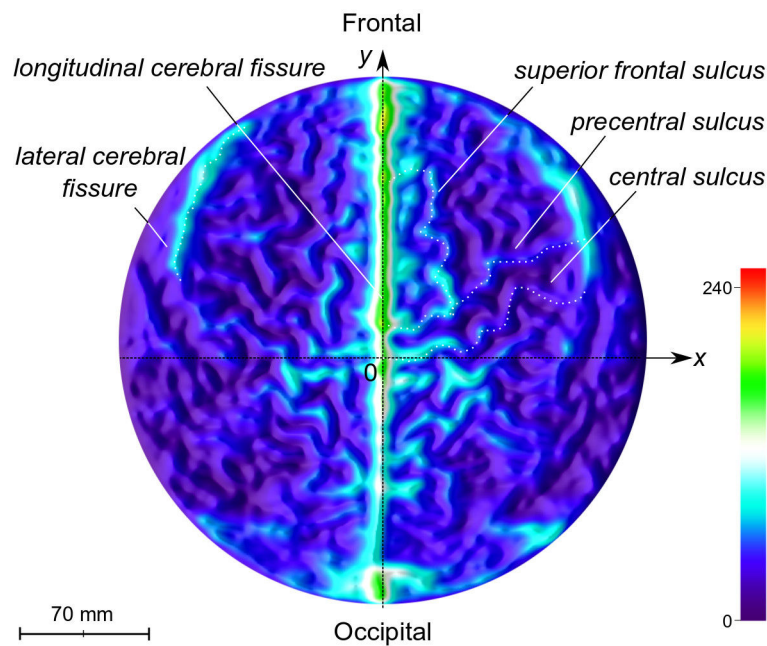


Figure 4.7 – An example of colored volumetric relief map for a healthy adult. Note that the frontal region is on the upper part of the map and the occipital region is on the lower part of the map. The longitudinal cerebral fissure separates the map vertically and appears brighter (y -axis).

With moderate training, experts would be able to verify at a glance that the fluid is well distributed without any depletion, or that it has returned to a normal state after a surgery. Volumetric relief map examples for communicating and non-communicating hydrocephalus patients are shown in Fig 4.8. Clearly, we see different distributions from their corresponding volumetric relief maps. Both patients have loosed symmetry, but communicating hydrocephalus patient has less

fluid within the longitudinal and lateral cerebral fissure in particular (Fig 4.8(a)), whereas non-communicating one has less fluid everywhere, in the center as well except in the lateral cerebral fissure (Fig 4.8(b)).

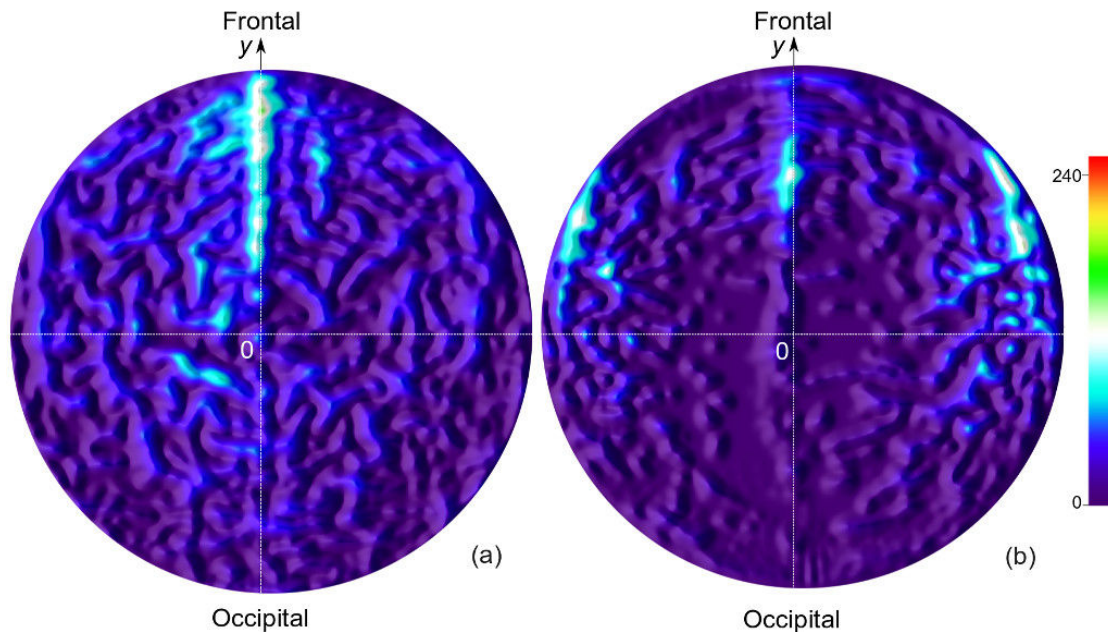


Figure 4.8 – Colored volumetric relief maps for a communicating hydrocephalus patient (a) and a severe non-communicating one (b).

Figure 4.9 shows volumetric relief map examples for one patient before (a) and after (b) a surgery. Before surgery, as observed from Fig. 4.9(a), notice the fluid depleted regions (black and dark blue colors) on the bottom side of the map and the reduced and less bright longitudinal cerebral fissure. Those depleted regions are related to the occipital lobe and posterior parts of both the temporal lobes and the parietal ones. After surgery, as observed from Fig. 4.9(b), the intensity within all cerebral sulci increased as the cerebrospinal fluid has recovered its balanced distribution and depleted regions were restored. Note that, in this case, the longitudinal cerebral fissure does not seem to stretch yet to the entire height with a high intensity, but clearly elongates more than before.

Volumetric relief maps also serve to estimate depths of cerebrospinal fluid within cerebral sulci, *i.e.*, sulcal depths by verifying depths of healthy adults in the clinical dataset. We reported mean depth values of the cerebrospinal fluid inside main cerebral sulci related to the superior cortical subarachnoid space in Table 4.1. Those values are consistent with recent works [168, 187]. Furthermore, Fig. 4.10 shows profiles of the fluid depths, along the medial axis [86, Chapter 3] of some sulci, retrieved from the relief maps of the patient before and after surgery

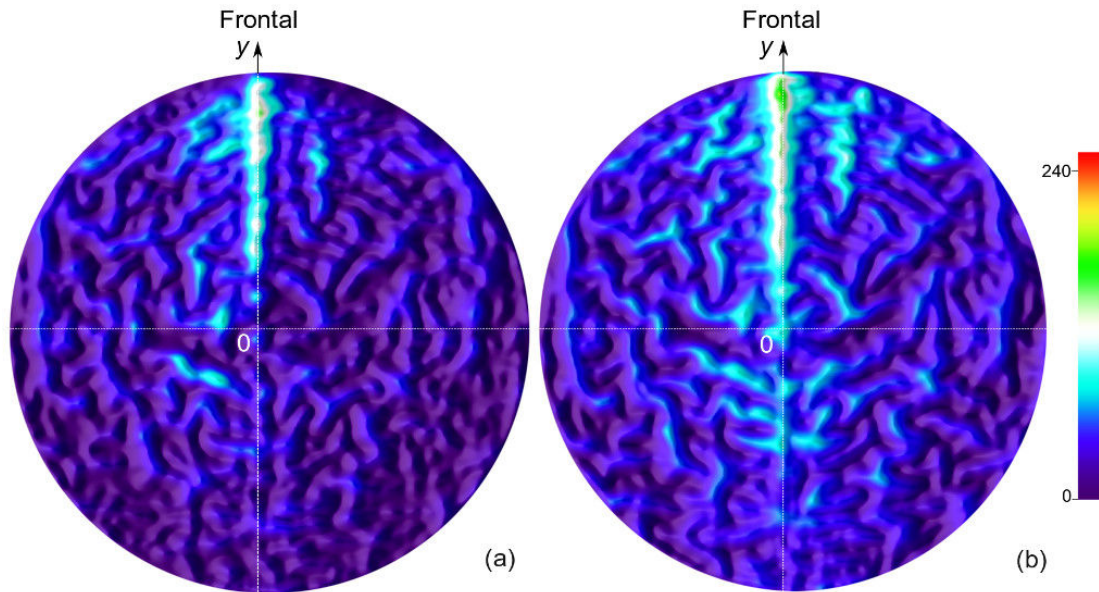


Figure 4.9 – Colored volumetric relief maps for a non-communicating hydrocephalus patient before (a) and after (b) a surgery. Note that the depleted region (black and dark blue colors) in the bottom part of the map in (a) is reduced in (b) and the longitudinal cerebral fissure is less bright in (a) than (b). It is also observed that the fluid has recovered a more balanced distribution after surgery.

in Fig. 4.9. If we compare the profiles before and after surgery, their difference provides the depletion intensity inside a sulcus for a hydrocephalus patient.

Table 4.1 – Assessment of the cerebrospinal fluid depths in main cerebral sulci related to the superior cortical subarachnoid space, along their medial axis. Each value is represented by (mean \pm standard deviation).

Sulcus	Class	Depth of fluid (mm)
central cerebral	healthy	55.32 ± 14
	pathological	29.14 ± 15
precentral	healthy	55.19 ± 16
	pathological	34.88 ± 9
postcentral	healthy	63.88 ± 18
	pathological	35.13 ± 14
superior frontal	healthy	58.12 ± 17
	pathological	44.95 ± 15
intraparietal	healthy	57.28 ± 21
	pathological	26.01 ± 15

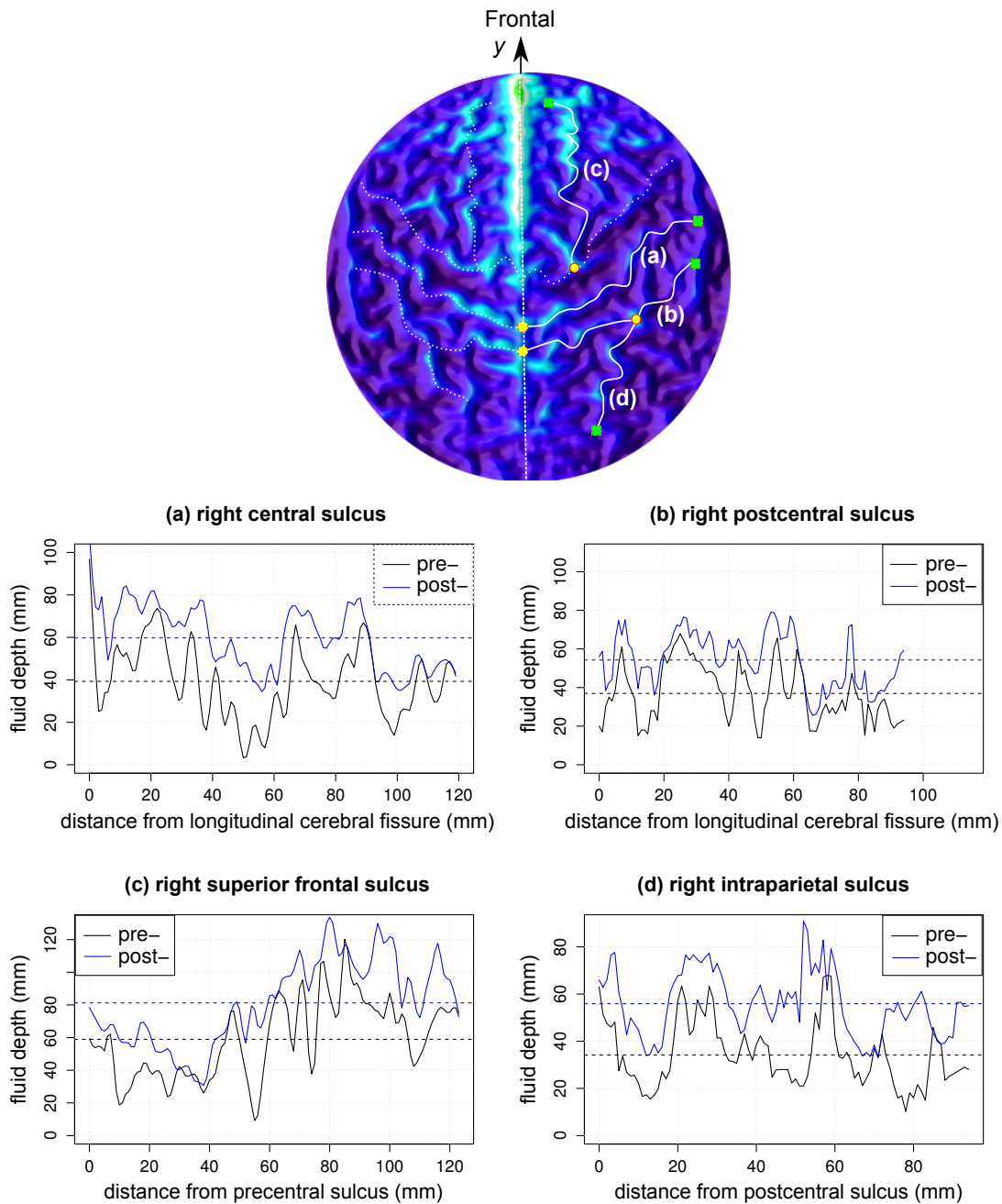


Figure 4.10 – Examples of the fluid distribution depths along some cerebral sulci for a communicating hydrocephalus patient before and after surgery (Fig. 4.9). Considered cerebral sulci are: right central cerebral sulcus (a), right precentral sulcus (b), right superior frontal sulcus (c) and right intraparietal sulcus (d), each of which is drawn as a white curve starting at an orange circle to a green square.

4.4.2 Moment-based analysis of the fluid distribution

In order to assist experts to confirm their visual analysis of volumetric relief maps, we extract geometric characteristics of a fluid distribution from each map using a moment-based approach.

Notions of moments

Moments, first introduced by Hu [73], provide efficient descriptors to represent a shape, and have been widely used in medical image analysis applications such as to describe cerebral sulci in [109] or to characterize cerebral aneurisms [121]. In this study, we use two-dimensional geometric moments to characterize a fluid distribution in the superior cortical subarachnoid space. A complete study of moment-based techniques can be found in Flusser et al. [46].

Considering a two-dimensional digital image $g(x, y)$ of size $N \times M$, the moment m_{pq} of order $p + q$ is defined as:

$$m_{pq} = \sum_{y=0}^{M-1} \sum_{x=0}^{N-1} x^p y^q g(x, y).$$

Basic features of a shape can be computed from low-order moments as follow.

The zeroth order moment m_{00} clearly represents the total mass of the distribution function $g(x, y)$.

The two first order moments m_{10} and m_{01} are used to calculate the coordinates of the center of mass $\mathbf{C} = (C_x, C_y)$ such that

$$C_x = \frac{m_{10}}{m_{00}} \text{ and } C_y = \frac{m_{01}}{m_{00}}.$$

If an object is positioned such that its center of mass is coincident with the origin, namely $C_x = 0$ and $C_y = 0$, then the moments are also called central moments, and denoted by μ_{pq} . Here, we use the central moments by translating all the coordinates (x, y) by $-\mathbf{C} = (-C_x, -C_y)$ for more than one order moments.

The second order central moments, μ_{02} , μ_{11} and μ_{20} , sometimes called moments of inertia, are used to calculate the principal axis of the image, around which there is the minimum second moment. More concretely, the moments determine the covariance matrix $\begin{pmatrix} \mu_{20} & \mu_{11} \\ \mu_{11} & \mu_{02} \end{pmatrix}$, and by using the eigenvector with the corresponding eigenvalue that has the largest absolute value, the orientation of the principal axis can be obtained. This orientation is given relative to the x -axis and can be also calculated directly from:

$$\theta = \frac{1}{2} \arctan \frac{2\mu_{11}}{\mu_{20} - \mu_{02}}.$$

The two third order central moments, μ_{30} and μ_{03} , describe the skewness of the image projections to the x - and y -axes, respectively, each of which measures a distribution's degree of deviation from symmetry about the center of mass on the axis. The coefficients of skewness are given by:

$$Sk_x = \frac{\mu_{30}}{\mu_{20}^{3/2}} \text{ and } Sk_y = \frac{\mu_{03}}{\mu_{02}^{3/2}}.$$

Moment-based features of synthetic relief maps

Relevance of using low-order geometric moments was tested on synthetic volumetric maps (f_1 to f_6) initialized with the same width (203 pixels) as illustrated in Fig. 4.11. These relief maps depict distributions that may be observed for the cerebrospinal fluid within the superior cortical subarachnoid space: f_1 represents a control (or "healthy adult") distribution while the others reflect different pathological distributions. Distributions of centers of mass and skewnesses are respectively shown in Fig. 4.12 and 4.13, and orientations are given in Table 4.2.

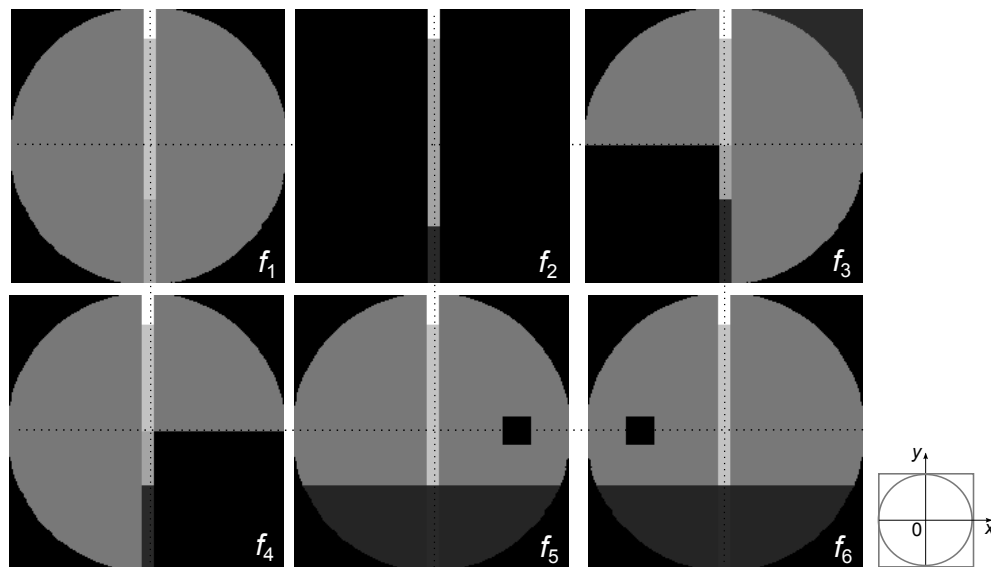


Figure 4.11 – Examples of synthetic volumetric relief maps (f_1 to f_6). f_1 is a control distribution and f_2 to f_6 reflect different pathological distributions.

It is observed that the control distribution f_1 (green square) has a center of mass located at the origin, its skewness coefficients are all zero and its orientation is 90 degrees. On the other hand, the other distributions (f_2 to f_6) have scattered centers of mass illustrated in red circles, with moderate skewness coefficients and different orientations.

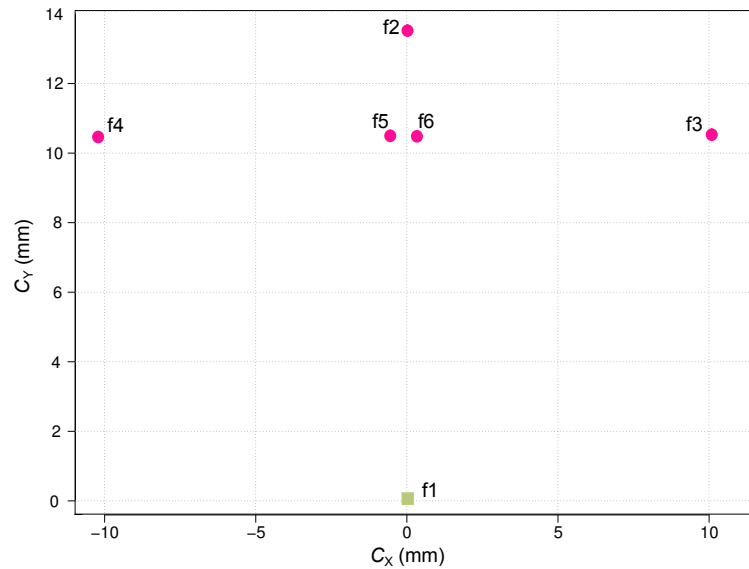


Figure 4.12 – Distribution of the centers of mass for synthetic volumetric relief maps (f_1 to f_6). The control distribution f_1 is represented by a green square and distributions f_2 to f_6 by red circles.

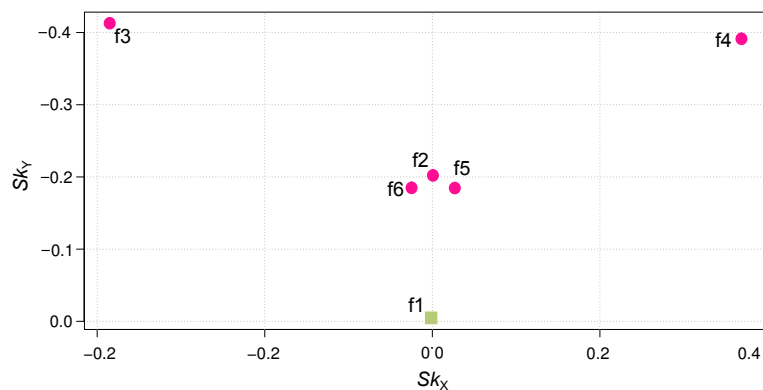


Figure 4.13 – Distribution of skewnesses for synthetic volumetric relief maps (f_1 to f_6). The control distribution f_1 is represented by a green square and distributions f_2 to f_6 by red circles.

Table 4.2 – Orientations calculated from synthetic volumetric relief maps (f_1 to f_6).

Image	f_1	f_2	f_3	f_4	f_5	f_6
Orientation (degrees)	90	90	-45.74	133.46	178.71	1.28

Moment-based features of the fluid distribution

Quantitative assessments on the clinical dataset were carried out by calculating low order geometric moments for each volumetric relief map, *i.e.*, the center of mass, principal axis and skewness coefficients. Results are summarized in Table 4.3.

First, the resulting distribution of centers of mass for healthy adults and pathological cases is shown in Fig. 4.14. Regarding the distribution, healthy adults have the average center of mass close to the relief map center. In contrast, every hydrocephalus patient has a fluid distribution more or less depleted in the posterior and lateral regions of the brain, with larger deviations around the longitudinal cerebral fissure than healthy adults. This confirms the visual analysis, which indicates the decrease of cerebrospinal fluid inside sulci as shown in Section 4.4.1. The relative change of the averages of centers of mass between healthy adults and patients is -80% along the vertical axis of the map.

Concerning distributions of principal axes for healthy adults and pathological cases, both of their averages are almost along the longitudinal cerebral fissure and are oriented towards the frontal region; there are very few patients who have orientations differing from that of the longitudinal cerebral fissure. This indicates that the principal axis, *i.e.*, the fluid distribution orientation, may not be a relevant discriminant factor when volumetric relief maps are used. Compared to the principal axis of an original three-dimensional image, we may lose the depth information that is different between healthy adults and hydrocephalus patients. Indeed, healthy adults tend to have their major axes oriented towards the frontal regions parallel to an axial plane, while major axes of patients also tend to be oriented toward the frontal regions but slightly decline to their lower parts; it is obvious that this distinction is impossible when volumetric relief maps are used.

Finally, the skewness coefficients exhibit that the fluid distribution has a low degree of deviation from symmetry about the center of mass for a healthy adult. On the other hand, hydrocephalus patients have moderate asymmetry towards the frontal region of the longitudinal cerebral fissure, indicated by negative skewness coefficients Sk_y . Differently from Sk_y , Sk_x varies in signs. Furthermore, the sign of Sk_x seems to depend on the sign of C_x of the center of mass (C_x, C_y); $Sk_x < 0$ if $C_x > 0$ and $Sk_x > 0$ if $C_x < 0$. In fact, Fig. 4.15 illustrates that the absolute value

of each skewness coefficient increases with respect to the distance from the center of mass to the average center of mass of healthy adults. Let d be the distance from each center of mass (C_x, C_y) to the average center of mass of healthy adults. Given a set of the skewness coefficients Sk_x and Sk_y , as well as a set of associated distances d , we make polynomial regression that fits a nonlinear model to them. This results in the following quadratic models using an ordinary least squares method [94]:

$$\begin{cases} Sk_x = -0.0113d + 0.0002d^2 & \text{if } C_x > 0, \\ Sk_x = 0.0134d - 0.0002d^2 & \text{otherwise,} \end{cases}$$

$$Sk_y = -0.0448d + 0.0005d^2.$$

From these models, we can conclude that asymmetry of fluid distribution increases with depletion in the posterior regions of the brain if the fluid is increasingly concentrated in the frontal part of the longitudinal cerebral fissure.

Table 4.3 – Means with standard deviations of the low order moment-based features calculated from volumetric relief maps for healthy adults and pathological cases, respectively.

Order	Feature	Class	Value
0	volume (cm ³)	healthy	237 ± 51
		pathological	200 ± 83
1	center of mass (mm)	healthy	$C_x = 0.70 \pm 0.77; C_y = 2.33 \pm 2.70$
		pathological	$C_x = 0.91 \pm 2.71; C_y = 12.75 \pm 5.47$
2	orientation (degrees)	healthy	$\theta = 92 \pm 7$
		pathological	$\theta = 94 \pm 51$
3	skewness	healthy	$ Sk_x = 0.03 \pm 0.02; Sk_y = -0.08 \pm 0.09$
		pathological	$ Sk_x = 0.09 \pm 0.06; Sk_y = -0.42 \pm 0.21$

In summary, the center of mass and the skewness, to a lesser extent, could be both relevant discriminant factors to distinguish between healthy adults and hydrocephalus patients. Furthermore, we corroborated these results, *i.e.*, the average center of mass and skewness for healthy adults, with those obtained with healthy volunteers from the OASIS dataset [113].

4.4.3 Descriptive discriminant analysis

A descriptive discriminant analysis [65] was performed on the clinical dataset using the coordinates of centers of mass as the input variables. The software package R [140] was used for this analysis.

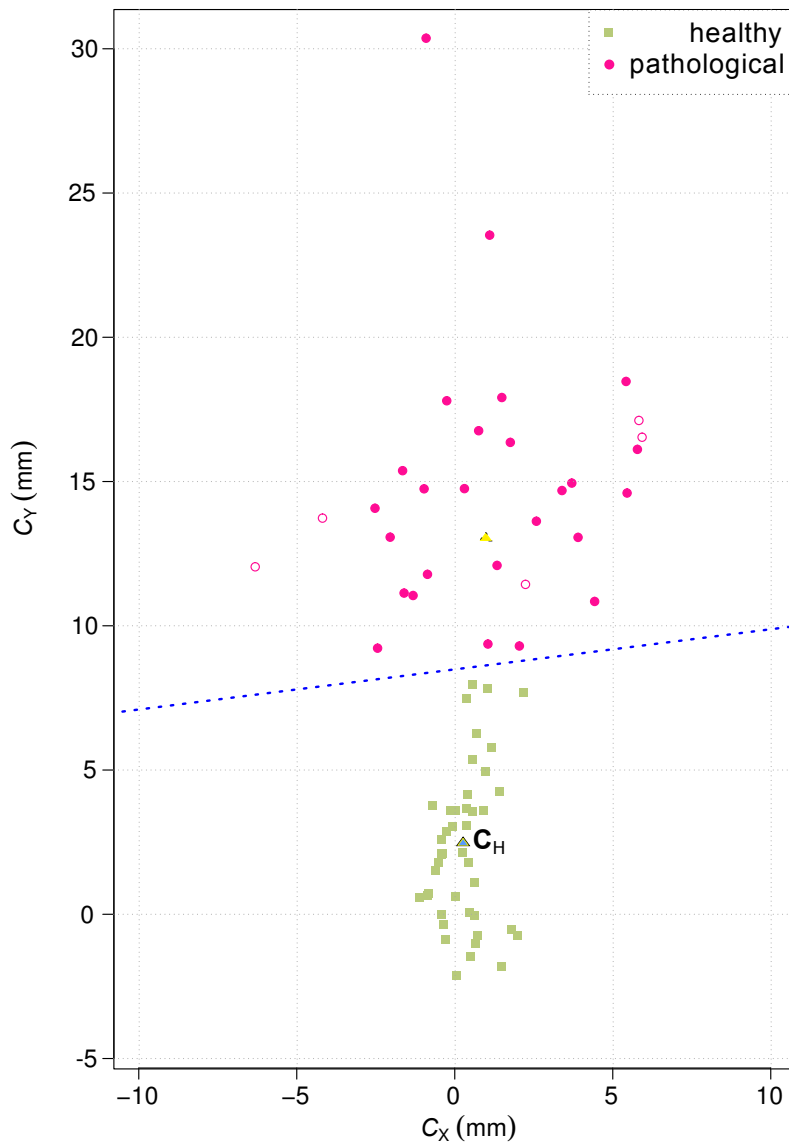


Figure 4.14 – Distribution of the centers of mass for the clinical dataset with its descriptive discriminant analysis. The dotted line ($C_Y = 0.161C_X + 8.39$), resulting from the discriminant analysis, indicates the limit values from which the centers of mass can be distinguished between healthy adults and hydrocephalus patients. Healthy adults have an average center of mass C_H close to the relief map center (bottom blue triangle). In contrast, hydrocephalus patients have fluid distributions depleted in the posterior region of the brain, with larger deviations around the longitudinal cerebral fissure than healthy adults (the average is illustrated by the top yellow triangle; the centers of mass for non-communicating hydrocephalus patients are distinguished from those for communicating ones by red non-filled circles).

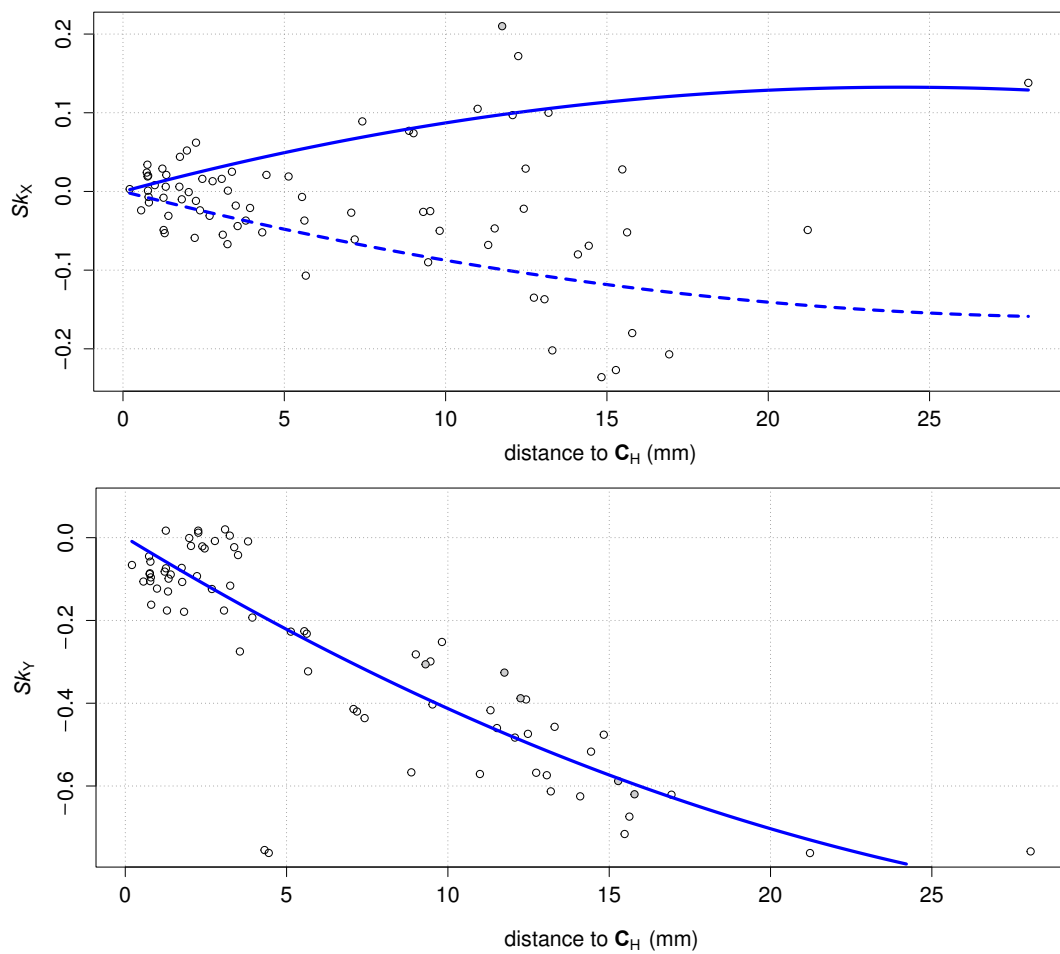


Figure 4.15 – Evolution of the skewness coefficients Sk_x (top) and Sk_y (below) relatively to the distance d to the average center of mass for healthy adults C_H . The quadratic regression between Sk_x and d gives: $Sk_x = -0.0113d + 0.0002d^2$ if $C_x > 0$ (dashed line), $Sk_x = 0.0134d - 0.0002d^2$ if $C_x < 0$ (solid line), and the one between Sk_y and d gives: $Sk_y = -0.0448d + 0.0005d^2$.

We consider two classes: healthy adults and pathological cases (containing communicating and non-communicating hydrocephalus cases). The Wilks' lambda was significant ($= 0.2114$) with the p -value of $2.2e - 16$. Thus, with a significance level of 0.001, this test indicated that the coordinates of centers of mass differentiated between healthy adults and pathological cases.

The distinction between pathological cases and healthy adults results in 100% for all of sensitivity S_e , specificity S_p and F_1 -score. This analysis is efficient to discriminate between the above two classes; it remains to be confirmed with a larger number of data.

4.4.4 Monitoring of patients

Figures 4.16 and 4.17 respectively show the distribution of centers of mass and the evolution of the skewness coefficients for eight patients who had magnetic resonance image acquisitions before and after their surgery. We observe that all patients after surgery have their centers of mass recovered to acceptable values and that their skewness coefficients have decreased following the models presented in Section 4.4.2. The predicted classification between patients before and after surgery is performed by using processed data in Section 4.4.3 as a training set for the linear discriminant analysis. This results in 100% for all of the sensitivity S_e , specificity S_p and F_1 -score, and indicates its efficiency to discriminate between the classes and also to perform patient monitoring before and after surgery. Certainly, this remains to be confirmed with a larger number of data.

4.5 CONCLUSION

This chapter used pre-segmented magnetic resonance images of the cerebrospinal fluid, and introduced a two-dimensional image representation of the fluid volume distribution within the superior cortical subarachnoid space, called a volumetric relief map. Volumetric relief maps are automatically retrieved through ray tracing and map projection techniques from a volume data. Maps provide efficient representations that are used to visualize, at a glance, a complex structure such as a fluid volume distribution within the cortical subarachnoid space. We also show that features of the fluid distributions on maps are extracted using image moments in low orders. In particular, volumetric relief maps show that distributions are balanced for healthy adults, *i.e.*, their centers of mass are close to the relief map center and their skewnesses hovers around zero. In contrast, hydrocephalus patients have fluid

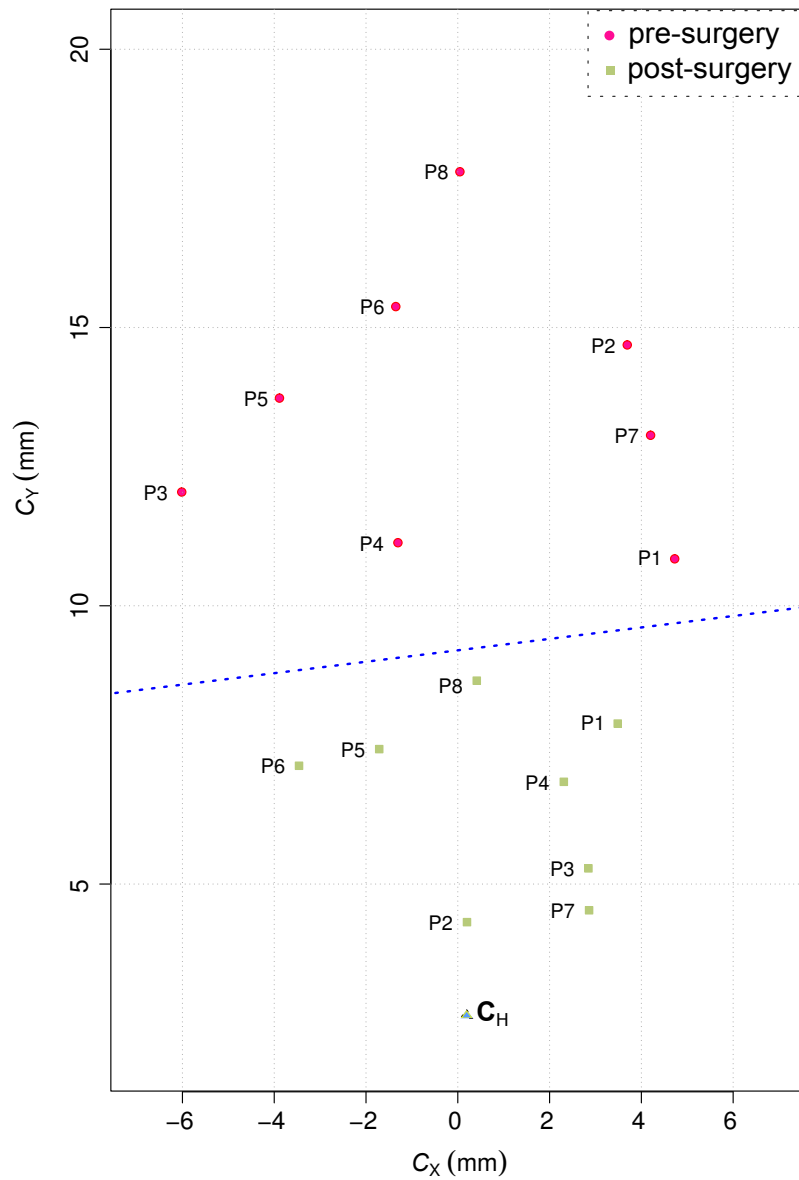


Figure 4.16 – Monitoring of the centers of mass for pre- and post-surgery patients. The dotted line ($C_Y = 0.161C_X + 8.39$), resulting from the discriminant analysis, indicates the border by which the centers of mass for the two classes (healthy adults and patients) can be separated. It follows that each patient has recovered a normal state after the surgery.

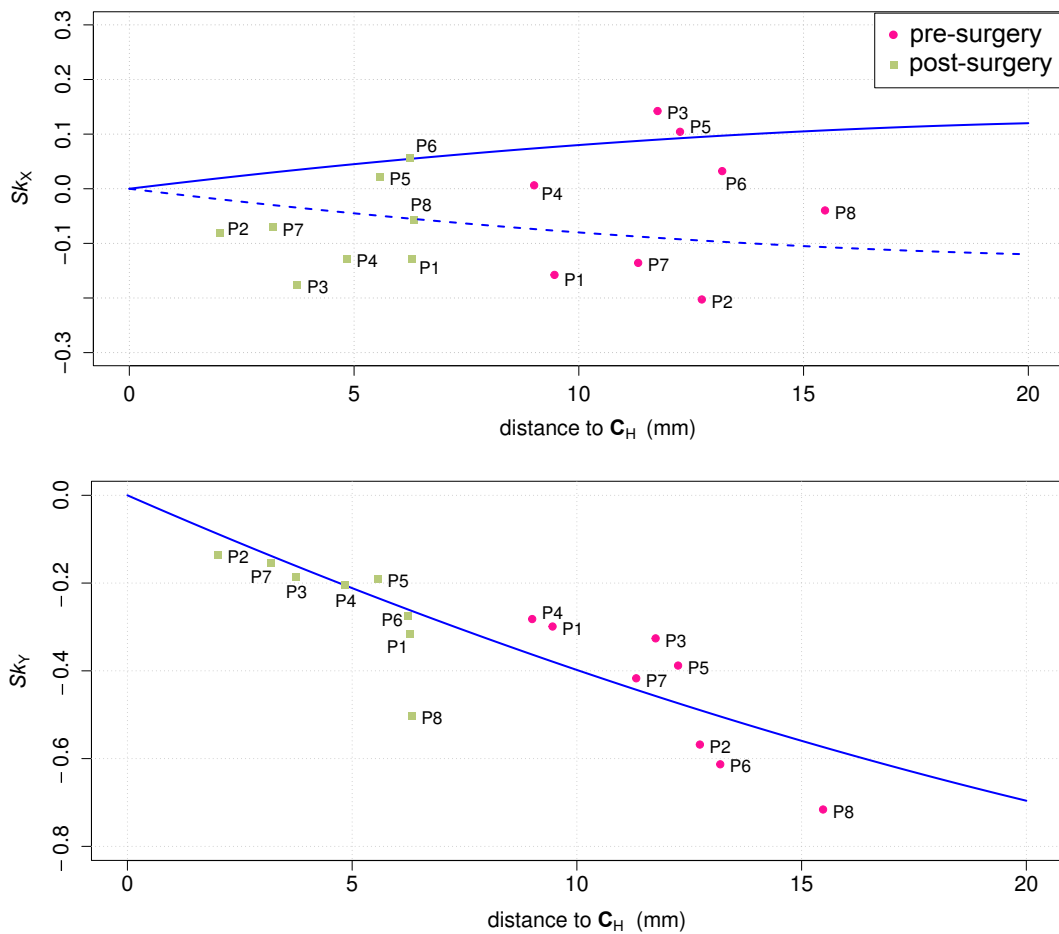


Figure 4.17 – Monitoring of the skewness coefficients for pre- and post-surgery patients with the calculated evolution models in Fig. 4.15. Every patient has recovered a normal state after the surgery.

distributions depleted in posterior regions of their brains with various asymmetries that increase with depletion, and that are oriented towards the frontal part of the longitudinal cerebral fissure. Indeed, the relative change of the averages of the centers of mass between healthy adults and patients is -80% along the vertical axis of the map. This result confirms that the above two moment-based features can be efficient discriminant factors to distinguish between healthy and pathological cases. This tool also allows to monitor a variation of the cerebrospinal fluid distribution within the superior cortical subarachnoid space, before and after surgery, on a patient suffering from hydrocephalus.

FLUID NETWORK OF THE CORTICAL SUBARACHNOID SPACE

CONTENTS

5.1	INTRODUCTION	79
5.2	VOXEL LABELING BY GEODESIC PROPAGATION FROM SEEDS	80
5.3	FLUID PATHWAYS FROM SEEDS AS “FLUID SOURCES”	81
5.3.1	Seeds setting and geodesic propagation	81
5.3.2	Visualization using volumetric relief map	83
5.4	DISTRIBUTION OF DEEP FLUID PATHWAYS FROM HOMOGENEOUSLY DIS- TRIBUTED SEEDS	87
5.4.1	Seeds setting	88
5.4.2	Generating a geodesic relief map	89
5.4.3	Deep fluid pathways distribution analysis	90
5.5	CONCLUSION	93

VOLUMETRIC relief maps serve to visualize and to characterize the cerebrospinal fluid volume distribution within the superior cortical subarachnoid space. However, such method disregards topological characteristic of the fluid, particularly within the cerebral sulci network. In this chapter, we suggest an additional method to focus on the fluid network within the cortical subarachnoid space.

5.1 INTRODUCTION

In Chapter 4, we proposed volumetric relief maps as a visualization and characterization tool. However, such map does not reflect any topological structure of the fluid distribution, despite its effective visualization of the geometric projection information. For example, with such a naive spherical projection, we obtain volumetric relief maps as shown in Fig. 5.1. Even if the two synthetic images have different topological structures inside the hemisphere, their distinction is doubtful by observing only those maps.

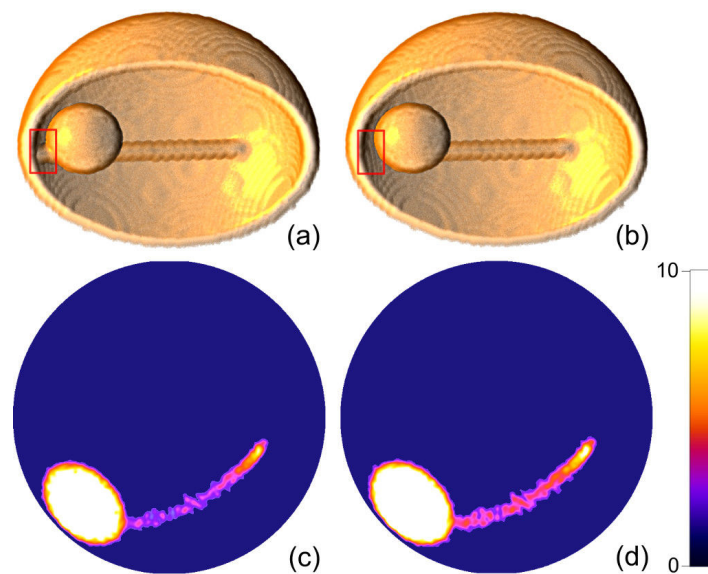


Figure 5.1 – Comparison of two synthetic images with their respective colored volumetric relief maps: image with two connected branches (a) and its associated map (c); image with a disconnected branch (b) and its associated map (d).

To take into account such topological information and to afford analysis of the fluid network, we use a geodesic distance defined only in the fluid region instead of the Euclidean distance defined in the whole space. Figure 5.2 illustrates Euclidean (dashed line) and geodesic (solid line) distances between points A and B in the cerebrospinal fluid.

Geodesic distance has been widely used in the medical image computing field. Although its main application remains segmentation [8, 136], it is also used to facilitate virtual endoscopy [34] and to perform parcellation of cortical brain from functional magnetic resonance imaging [45, 170]. In this work, we aim to study the cerebrospinal fluid network around the brain and within its sulci. Geodesic distance is used to trace every voxel in the fluid region from points close to the periphery of the fluid, called “seeds” in this chapter.

In Section 5.2, we present the voxel labeling method that performs geodesic

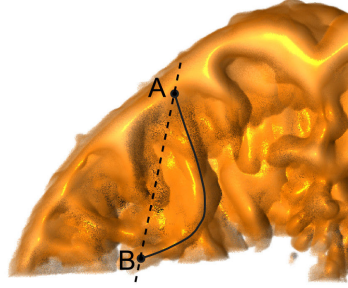


Figure 5.2 – Geometric (dashed line) and geodesic (solid line) distances between points A and B in the cerebrospinal fluid.

propagation from one or more seeds located close the periphery of the fluid. Then, we observe fluid propagations from those seeds chosen as “fluid sources” in Section 5.3, using volumetric relief maps for visualization. We show visual results for a healthy adult and a hydrocephalus patient before and after surgery. Section 5.4 is devoted to studying deep fluid pathways rather than network. Given a three-dimensional volume data of the cerebrospinal fluid within the superior cortical subarachnoid space, we introduce an additional two-dimensional image representation, called *geodesic relief map*, obtained with an automatic geodesic propagation from homogeneously distributed seeds.

5.2 VOXEL LABELING BY GEODESIC PROPAGATION FROM SEEDS

Let D be a set of seeds located within the fluid region V and close to its periphery for example. Assuming that each valid seed $\mathbf{s} \in D$ has a different label, every label is then diffused in voxels $\mathbf{v} \in V$ by considering a geodesic distance between the seed \mathbf{s} and \mathbf{v} as follows.

Let $\mathcal{P} = (\mathbf{v}_1, \mathbf{v}_2, \dots, \mathbf{v}_n)$ be a path between voxels \mathbf{v}_1 and \mathbf{v}_n in V , such that \mathbf{v}_i and \mathbf{v}_{i+1} are adjacent (6-, 18- or 26-adjacent) for $i \in \{1, 2, \dots, n-1\}$, and $\mathbf{v}_i \in V$ for all i . In this work, we set the length of \mathcal{P} , $l(\mathcal{P})$ to be $n-1$, *i.e.*, the number of edges of the adjacency graph. Let us consider the set $\Pi(\mathbf{u}, \mathbf{v})$ of all the paths between \mathbf{u} and \mathbf{v} in V . Then, the geodesic distance between \mathbf{u} and \mathbf{v} is defined by

$$d(\mathbf{u}, \mathbf{v}) = \min_{\mathcal{P} \in \Pi(\mathbf{u}, \mathbf{v})} l(\mathcal{P}).$$

The path that has the minimum length is called the “shortest path”. There may be several shortest paths for given \mathbf{u} and \mathbf{v} [25, Chapters 24, 26].

Now let us consider for each voxel $\mathbf{v} \in V$ such that the seed $\mathbf{s} \in D$ provides a shortest path to \mathbf{v} . In fact, we attribute the label of the closest seed, in the sense of the geodesic distance defined above, to each $\mathbf{v} \in V$ as shown in Fig. 5.3(a).

Note that there may be several seeds that have the same geodesic distance to \mathbf{v} as illustrated in Fig. 5.3(b); in this case, we accept to attribute all the labels to \mathbf{v} (multi-labeling), by setting the set of seeds having the shortest paths to \mathbf{v} by

$$M(\mathbf{v}) = \operatorname{argmin}_{\mathbf{s} \in D} d(\mathbf{v}, \mathbf{s}).$$

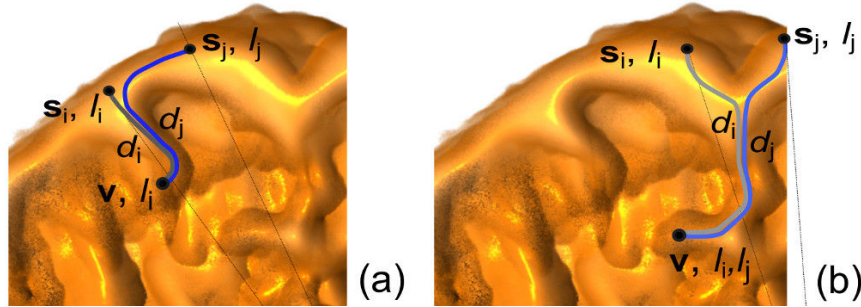


Figure 5.3 – Voxel labeling using geodesic propagation from seeds with a unique minimum distance $d_i < d_j$ (a), or more equal minimum distances $d_i = d_j$ (d).

This multi-labeling does not cause any problem whereas the interest is not to realize a segmentation but plainly to associate voxels to seeds or distances themselves. For each voxel $\mathbf{v} \in V$, we can define a distance $Dis(\mathbf{v}) = \min_{\mathbf{s} \in D} d(\mathbf{v}, \mathbf{s})$ which is called a geodesic distance map. For computing such geodesic voxel propagation from seeds, we currently use an algorithm which is similar to the classical fast marching algorithm based on front propagation presented in Sethian [155], or the Dijkstra algorithm [25, Chapter 24]. As we have a set of seeds and take a graph-based approach, the computation can be made more efficiently by using the framework of image foresting transform [43].

5.3 FLUID PATHWAYS FROM SEEDS AS “FLUID SOURCES”

In this section, we observe the fluid propagation pathways from a given single seed chose close to arachnoid granulation areas along the longitudinal cerebral fissure, and from several seeds located on the boundary of the hemisphere basis and then projected onto the cerebrospinal fluid volume. Geodesic distance maps are calculated from initial regions, *i.e.*, the single seed or set of seeds, by using the previous voxel labeling technique. Distance maps are then thresholded at each unit distance to get binary images, for which we generate volumetric relief maps.

5.3.1 Seeds setting and geodesic propagation

As discussed in Chapter 2, the cerebrospinal fluid circulates from the ventricular space to the superior cortical subarachnoid space where it is drained through

arachnoid granulations. We might be tempted to limit the fluid propagation analysis to the set of seeds located on the boundary of the hemisphere basis. However, such seeds compete while searching pathways so they may provide average information about propagation. For this reason, we first use a single seed positioned farthest from all actual fluid sources, that is to say close the projection of the pole of the hemisphere.

Single seed initialization

A single seed s is initialized as a “fluid source” by the user, directly on the initial three-dimensional image of the cerebrospinal fluid volume, or by selecting a pixel in the target relief map (see Section 5.4). In the following examples (Fig. 5.5 and 5.7), the seed is initially chosen close to the projection of the center hemisphere, closely to fluid flow outputs, *i.e.*, arachnoid granulations areas (see [57] for localization of arachnoid granulations in the superior cortical subarachnoid space).

Several seeds initialization

Under normal conditions, it is known that the fluid flow follows a reverse propagation from the inferior regions of the cortical subarachnoid space to arachnoid granulations located along the longitudinal cerebral fissure [57]. According to this, we automatically initialize a set of N seeds s_i ($i = 1$ to N) as “fluid sources” as follows. As illustrated in Fig. 5.4, seeds are positioned on the boundary of the upper hemisphere basis and are projected to the cerebrospinal fluid volume by using the same technique detailed in Section 5.4.1.

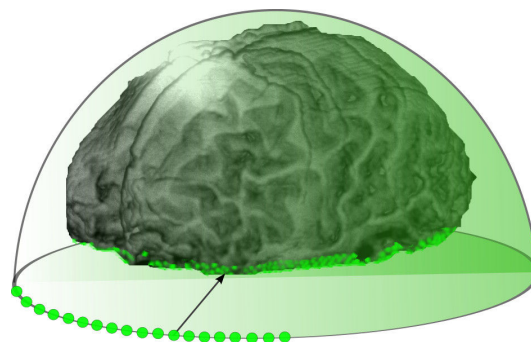


Figure 5.4 – Initialization of seeds on the bottom periphery of the cortical subarachnoid space before geodesic propagation.

Geodesic distance map

A geodesic distance map is then computed from the initial regions, *i.e.*, the single seed or set of seeds, by iteratively perform a voxel labeling (see Section 5.2) on the 26-neighborhood of the considered region.

5.3.2 Visualization using volumetric relief map

We produce a series of volumetric relief maps such as a series of thresholded images obtained from the geodesic distance maps by increasing the distance threshold from zero to its maximum value within the fluid.

Figures 5.5 and 5.6 show sequence examples of the cerebrospinal fluid propagation for a healthy adult, respectively from a single seed located closely to the top projection of the hemisphere (white arrow), and from several seeds uniformly positioned along the boundary of the hemisphere basis. Sequences interval in the figures is ten. The front propagation [155], which is a set of voxels with threshold distance, is highlighted in hot orange. We observed that, for healthy adults, the fluid propagates uniformly in every direction from the chosen seeds, filling cerebral sulci first, then spaces among them as shown in Fig. 5.5 and 5.6. Regardless the selection of seeds, larger cerebral sulci, especially the longitudinal cerebral fissure, seem predominant while fluid propagation steps as illustrated by red arrows.

In contrast, we noted that for hydrocephalus patients, an asymmetrical diffusion occurs mainly along the entire longitudinal fissure when propagating from a single source as shown in Fig. 5.7(a). Figures 5.7(a) and 5.8(a) respectively show a discontinuous front propagation and reflect the gradually and oscillatory propagation process, from a single seed, and from several sources. After surgery (see Fig. 5.7(b) and 5.8(b)), patients recover a more consistent front propagation from the chosen seeds.

Figures 5.9 and 5.10 illustrate the evolution of centers of mass and orientations for sequences of the fluid distribution from a single seed shown in Fig. 5.5 and 5.7 (a, b). For the healthy adult (dashed blue line), the initial seed was set slightly above the center of the map along the longitudinal cerebral fissure. We observe that the center of mass and orientation are smoothly adjusted to their final values. On the contrary, the hydrocephalus patient before (red line) and after (green line) surgery has his initial seed located substantially below the center of the map. This initial position is set in the region corresponding with healthy adults as shown in Chapter 4. In the previous chapter, we also reported that hydrocephalus patients are characterized by a center of mass shifted towards the frontal region and with

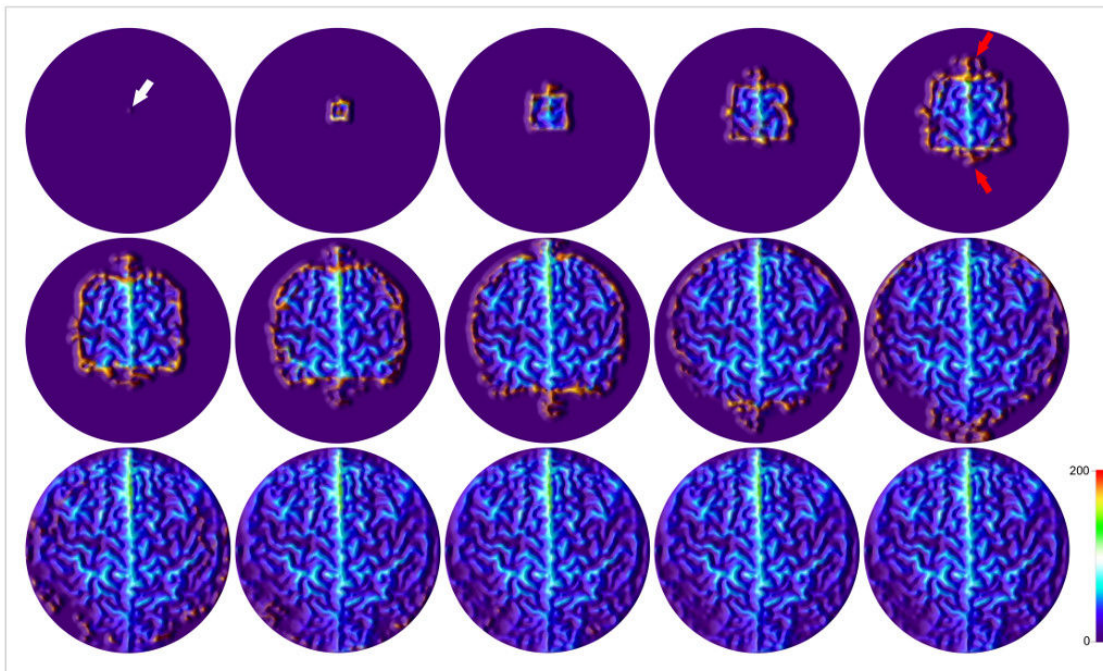


Figure 5.5 – Colored volumetric relief map sequence illustrating propagation within cerebrospinal fluid from a seed located close to the top projection of the hemisphere (white arrow) for a healthy adult. The sequence begins at a distance $d = 0$ with an increment of 10, and the front propagation is colored in hot orange. Larger cerebral sulci, particularly the longitudinal cerebral fissure, are predominant in the fluid propagation (red arrows).

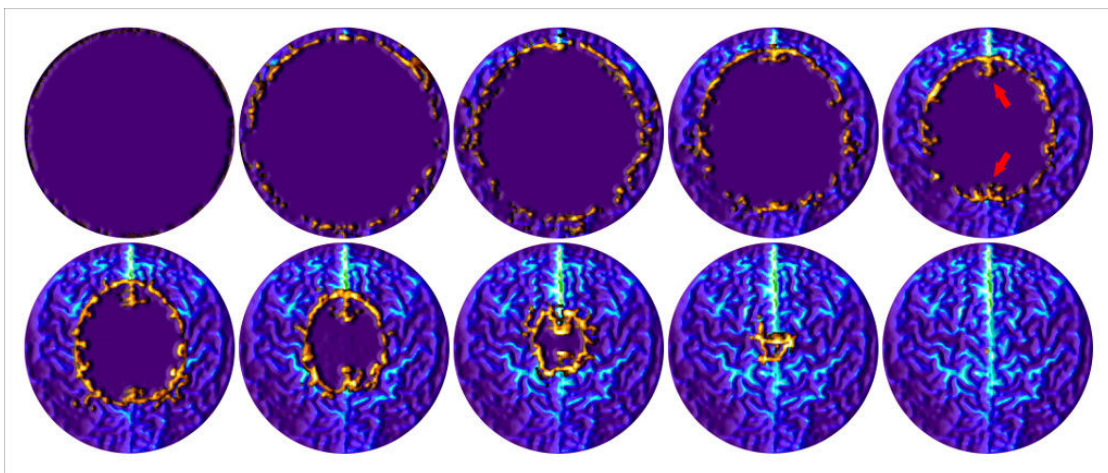


Figure 5.6 – Colored volumetric relief map sequence illustrating propagation within cerebrospinal fluid from several seeds located on the boundary of the relief map for a healthy adult. The sequence begins at a distance $d = 0$ with an increment of 10, and the front propagation is colored in hot orange. Larger cerebral sulci, particularly the longitudinal cerebral fissure, are predominant in the fluid propagation (red arrows).

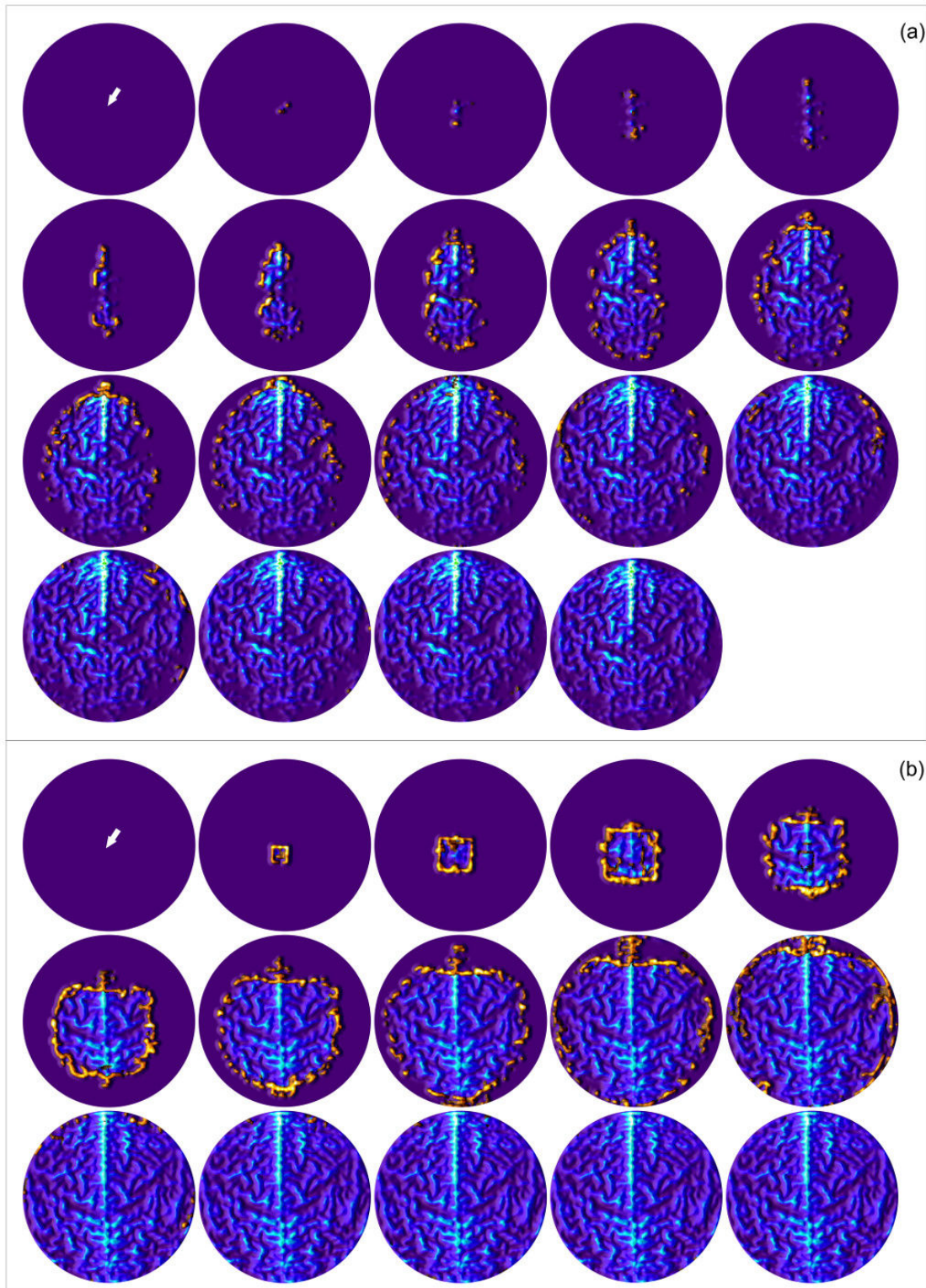


Figure 5.7 – Colored volumetric relief map sequences illustrating single seed propagation within cerebrospinal fluid from a seed located close to the top projection of the hemisphere center for a hydrocephalus patient (white arrow) before (a) and after (b) surgery. Each sequence begins at a distance $d = 0$ with an increment of 10, and the front propagation is colored in hot orange.

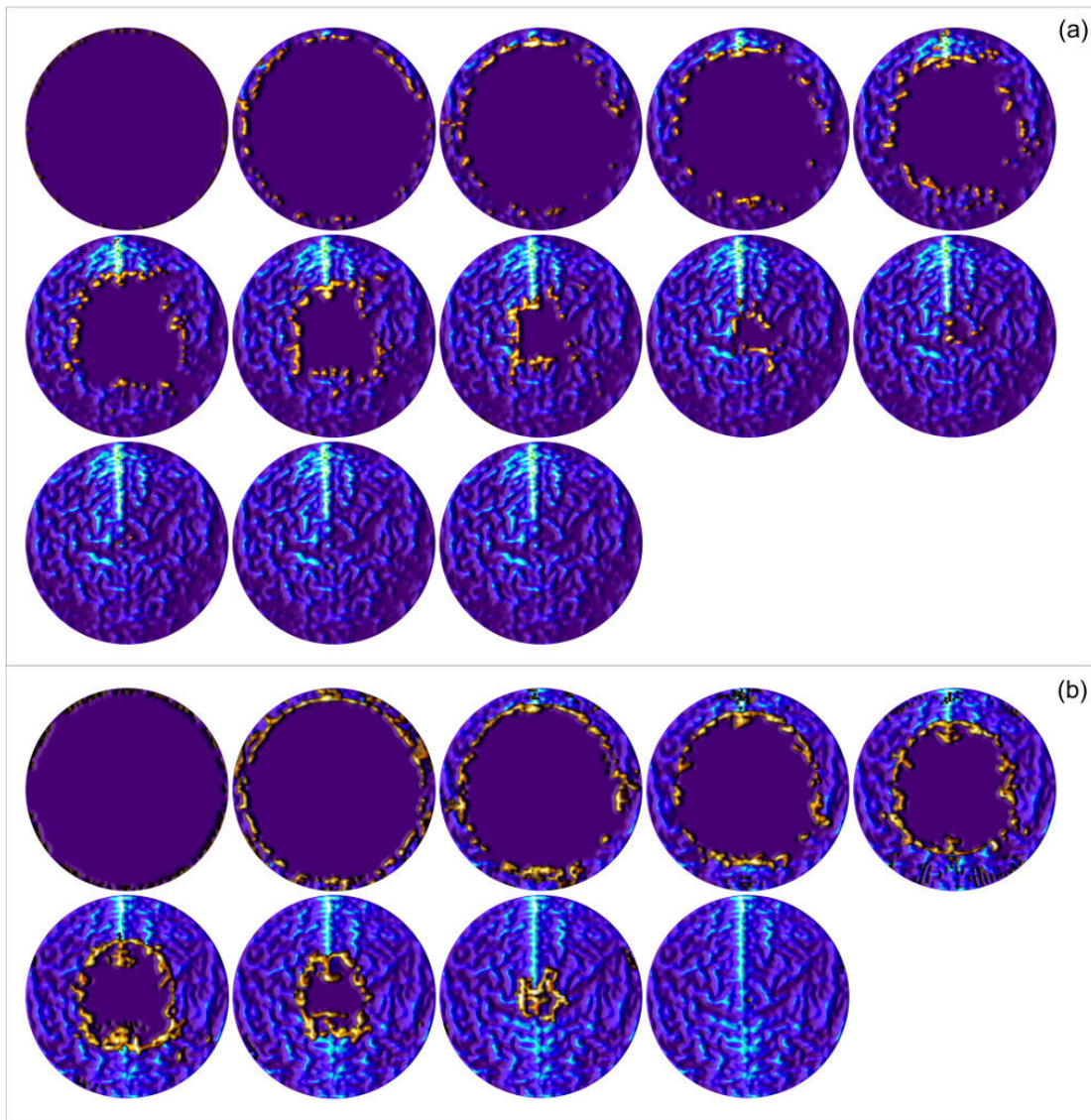


Figure 5.8 – Colored volumetric relief map sequences illustrating propagation within cerebrospinal fluid from several seeds located on the periphery of the relief map for a hydrocephalus patient before (a) and after (b) surgery. Each sequence begins at a distance $d = 0$ with an increment of 10, and the front propagation is colored in hot orange.

moderate skewness coefficients. Evolutions of the center of mass and orientation for the patient before surgery confirm this prior characterization. Furthermore, these evolutions also corroborate the previous visual analysis of gradually and oscillatory propagation process caused by the search of fluid pathways. Finally, we noticed that the maximum distance for the fluid to propagate to the entire space from a single seed, or several ones, is larger by approximately one-third for hydrocephalus patients than for healthy adults. After surgery, patients return to similar propagation steps than healthy adults.

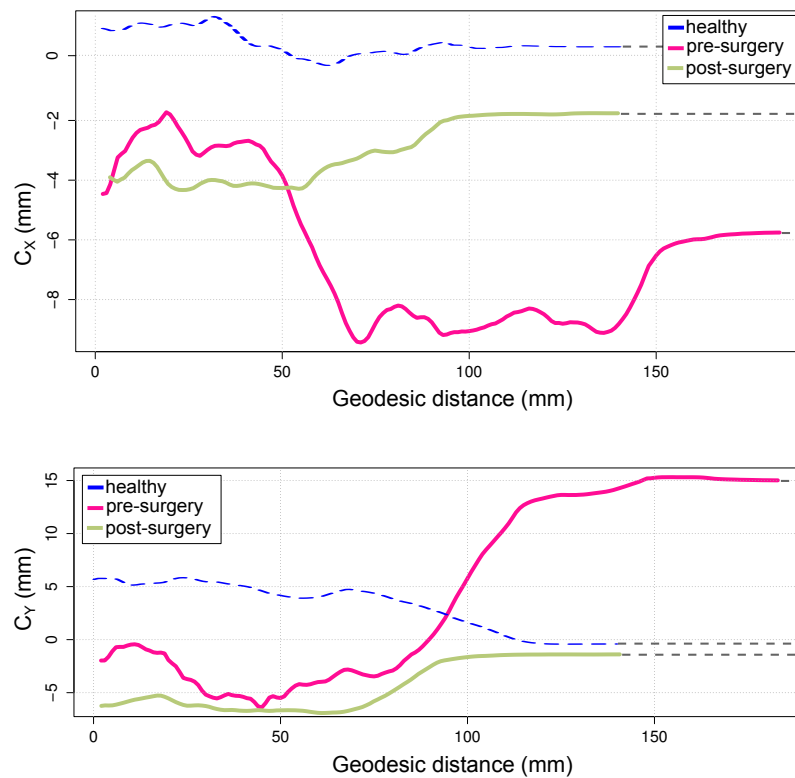


Figure 5.9 – Evolution of the fluid distribution center of mass using geodesic propagation from a single seed, for a healthy adult (blue dashed line) and a hydrocephalus patient before (red line) and after (green line) surgery.

5.4 DISTRIBUTION OF DEEP FLUID PATHWAYS FROM HOMOGENEOUSLY DISTRIBUTED SEEDS

In this section, we observe the fluid propagation from a set of homogeneously distributed seeds automatically generated on a targeted relief map. This results in two-dimensional digital images, called *geodesic relief maps*, which inform on the topological structure of the cerebrospinal fluid network and the distribution of

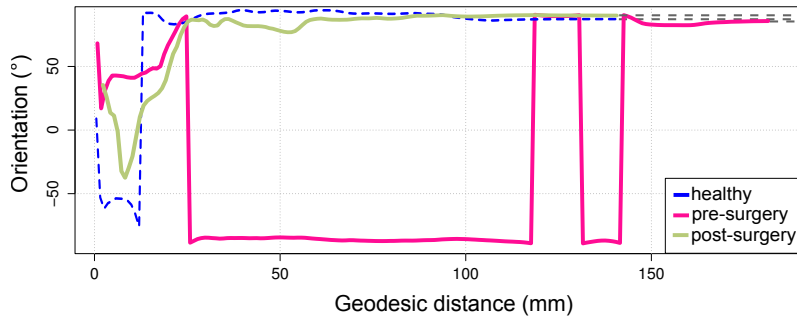


Figure 5.10 – Evolution of the fluid distribution orientation using geodesic propagation from a single seed, for a healthy adult (blue dashed line) and a hydrocephalus patient before (red line) and after (green line) surgery.

deep fluid pathways within the fluid network. This distribution may also be characterized as volumetric relief maps using a moment-based analysis (see Chapter 4).

5.4.1 Seeds setting

Generating points in a two-dimensional plane

A geodesic relief map is defined as a two-dimensional digital image of size $(N + 1) \times (N + 1)$ that contains a digitized disc positioned at the image center with the maximum radius. This disc is used later for mapping points from a two-dimensional plane to the hemisphere that covers the superior cortical subarachnoid space. Here, we focus on how to generate relief map points as sampling points on the planar image. In fact, the center point of every pixel in the digitized disc is considered to be a geodesic relief map point, so that the size of a map and the radius of the contained disc automatically provide us the two-dimensional coordinates of all relief map points $\mathbf{P} = (X, Y)$ on the grid. To simplify the successive explanations, we set the radius of the disc to be $\sqrt{2}r$ so that the square grid length (*i.e.*, pixel size) is considered to be $\frac{2\sqrt{2}r}{N}$ as illustrated in Fig. 5.11(a). Note that all pixel values of this two-dimensional image are initialized to be zero.

Mapping seeds from the plane onto the hemisphere

All the geodesic relief map points \mathbf{P} on the plane are now projected on an upper hemisphere. For this aim, we use the inverse of the Lambert azimuthal equal-area projection [16, Chapter 3].

The following formulas are applied for each point on the plane $\mathbf{P} = (X, Y)$ located in the disc with center at the origin and radius $\sqrt{2}r$ to obtain the corre-

sponding three-dimensional coordinates $\mathbf{p} = (x, y, z)$ on the upper hemisphere such that $(x - c_x)^2 + (y - c_y)^2 + (z - c_z)^2 = r^2$ and $z \geq c_z$:

$$\begin{aligned} x &= \sqrt{2r - \frac{X^2 + Y^2}{4r^2}}X + c_x, \\ y &= \sqrt{2r - \frac{X^2 + Y^2}{4r^2}}Y + c_y, \\ z &= r - \frac{X^2 + Y^2}{2r} + c_z. \end{aligned}$$

With those formulas, the geodesic relief map points \mathbf{P} in the disc with center at the origin and radius $\sqrt{2}r$ are projected on the upper hemisphere with center at the origin and radius r , as illustrated in Fig. 5.11(b).

Moving seeds on the superior subarachnoid space

Generated points are now on the upper hemisphere, but not yet in a given volume data V of the cerebrospinal fluid. In order to apply a geodesic propagation method for voxel labeling from seeds, those seeds must be in this fluid region V . In this perspective, we draw a three-dimensional discrete ray from each point \mathbf{p} toward the hemisphere center \mathbf{c} by using a technique of discrete ray traversal proposed in Yagel et al. [185]. This allows to find the first discrete seed \mathbf{s} along this discrete ray, which belongs to V as the new seed position as illustrated in Fig. 5.11(c, d). Such a discrete ray can be defined depending on connectivity of voxels [23], and in this chapter we choose the 26-connectivity as we know that the pre-segmented fluid region V is 6-connected.

When a discrete ray, drawn from a point \mathbf{p} , does not encounter any voxel of V , we say that \mathbf{p} is not valid and ignore it for the following procedure. It may also happen that a discrete ray finds \mathbf{s} located far inside the hemisphere as for some pathological cases. In order to avoid such a case, we define an allowed search depth from an encompassing ellipsoid.

5.4.2 Generating a geodesic relief map

We finally obtain a geodesic relief map as a two-dimensional image as follows. As each pixel corresponds to a seed $\mathbf{s} \in D$, for each seed \mathbf{s} , we first obtain the set of voxels that are associated to \mathbf{s} such that

$$A(\mathbf{s}) = \{\mathbf{v} : \mathbf{s} \in M(\mathbf{v})\}.$$

Then, we count the number of associated voxels to s by considering the multi-labeling such as $\sum_{v \in A(s)} \frac{1}{|M(v)|}$. This value corresponds to the pixel value of a geodesic relief map, which indicates a “depth” of the fluid region projected on the hemisphere by using a geodesic metric as shown in Fig. 5.11(c, d). The geodesic relief map has the property that the total amount of “depths” in the map is equal to the volume of the initial three-dimensional voxel set.

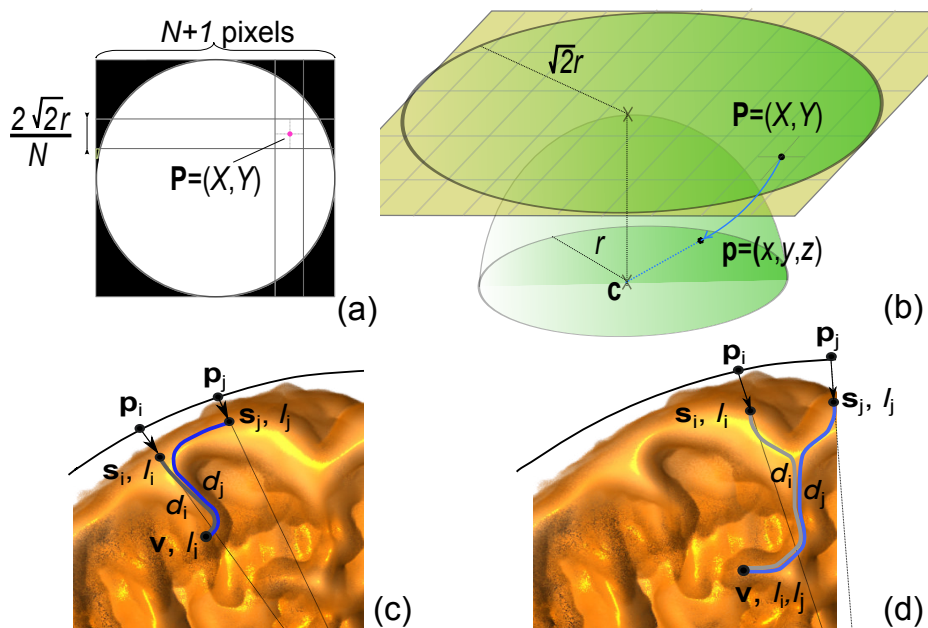


Figure 5.11 – Steps of the geodesic relief map generation: generating points \mathbf{P} in a two-dimensional grid (a); mapping points \mathbf{P} from the plane to their corresponding points \mathbf{p} onto the hemisphere using the inverse Lambert azimuthal equal-area projection (b); moving points on the superior cortical subarachnoid space using a discrete ray tracing technique and labeling voxels by geodesic propagation from seeds with a unique minimum distance $d_i < d_j$ (c), or equal minimum distances $d_i = d_j$ (d).

5.4.3 Deep fluid pathways distribution analysis

Synthetic Images

Validation of the current method was performed on the two synthetic images in Fig. 5.1(a, b). Unlike volumetric relief maps in Fig. 5.1(c, d), geodesic relief maps serve to highlight the topological structure of objects to distinguish clearly between them as shown in Fig. 5.12. Thus, a geodesic relief map provide us a “topological signature” of objects.

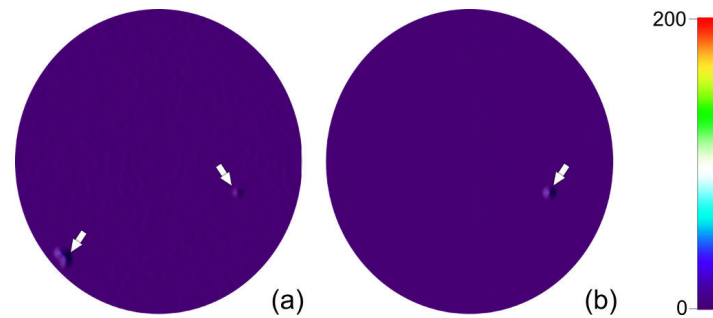


Figure 5.12 – Comparison of the two colored geodesic relief maps of synthetic images from Fig. 5.1 with two connected branches (a) and a disconnected branch (b).

Geodesic relief map generation

Geodesic relief maps were generated using the same clinical dataset, settings and materials than for volumetric relief maps in Chapter 4. Maps were initialized with a width of 203 pixels, and the radius of the hemisphere was set to 100 mm. The overall time of image acquisition including the pre-processing and the map generation is less than 5 min for each patient: 3 min for the image acquisition, 50 seconds for the pre-processing and 20 seconds or less for the map generation.

Figure 5.13 shows a geodesic relief map example for a healthy volunteer using a 26-connectivity. For almost every healthy adults, deep fluid pathways, *i.e.*, seeds that have been most propagated through the cerebrospinal fluid volume, are distributed over the entire map, particularly along the longitudinal cerebral fissure and most larger sulci.

Figure 5.14 shows geodesic relief map examples for one patient before (a) and after (b) a surgery. Before surgery, as observed from Fig. 5.14(a), notice regions depleted of deep fluid pathways and the strong asymmetry. Those depleted regions are related to the occipital lobe and posterior parts of both the temporal lobes and the parietal ones as noticed for volumetric relief maps, but they may also be related to the frontal lobe. After surgery, as observed from Fig. 5.14(b), the number of deep fluid pathways has increased and such pathways recovered a more balanced distribution, mainly along cerebral sulci. Furthermore, the deep fluid pathways localization can be superimposed to the corresponding volumetric relief map, to indicate regions, mostly sulci, that have largest fluid pathways as shown in Fig. 5.15(a, b).

Moment-based analysis of geodesic relief maps

Similarly to volumetric relief maps, we extract geometric characteristics from each geodesic relief map by using a moment-based approach as explained in Section 4.4.2. The distribution of centers of mass for healthy adults and pathological

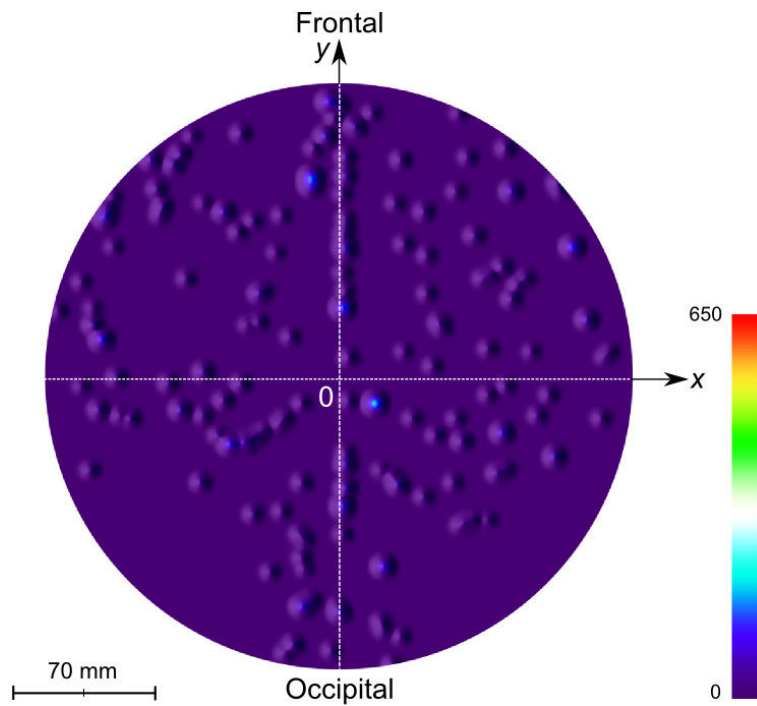


Figure 5.13 – An example of colored geodesic relief map for a healthy adult. The longitudinal cerebral fissure separates the map vertically and shows several deep fluid pathways.

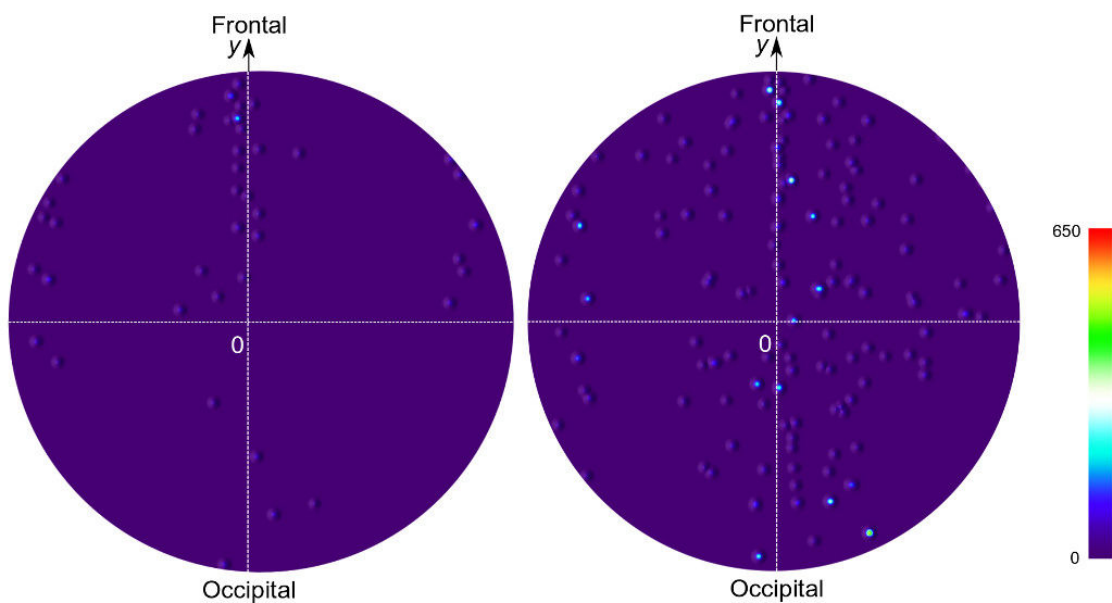


Figure 5.14 – Colored geodesic relief maps for a non-communicating hydrocephalus patient before (a) and after (b) surgery. Note that deep fluid pathways have recovered a more balanced distribution after surgery.

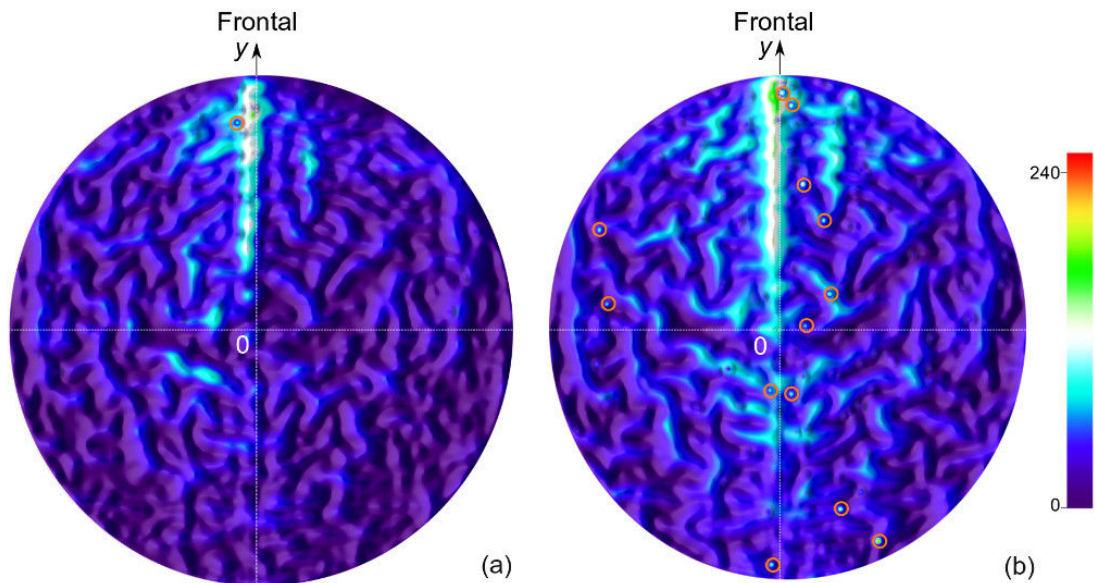


Figure 5.15 – Colored volumetric relief maps, with superimposed deep fluid pathways from geodesic maps, for a non-communicating hydrocephalus patient before (a) and after (b) surgery. Larger deep fluid pathways are surrounded by red circles. Note that deep fluid pathways have recovered a more balanced distribution after surgery.

cases is similar to that in Chapter 4, which seems to confirm previous classification results (see Fig. 5.16). Results are summarized in Table 5.1.

Table 5.1 – Means with standard deviations of the low order moment-based features calculated from geodesic relief maps for healthy adults and pathological cases, respectively.

Order	Feature	Class	Value
0	volume (cm ³)	healthy	237 ± 51
		pathological	200 ± 83
1	center of mass (mm)	healthy	$C_x = 2.3 \pm 2.45$; $C_y = -0.69 \pm 8.33$
		pathological	$C_x = 1.95 \pm 2.3$; $C_y = 16.64 \pm 8.47$
2	orientation (degrees)	healthy	$\theta = 88 \pm 48$
		pathological	$\theta = 86 \pm 51$
3	skewness	healthy	$ Sk_x = 0.03 \pm 0.03$; $Sk_y = -0.03 \pm 0.15$
		pathological	$ Sk_x = 0.02 \pm 0.13$; $Sk_y = -0.5 \pm 0.14$

5.5 CONCLUSION

The work presented in this chapter, still at a preliminary stage, suggested using geodesic propagation from one or more seeds within the cerebrospinal fluid in the superior cortical subarachnoid space. The result of propagation from one or several seeds can be combined with volumetric relief maps to track fluid pathways. By con-

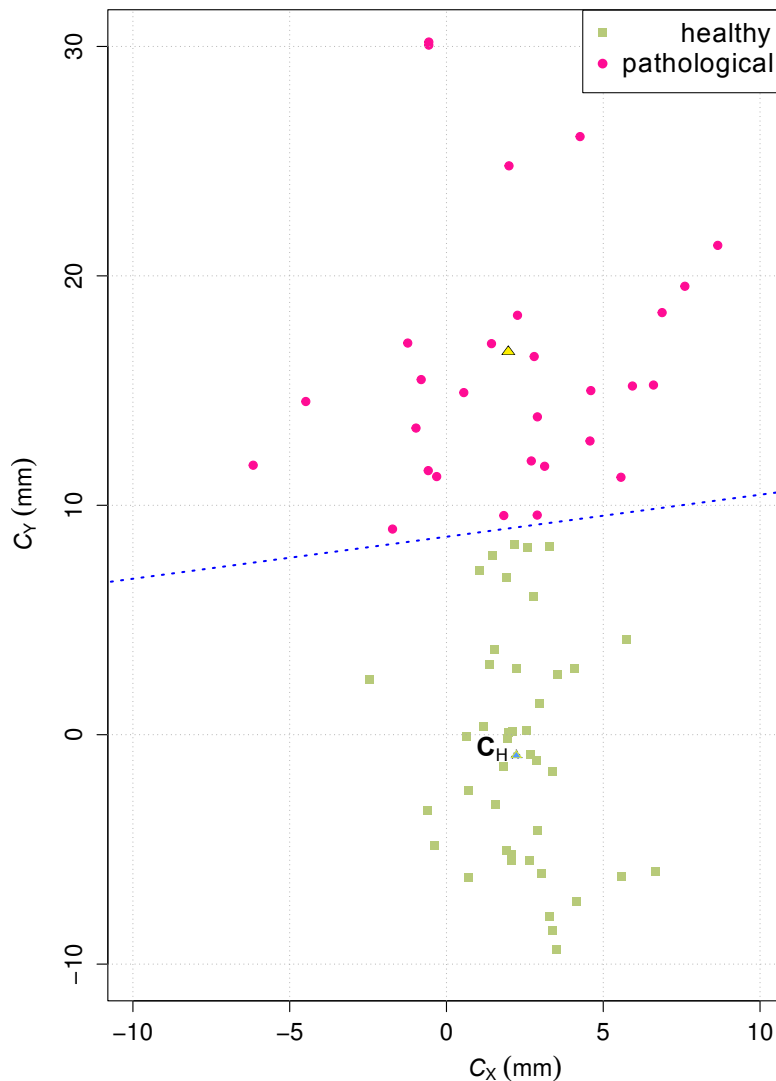


Figure 5.16 – Distribution of the centers of mass for the clinical dataset with its descriptive discriminant analysis. The dotted line ($C_Y = 0.1245C_X + 8.04$), resulting from the discriminant analysis, indicates the limit values from which the centers of mass can be distinguished between healthy adults and hydrocephalus patients. Healthy adults have an average center of mass C_H close to the relief map center (bottom blue triangle). In contrast, hydrocephalus patients have their deep fluid pathways distribution depleted in most regions, with larger deviations around the longitudinal cerebral fissure than healthy adults (the average is illustrated by the top yellow triangle).

sidering homogeneously distributed seeds on a targeted relief map, we obtained a complementary two-dimensional image representation to volumetric relief maps, called geodesic relief maps. Similarly to volumetric relief maps, geodesic maps can be used to visualize, characterize and analyze the cerebrospinal fluid distribution within the cortical subarachnoid space. In addition, they show the distribution of deep fluid pathways which provide information to distinguish between healthy adults and pathological cases.

In complementary works about the cerebrospinal fluid network analysis within the superior cortical subarachnoid space, it may be interesting to consider not only fluid sources, but also sinks. So it could be helpful to formalize the problem as a maximum flow problem [25, chap. 26], to better understand and characterize not only fluid structure, but also volumetric flow rate and flow velocity information.

CONCLUSION AND PERSPECTIVES

6

6.1 CONTRIBUTIONS

This work is devoted to the development of computational methods for medical image analysis and diagnosis which concern the study of cerebrospinal fluid volumes. From a medical point of view, our results provided physiological characteristics about the fluid volumes equilibrium with respect to a steady state intracranial pressure.

The first contribution of this thesis is the analysis of cerebrospinal fluid volumes from a recent “tissue specific” whole body magnetic resonance imaging sequence. We proposed an automatic segmentation method of the entire cerebrospinal fluid from these particular whole body images, by making use of a topological model of the fluid shape as well as image properties. The total volume was separated into ventricular and subarachnoid spaces by considering morphological characteristics of the fluid in different regions. These segmentation and separation methods helped to process a large number of images, and allowed to extract a functional index to describe the intracranial pressure steady state. We showed that the ratio of the total subarachnoid space volume to the ventricular space volume is a proportionality constant for healthy adults, in order to maintain a stable intracranial pressure, whereas it decreases significantly for pathological cases suffering of hydrocephalus.

In the second part of this work, we investigated on the cortical subarachnoid space from a structural point of view. We first proposed the fast two-dimensional visualization method that generates volumetric relief maps from the three-dimensional pre-segmented images of the superior cortical subarachnoid space. Volumetric relief maps are used to visualize and characterize the fluid volume distribution within the subarachnoid space as previously mentioned. They were efficiently used for the clinical diagnosis of hydrocephalus and monitoring of patients before and after surgery. Despite its effectiveness, such method disregards topological characteristic of the fluid, particularly within the cerebral sulci network. In a second step, we suggest an additional method that takes into account the fluid

network topology within the superior cortical subarachnoid space. The method can be combined with volumetric relief maps, in order to visualize fluid pathways from one or more given seeds within the cerebrospinal fluid volume. Furthermore, it can be also used to produce geodesic relief maps from homogeneously distributed seeds located on the hemispherical periphery closed to the cranium. Similarly to volumetric relief maps, geodesic relief maps visualize, characterize and analyze the cerebrospinal fluid distribution within the cortical subarachnoid space as a two-dimensional image. Note that they also indicate the distribution of deep fluid pathways from a given seed set.

6.2 LIMITATIONS

The volumes assessment technique presented in Chapter 3 is closely related to the 3D-SPACE image characteristics as well as the correct extraction of structures such as the cerebral aqueduct and eyeballs. One limitation is that separation of the ventricular and subarachnoid spaces may fail in some pathological cases where the cerebral aqueduct is completely hidden in the image because of a severe stenosis. Nonetheless, we have experienced good results of the segmentation and separation steps in most moderate aqueductal stenoses cases as the topological constraint operates on the entire image and allows to find a consistent path between the third and fourth ventricles.

Although volumetric and geodesic relief maps do not depend on the input image, both necessitate a robust positioning of the hemisphere in order to characterize and compare them. Such positioning also requires an accurate localization of the cerebral aqueduct that may have failed in some previous steps. However, this can be corrected manually by an expert.

6.3 PERSPECTIVES

From a medical viewpoint, the cerebrospinal fluid volumes quantification method presented in Chapter 3 should help to refine ongoing results as the whole body cerebrospinal fluid image dataset is in expansion. Moreover, the proposed method should facilitate large studies of cerebrospinal fluid volume variations, depending on gender and age, for healthy people and pathological cases.

Volumetric and geodesic relief maps are useful visualization tools and effortless

to apply in various scenes. For example, it may be interesting to observe the volume distribution differences depending on not only gender and age, but also left- or right-handedness, before making hypotheses for more important assessments. Furthermore, both relief maps would be suitable to visualize and characterize miscellaneous complex three-dimensional structures, in the medical field and other fields such as geological and mechanical ones, from various imaging modalities.

Concerning the structural analysis of the cortical subarachnoid space, further studies are expected; for example, its automatic decomposition into cerebral sulci. It may be also interesting to analyze the volumetric flow rate from the volume and network information, by formulating the problem as a maximum flow problem [25, Chapter 26].

Finally, besides the analysis and diagnostic issues of the work presented in this thesis, we would like to show that our results primarily aim to provide guidance for the implementation of a future biomechanical model of the cerebrospinal fluid. Several studies have been achieved to model the cerebrospinal fluid, but most are limited to the modeling of its pulsatile flow within the third ventricle and cerebral aqueduct [44, 59, 75, 104], to the entire ventricular space [21, 92, 93], or to some limited regions of the subarachnoid space [59, 92, 93, 104]. Some authors have suggested simple but time-consuming intracranial models [37, 161, 183]. Therefore, the challenge to achieve a model of the entire cerebrospinal fluid that is not time-consuming, should better allow to understand the interactions between spaces. Such a model could also be used with static whole body images of the cerebrospinal fluid presented in this work, to help to perform intracranial pressure estimations in routine clinical practice [181].

INDEX

- Cerebral sulci, 58, 62–65, 68
 - Central cerebral, 61, 63, 64
 - Intraparietal, 63, 64
 - Lateral cerebral fissure, 61, 62
 - Longitudinal cerebral fissure, 61–63, 68–70, 83
 - Postcentral, 63
 - Precentral, 63, 64
 - Superior frontal, 63, 64
- Cerebrospinal fluid, 5, 7, 11–18, 20, 29
 - Arachnoid granulations, 12, 16, 18–20, 31, 81, 82
 - Bulk flow, 12, 18, 19, 31
 - Choroid plexus, 5, 11, 12, 18, 31
 - Cisterns, 14, 19, 20, 30
 - Interpeduncular, 16, 19, 37
 - Lumbar, 19
 - Pontocerebellar, 14, 15, 19
 - Posterior cerebellomedullary, 14, 15, 19
 - Quadrigeminal, 16, 19
 - Lateral apertures, 14, 30
 - Median aperture, 12, 14, 15, 19, 31
 - Physiology, 6, 12, 16–19
 - Pulsatile flow, 13, 18
 - Subarachnoid space, 6, 11–14, 16, 17, 19, 31
 - Cortical, 29, 31, 34–36, 41, 54, 55, 57–60, 62, 63, 65
 - Spinal, 12, 17, 18, 29, 33, 35, 36, 41, 44, 48
 - Ventricular system, 11–15, 17, 19, 29–31, 34, 35, 37, 41
 - Cerebral aqueduct, 14, 15, 19, 35–40, 55, 58, 61
 - Fourth ventricle, 12–15, 37
 - Infundibular recess, 13, 15, 37
 - Interventricular foramen, 13, 15
 - Lateral ventricles, 12, 13
 - Third ventricle, 13, 14, 37
 - Volume, 5–7, 17, 18, 29, 44–47
 - Assessment, 6, 17, 29, 44, 45, 48
 - Ratio, 29, 46, 48
- CH, *see* Communicating hydrocephalus
- Communicating hydrocephalus, *see* Hydrocephalus
- Discriminant analysis, 46, 49, 69, 70, 72, 73, 94
- Distance map
 - Euclidean, 32
 - Geodesic, 83
- Gauss digitization, 58
- Geometric moments, *see* Moments
- Hessian filter, 37–39
- Hydrocephalus, 5, 11, 18, 29
 - Classification, 18, 48, 49

- Communicating hydrocephalus, 20, 29
- Diagnosis, 6, 29, 48, 49, 69–73, 94
- Monitoring, 72–74
- Non-communicating hydrocephalus, 20
- Treatment, 20
- Index
 - Evan’s index, 6
 - Volume ratio, *see* Cerebrospinal fluid
- Intracranial hypertension, *see* Intracranial pressure
- Intracranial hypotension, *see* Intracranial pressure
- Intracranial pressure, 5, 6, 12, 20, 46
 - Measurement, 6, 12, 29
 - Monro-Kellie hypothesis, 5
- Linear regression, 44, 46, 47
- Magnetic resonance imaging, 6, 13, 20–23, 29
 - 3D-SPACE sequence, 23–25, 30
- Map projection, 53, 54
 - Lambert azimuthal equal-area, 56, 57, 88, 90
- Mathematical morphology
 - h -dome transform, 40
 - Geodesic reconstruction, 38, 40
- Moments, 65, 66
 - Center of mass, 65–70, 72, 73, 83, 87, 91, 94
 - Orientation, 65, 66, 68, 69, 83, 87, 88
 - Skewness, 66–69, 71, 72, 74, 87
- MRI, *see* Magnetic resonance imaging
- NCH, *see* Non-communicating hydrocephalus
- Non-communicating hydrocephalus, *see* Hydrocephalus
- Normal pressure hydrocephalus, *see* Communicating hydrocephalus
- NPH, *see* Communicating hydrocephalus
- Ray tracing, 56, 57
 - Discrete, 89, 90
- Relief map
 - Geodesic, 80, 87–93
 - Volumetric, 53, 54, 56–58, 60–63, 65–69, 79, 83–86
- Thresholding
 - Histogram-based thresholding, 32
 - Moment-preserving algorithm, 32, 34
 - Triangle algorithm, 32, 34
- Topology
 - Homotopic tickening, 31, 33–35
 - Simple point, 33
 - Topological Model, 29–32

BIBLIOGRAPHY

- [1] Michael J. Albeck, Svend E. Børgesen, Flemming Gjerris, Jes F. Schmidt, and Per Soelberg Sørensen. Intracranial pressure and cerebrospinal fluid outflow conductance in healthy subjects. *Journal of Neurosurgery*, 74(4):597–600, April 1991. (Cited page 6.)
- [2] Katherine P. Andriole, Jeremy M. Wolfe, Ramin Khorasani, S. Ted Treves, David J. Getty, Francine L. Jacobson, Michael L. Steigner, John J. Pan, Arkadiusz Sitek, and Steven E. Seltzer. Optimizing analysis, visualization, and navigation of large image data sets: One 5000-section CT scan can ruin your whole day. *Radiology*, 259(2):346–362, May 2011. (Cited pages 6 and 53.)
- [3] Richard Arbour. Intracranial hypertension: Monitoring and nursing assessment. *Critical Care Nurse*, 24(5):19–34, October 2004. (Cited page 5.)
- [4] Alfred Aschoff, Paul Kremer, Bahram Hashemi, and Stefan Kunze. The scientific history of hydrocephalus and its treatment. *Neurosurgery Review*, 22(2–3):67–93, October 1999. (Cited pages 11 and 20.)
- [5] Olivier Balédent, Marie Cécile Henry-Feugeas, and Ilana Idy-Peretti. Cerebrospinal fluid dynamics and relation with blood flow: a magnetic resonance study with semiautomated cerebrospinal fluid segmentation. *Investigative Radiology*, 36(7):368–377, July 2001. (Cited page 18.)
- [6] Pierre-Louis Bazin and Dzung L. Pham. Topology correction of segmented medical images using a fast marching algorithm. *Computer Methods and Programs in Biomedicine*, 88(2):182–190, November 2007. (Cited page 30.)
- [7] Pierre-Louis Bazin and Dzung L. Pham. Topology-preserving tissue classification of magnetic resonance brain images. *IEEE Transactions on Medical Imaging*, 26(4):487–496, April 2007. (Cited page 30.)
- [8] Fethallah Benmansour and Laurent D. Cohen. Fast object segmentation by growing minimal paths from a single point on 2D or 3D images. *Journal of Mathematical Imaging and Vision*, 33(2):209–221, February 2009. (Cited page 79.)

- [9] Edgar A. Bering, Jr. Circulation of the cerebrospinal fluid. demonstration of the choroid plexus as the generator of the force for flow of fluid and ventricular enlargement. *Journal of Neurosurgery*, 19(5):405–413, May 1962. (Cited page 18.)
- [10] Gilles Bertrand and Grégoire Malandain. A new characterization of 3-dimensional simple points. *Pattern Recognition Letters*, 15(2):169–175, February 1994. (Cited page 33.)
- [11] Duane D. Blatter, Erin D. Bigler, Shawn D. Gale, Sterling C. Johnson, Carol V. Anderson, Bruce M. Burnett, Natalie Parker, Shanna Kurth, and Susan D. Horn. Quantitative volumetric analysis of brain MR: Normative database spanning 5 decades of life. *American Journal of Neuroradiology*, 16:241–251, February 1995. (Cited page 29.)
- [12] Kaj Blennow and Eugeen Vanmechelen. CSF markers for incipient Alzheimer’s disease. *The Lancet Neurology*, 2(10):605–613, October 2003. (Cited page 17.)
- [13] Felix Bloch. Nuclear induction. *Physical Review*, 70(7–8):460–474, October 1946. (Cited page 13.)
- [14] R. Bozanovic-Sosic, R. Mollanji, and M. G. Johnston. Spinal and cranial contributions to total cerebrospinal fluid transport. *American Journal of Physiology – Regulatory, Integrative and Comparative Physiology*, 281(3):R909–R916, September 2001. (Cited page 18.)
- [15] James H. Breasted. *The Edwin Smith Surgical Papyrus: published in facsimile and hieroglyphic transliteration with translation and commentary in two volumes*. The Oriental Institute of the University of Chicago, Chicago, 1991. ISBN 978-0-9189-8673-3. (Cited page 11.)
- [16] Lev Moiseevič Bugaevskij and John Parr Snyder. *Map projections: A reference manual*. Taylor & Francis, London, 1995. ISBN 978-0-7484-0304-2. (Cited pages 54, 56, and 88.)
- [17] George Burrows. *On disorders of the cerebral circulation and on the connection between affections of the brain and diseases of the heart*. Lea & Blanchard, Philadelphia, 1848. (Cited page 5.)

- [18] Jerrold T. Bushberg, J. Anthony Seibert, Edwin M. Leidholdt Jr, and John M. Boone. *The essential physics of medical imaging*. Lippincott Williams & Wilkins, Philadelphia, PA, 2nd edition, 2002. ISBN 978-0-7817-8057-5. (Cited page 21.)
- [19] Reed F. Busse, Anja C.S. Brau, Anthony Vu, Charles R. Michelich, Ersin Bayram, Richard Kijowski, Scott B. Reeder, and Howard A. Rowley. Effects of refocusing flip angle modulation and view ordering in 3D fast spin echo. *Magnetic Resonance in Medicine*, 60(3):640–649, September 2008. (Cited page 22.)
- [20] M. Ciołkowski, M. Sharifi, S. Tarka, and B. Ciszek. Median aperture of the fourth ventricle revisited. *Folia Morphologica (Poland)*, 70(2):84–90, May 2011. (Cited page 14.)
- [21] Olivier Clatz, Stéphane Litrico, Hervé Delingette, Philippe Paquis, and Nicholas Ayache. Dynamic model of communicating hydrocephalus for surgery simulation. *IEEE Transactions on Biomedical Engineering*, 54(4):755–758, April 2007. (Cited page 99.)
- [22] Laurent D. Cohen. On active contours models and balloons. *Computer Vision, Graphics, and Image Processing: Image Understanding*, 53(2):211–218, March 1991. (Cited page 38.)
- [23] Daniel Cohen-Or and Arie Kaufman. 3D line voxelization and connectivity control. *IEEE Computer Graphics and Applications*, 17(6):80–87, November 1997. (Cited page 89.)
- [24] B. Condon, D. Wyper, R. Grant, J. Patterson, D. Hadley, G. Teasdale, and J. Rowan. Use of magnetic resonance imaging to measure intracranial cerebrospinal fluid volume. *The Lancet*, 327(8494):1355–1357, June 1986. (Cited pages 29, 44, and 45.)
- [25] Thomas H. Cormen, Charles E. Leiserson, Ronald L. Rivest, and Clifford Stein. *Introduction to algorithms*. MIT Press, Cambridge, MA, 3rd edition, 2009. ISBN 978-0-2620-3384-8. (Cited pages 80, 81, 95, and 99.)
- [26] Robert Corns and Andrew Martin. Hydrocephalus. *Surgery*, 30(3):142–148, March 2012. (Cited pages 17, 18, and 20.)
- [27] Pierrick Coupé, Pierre Yger, Sylvain Prima, Pierre Hellier, Charles Kervrann, and Christian Barillot. An optimized blockwise nonlocal means denoising fil-

- ter for 3-D magnetic resonance images. *IEEE Transactions on Medical Imaging*, 27(4):425–441, April 2008. (Cited page 30.)
- [28] Enrico Crivellato and Domenico Ribatti. Soul, mind, brain: Greek philosophy and the birth of neuroscience. *Brain Research Bulletin*, 71(4):327–336, January 2007. (Cited page 11.)
- [29] Harvey Cushing. *Studies in intracranial physiology and surgery: The third circulation, the hypophysics, the gliomas*. Oxford University Press, London, 1926. (Cited page 5.)
- [30] Marek Czosnyka and John D. Pickard. Monitoring and interpretation of intracranial pressure. *Journal of Neurology, Neurosurgery & Psychiatry*, 75(6):813–821, June 2004. (Cited page 6.)
- [31] R. Damadian, L. Minkoff, M. Goldsmith, M. Stanford, and J. Koutcher. Field focusing nuclear magnetic resonance (FONAR): visualization of a tumor in a live animal. *Science*, 194(4272):1430–1432, December 1976. (Cited page 21.)
- [32] Walter E. Dandy. Ventriculography following the injection of air into the cerebral ventricles. *Annals of Surgery*, 68(1):5–11, July 1918. (Cited page 13.)
- [33] Walter E. Dandy and Kenneth D. Blackfan. An experimental and clinical study of internal hydrocephalus. *Journal of the American Medical Association*, 61(25):2216–2217, December 1913. (Cited pages 12 and 18.)
- [34] Thomas Deschamps and Laurent D. Cohen. Fast extraction of minimal paths in 3D images and applications to virtual endoscopy. *Medical Image Analysis*, 5(4):281–299, December 2001. (Cited page 79.)
- [35] Kunio Doi. Computer-aided diagnosis in medical imaging: Historical review, current status and future potential. *Computerized Medical Imaging and Graphics*, 31(4):198–211, June 2007. (Cited page 6.)
- [36] Petr Dokládál, Isabelle Bloch, Michel Couprie, Daniel Ruijters, Raquel Urtasun, and Line Garnero. Topologically controlled segmentation of 3D magnetic resonance images of the head by using morphological operators. *Pattern Recognition*, 36(10):2463–2478, October 2003. (Cited page 30.)
- [37] Tonmoy Dutta-Roy, Adam Wittek, and Karol Miller. Biomechanical modelling of normal pressure hydrocephalus. *Journal of Biomechanics*, 41(10):2263–2271, July 2008. (Cited page 99.)

- [38] M. Edsbagge, G. Starck, H. Zetterberg, D. Ziegelitz, and C. Wikkelso. Spinal cerebrospinal fluid volume in healthy elderly individuals. *Clinical Anatomy*, 24(6):733–740, September 2011. (Cited pages 29, 44, and 45.)
- [39] L. J. Erasmus, D. Hurter, M. Naudé, H. G. Kritzinger, and S. Acho. A short overview of MRI artefacts. *South African Journal of Radiology*, 8(2):13–17, August 2004. (Cited page 29.)
- [40] Stephanie S. Erlich and Michael L. J. Apuzzo. The pineal gland: anatomy, physiology, and clinical significance. *Journal of Neurosurgery*, 63(3):321–341, September 1985. (Cited page 55.)
- [41] Williams A. Evans. An encephalographic ratio for estimating ventricular enlargement and cerebral atrophy. *Archives of Neurology and Psychiatry*, 47(6):931–937, June 1942. (Cited page 6.)
- [42] J.-J. Faivre. Recherches sur la structure du coronarium et des plexus choroïdes chez l’homme et chez les animaux. *Compte-rendu de l’Académie des Sciences*, 39:424–427, 1854. (Cited page 12.)
- [43] Alexandre X. Falcão, Jorge Stolfi, and Roberto de Alencar Lotufo. The image foresting transform: Theory, algorithms, and applications. *IEEE Transactions on Pattern Analysis and Machine Intelligence*, 26(1):19–29, January 2004. (Cited page 81.)
- [44] Loïc Fin and Reinhard Grebe. Three dimensional modeling of the cerebrospinal fluid dynamics and brain interactions in the aqueduct of Sylvius. *Computer Methods in Biomechanics and Biomedical Engineering*, 6(3):163–170, June 2003. (Cited page 99.)
- [45] Guillaume Flandin, Ferath Kherif, Xavier Pennec, Grégoire Malandain, Nicholas Ayache, and Jean-Baptiste Poline. Improved detection sensitivity in functional MRI data using a brain parcelling technique. In *Proceedings of the 5th International Conference on Medical Image Computing and Computer-Assisted Intervention (MICCAI 2002), Tokyo, Japan, September 25–28, 2002*, volume 2488 of *Lecture Notes in Computer Science*, pages 467–474, Heidelberg, 2002. Springer-Verlag. (Cited page 79.)
- [46] Jan Flusser, Tomáš Suk, and Barbara Zitová. *Moments and moment invariants in pattern recognition*. John Wiley & Sons, Ltd, Chichester, West Sussex, 2009. ISBN 978-0-4706-9987-4. (Cited page 65.)

- [47] James D. Foley, Andries van Dam, Steven K. Feiner, and John F. Hughes. *Computer graphics: Principles and practice in C*. Addison-Wesley, Reading, MA, 2nd edition, 1995. ISBN 978-0-2018-4840-3. (Cited pages 54 and 56.)
- [48] Alejandro F. Frangi, Wiro J. Niessen, Koen L. Vincken, and Max A. Viergever. Multiscale vessel enhancement filtering. In W. M. Wells, A. Colchester, and S. L. Delp, editors, *Proceedings of the 1st International Conference on Medical Image Computing and Computer-Assisted Intervention (MICCAI '98)*, Cambridge, MA, USA, October 11–13, 1998, volume 1496 of *Lecture Notes in Computer Science*, pages 130–137, Heidelberg, 1998. Springer-Verlag. (Cited pages 37, 38, and 39.)
- [49] David B. Fuller. *Osteopathy and Swedenborg: The influence of Emanuel Swedenborg on the genesis and development of osteopathy, specifically on Andrew Taylor Still and William Garner Sutherland*. Swedenborg Scientific Association Press, Bryn Athyn, PA, 2012. ISBN 978-0-9105-5782-5. (Cited page 11.)
- [50] Thomas A. Gallagher, Alexander J. Nemeth, and Lotfi Hacein-Bey. An introduction to the Fourier transform: Relationship to MRI. *American Journal of Roentgenology*, 190(5):1396–1405, May 2008. (Cited page 21.)
- [51] Gary L. Gallia, Daniele Rigamonti, and Michael A. William. The diagnosis and treatment of idiopathic normal pressure hydrocephalus. *Natural Clinical Practice – Neurology*, 2(7):375–381, July 2006. (Cited page 6.)
- [52] Tal Geva. Magnetic resonance imaging: Historical perspective. *Journal of Cardiovascular Magnetic Resonance*, 8(4):573–580, August 2006. (Cited page 20.)
- [53] Henri Gray. *Anatomy of the Human Body*. Lea & Febiger, Philadelphia, 1818. (Cited pages 14, 15, and 16.)
- [54] Charles G. Gross. Emanuel Swedenborg: A neuroscientist before his time. *The Neuroscientist*, 3(2):142–147, March 1997. (Cited page 11.)
- [55] Charles G. Gross. *Brain, vision, memory: Tales in the history of neurosciences*. MIT Press, Cambridge, 1998. ISBN 978-0-2625-7135-7. (Cited page 11.)
- [56] Charles G. Gross. Galen and the squealing pig. *The Neuroscientist*, 4(3):216–221, May 1998. (Cited page 11.)
- [57] Deborah M. Grzybowski, Edward E. Herderick, Kapil G. Kapoor, David W. Holman, and Steven E. Katz. Human arachnoid granulations Part I: a tech-

- nique for quantifying area and distribution on the superior surface of the cerebral cortex. *Cerebrospinal Fluid Research*, 4:6, July 2007. (Cited page 82.)
- [58] Hákon Gudbjartsson and Samuel Patz. The Rician distribution of noisy MRI data. *Magnetic Resonance in Medicine*, 34(6):910–914, December 1995. (Cited page 30.)
- [59] Sumeet Gupta, Michaela Soellinger, Peter Boesiger, Dimos Poulikakos, and Vartan Kurtcuoglu. Three-dimensional computational modeling of subject-specific cerebrospinal fluid flow in the subarachnoid space. *Journal of Biomechanical Engineering*, 131(2), February 2009. (Cited page 99.)
- [60] Sumeet Gupta, Michaela Soellinger, Deborah M. Grzybowski, Peter Boesiger, John Biddiscombe, Dimos Poulikakos, and Vartan Kurtcuoglu. Cerebrospinal fluid dynamics in the human cranial subarachnoid space: an overlooked mediator of cerebral disease. I. Computational model. *Journal of the Royal Society Interface*, 7(49):1195–1204, August 2010. (Cited page 7.)
- [61] Erwin L. Hahn. Spin echoes. *Physical Review*, 80(4):580–594, November 1950. (Cited pages 13 and 22.)
- [62] Steven I. Hajdu. A note from history: Discovery of the cerebrospinal fluid. *Annals of Clinical & Laboratory Science*, 33(3):334–336, July 2003. (Cited page 11.)
- [63] S. Hakim and R.D. Adams. The special clinical problem of symptomatic hydrocephalus with normal cerebrospinal fluid pressure. observations on cerebrospinal fluid hydrodynamics. *Journal of the Neurological Sciences*, 2(4):307–327, July–August 1965. (Cited page 20.)
- [64] Xiao Han, Chenyang Xu, and J.L. Prince. Topology preserving level set method for geometric deformable models. *IEEE Transactions on Pattern Analysis and Machine Intelligence*, 25(6):755–768, June 2003. (Cited page 30.)
- [65] Trevor Hastie, Robert Tibshirani, and Jerome Friedman. *The elements of statistical learning: Data mining, inference, and prediction*. Springer Series in Statistics. Springer, New York, 5th edition, 2009. ISBN 978-0-3878-4857-0. (Cited pages 46 and 69.)
- [66] Martin C. Hirsch. *Dictionary of human neuroanatomy*. Springer-Verlag, Berlin, 2000. ISBN 978-3-5406-6523-6. (Cited page 16.)

- [67] Jérôme Hodel. *Nouvelles approches techniques pour l'imagerie du liquide cérebrospinal et applications cliniques aux patients présentant une hydrocéphalie*. Thèse de doctorat, Université Paris-Est Créteil, 2012. (Cited pages 7 and 23.)
- [68] Jérôme Hodel, Alain Le Bret, Eric Petit, Xavier Leclerc, Marc Zins, Alexandre Vignaud, Philippe Decq, and Alain Rahmouni. Imaging of the entire cerebrospinal fluid volume with a multistation 3D SPACE MR sequence: feasibility study in patients with hydrocephalus. *European Radiology*, 23(6):1450–1458, June 2013. (Cited pages 7 and 23.)
- [69] Jérôme Hodel, Jonathan Silvera, Olivier Bekaert, Alain Rahmouni, Sylvie Bastuji-Garin, Alexandre Vignaud, Eric Petit, Bruno Durning, and Philippe Decq. Intracranial cerebrospinal fluid spaces imaging using a pulse-triggered three-dimensional turbo spin echo MR sequence with variable flip-angle distribution. *European Radiology*, 21(2):402–410, February 2011. (Cited pages 7, 23, 29, 42, 43, 44, 45, and 55.)
- [70] Q. H. Hogan, R. Prost, A. Kulier, M. L. Taylor, S. Liu, and L. Mark. Magnetic resonance imaging of cerebrospinal fluid volume and the influence of body habitus and abdominal pressure. *Anesthesiology*, 84(6):1341–1349, June 1996. (Cited page 29.)
- [71] Igor Holländer. Cerebral cartography – a method for visualizing cortical structures. *Computerized Medical Imaging and Graphics*, 19(5):397–415, September–October 1995. (Cited pages 53 and 54.)
- [72] David W. Holman, Vartan Kurtcuoglu, and Deborah M. Grzybowski. Cerebrospinal fluid dynamics in the human cranial subarachnoid space: an overlooked mediator of cerebral disease. II. In vitro arachnoid outflow model. *Journal of the Royal Society Interface*, 7(49):1205–1218, August 2010. (Cited page 7.)
- [73] Ming-Kuei Hu. Visual pattern recognition by moment invariants. *IRE Transactions on Information Theory*, 8:179–187, February 1962. (Cited page 65.)
- [74] Monica K. Hurdal, Ken Stephenson, Phil Bowers, De Witt Sumners, and David A. Rottenberg. Coordinate systems for conformal cerebellar flat maps. *NeuroImage*, 11(5):S467, May 2000. (Cited pages 53 and 54.)
- [75] E. E. Jacobson, D. F. Fletcher, M. K. Morgan, and I. H. Johnston. Computer modelling of the cerebrospinal fluid flow dynamics of aqueduct stenosis.

- Medical and Biological Engineering and Computing*, 37(1):59–63, 1999. (Cited page 99.)
- [76] Conrad E. Johanson, John A. Duncan III, Petra M. Klinge, Thomas Brinker, Edward G. Stopa, and Gerald D. Silverberg. Multiplicity of cerebrospinal fluid functions: New challenges in health and disease. *Cerebrospinal Fluid Research*, 5(10), May 2008. (Cited pages 17 and 18.)
- [77] Robert Jones and Oliver Lodge. The discovery of a bullet lost in the wrist by means of the Roentgen rays. *The Lancet*, 147(3782):476–477, February 1896. (Cited page 13.)
- [78] Werner Kähle. Atlas de poche d’anatomie : (3) système nerveux et organes des sens. Flammarion Médecine-Sciences, Paris, 4^e edition, 2007. ISBN 978-2-2571-4253-5. (Cited page 14.)
- [79] Kapil G. Kapoor, Steven E. Katz, Deborah M. Grzybowski, and Martin Lubow. Cerebrospinal fluid outflow: An evolving perspective. *Brain Research Bulletin*, 77(6):327–334, December 2008. (Cited page 18.)
- [80] Bruno Kastler, Daniel Vetter, Zoltán Patay, and Philippe Germain. *Comprendre l’IRM : Manuel d’auto-apprentissage*. Masson, Paris, 6^e edition, 2006. ISBN 2-294-05110-6. ISBN 978-2-2940-5110-4. (Cited page 21.)
- [81] George Kellie. An account of the appearances observed in the dissection of two of the three individuals presumed to have perished in the storm of the 3rd, and whose bodies were discovered in the vicinity of Leith on the morning of the 4th November 1821 with some reflections on the pathology of the brain. *The Transactions of the Medico-Chirurgical Society of Edinburgh*, 1:84–169, 1824. (Cited page 5.)
- [82] Julie T. Kerr, Felix W.K. Chu, and Stephen W. Bayles. Cerebrospinal fluid rhinorrhea: Diagnosis and management. *Otolaryngologic Clinics of North America*, 38(4):597–611, August 2005. (Cited page 5.)
- [83] Ernst A. H. Key and Magnus G. Retzius. *Studien in der Anatomie des Nervensystems und des Bindegewebe*. Samson & Wallin, Stockholm, 1876. (Cited page 12.)
- [84] A. Jon Kimerling, W. Scott Overton, and Denis White. Statistical comparison of map projection distortions within irregular areas. *Cartography and Geographic Information Systems*, 22(3):205–221, March 1995. (Cited page 56.)

- [85] Hajime Kitagaki, Etsuro Mori, Kazunari Ishii, Shigeru Yamaji, Nobutsugu Hirono, and Toru Imamura. CSF spaces in idiopathic normal pressure hydrocephalus: Morphology and volumetry. *American Journal of Neuroradiology*, 19(7):1277–1284, August 1998. (Cited page 29.)
- [86] Richard Klette and Azriel Rosenfeld. *Digital geometry: Geometric methods for digital picture analysis*. Morgan Kaufmann, San Francisco, 2004. ISBN 978-1-5586-0861-0. (Cited pages 32, 57, 58, and 62.)
- [87] Mark I. Kohn, Nitin K. Tanna, G. T. Herman, S. M. Resnick, P. D. Mozley, R. E. Gur, Abass Alavi, Robert A. Zimmerman, and R. C. Gur. Analysis of brain and cerebrospinal fluid volumes with MR imaging. Part I. methods, reliability, and validation. *Radiology*, 178(1):115–122, January 1991. (Cited page 29.)
- [88] Karl Krissian, Grégoire Malandain, and Nicholas Ayache. Model-based detection of tubular structures in 3D images. *Computer Vision and Image Understanding*, 80(2):130–171, November 2000. (Cited page 37.)
- [89] Frithjof Kruggel. MRI-based volumetry of head compartments: Normative values of healthy adults. *NeuroImage*, 30(1):1–11, March 2006. (Cited pages 17 and 29.)
- [90] Anil Kumar, Dieter Welti, and Richard R. Ernst. NMR Fourier zeugmatography. *Journal of Magnetic Resonance*, 18(1):69–83, April 1975. (Cited page 21.)
- [91] Vartan Kurtcuoglu. Pulsatile cerebrospinal fluid flow in the cranial subarachnoid space. *Neurology, Psychiatry and Brain Research*, 18(2):66–67, March 2012. (Cited pages 7 and 18.)
- [92] Vartan Kurtcuoglu, Dimos Poulikakos, and Yiannis Ventikos. Computational modeling of the mechanical behavior of the cerebrospinal fluid system. *Journal of Biomechanical Engineering*, 127(2):264–269, April 2005. (Cited page 99.)
- [93] Vartan Kurtcuoglu, Michaela Soellinger, Paul Summers, Kevin Boomsma, Dimos Poulikakos, Peter Boesiger, and Yiannis Ventikos. Computational investigation of subject-specific cerebrospinal fluid flow in the third ventricle and aqueduct of sylvius. *Journal of Biomechanics*, 40(6):1235–45, January 2007. (Cited page 99.)

- [94] Pierre Lafaye de Micheaux, Rémy Drouilhet, and Benoît Liquet. *Le logiciel R. Statistique et probabilités appliquées*. Springer-Verlag, Paris, 2011. (Cited pages 44 and 69.)
- [95] Paul C. Lauterbur. Image formation by induced local interactions: Examples employing nuclear magnetic resonance. *Nature*, 242:190–191, March 1973. (Cited page 20.)
- [96] Alain Lebet, Jérôme Hodel, Alain Rahmouni, Philippe Decq, and Eric Petit. Cerebrospinal fluid volume analysis for hydrocephalus diagnosis and clinical research. *Computerized Medical Imaging and Graphics*, 37(3):224–233, April 2013. (Cited pages 7, 27, and 45.)
- [97] Alain Lebet, Yukiko Kenmochi, Jérôme Hodel, Alain Rahmouni, Philippe Decq, and Eric Petit. Relief map of the upper cortical subarachnoid space. In *CARS 2013. Computer Assisted Radiology and Surgery. Proceedings of the 27th International Congress and Exhibition, Heidelberg, Germany, June 26–29, 2013*, volume 8(Suppl 1), pages S282–S284, Heidelberg, 2013. Springer. (Cited pages 7 and 51.)
- [98] Alain Lebet, Eric Petit, Bruno Durning, Jérôme Hodel, Alain Rahmouni, and Philippe Decq. Quantification of the cerebrospinal fluid from a new whole body MRI sequence. In Bram van Ginneken and Carol L. Novak, editors, *Proceedings of SPIE Medical Imaging 2012: Computer-Aided Diagnosis, San Diego, California, USA, February 04–09, 2012*, volume 8315, pages 83153H–83153H–7, 2012. (Cited pages 7 and 27.)
- [99] Louis Lemieux, Alexander Hammers, Toby Mackinnon, and Rebecca S.N. Liu. Automatic segmentation of the brain and intracranial cerebrospinal fluid in T₁-weighted volume MRI scans of the head, and its application to serial cerebral and intracranial volumetry. *Magnetic Resonance in Medicine*, 49(5): 872–884, May 2003. (Cited page 29.)
- [100] David Lesage, Elsa D. Angelini, Isabelle Bloch, and Gareth Funka-Lea. A review of 3D vessel lumen segmentation techniques: Models, features and extraction schemes. *Medical Image Analysis*, 13(6):819–845, December 2009. (Cited page 37.)
- [101] Shane A. Liddelow. Fluids and barriers of the CNS: A historical viewpoint. *Fluids and Barriers of the CNS*, 8:2, January 2011. (Cited pages 11 and 12.)

- [102] Andreas A. Linninger, Brian Sweetman, and Richard Penn. Normal and hydrocephalic brain dynamics: The role of reduced cerebrospinal fluid reabsorption in ventricular enlargement. *Annals of Biomedical Engineering*, 37(7): 1434–1447, July 2009. (Cited page 7.)
- [103] Andreas A. Linninger, Cristian Tsakiris, David C. Zhu, Michalis Xenos, Peter Roycewicz, Zachary Danziger, and Richard Penn. Pulsatile cerebrospinal fluid dynamics in the human brain. *IEEE Transactions on Bio-Medical Engineering*, 52(4):557–565, April 2005. (Cited page 18.)
- [104] Andreas A. Linninger, Michalis Xenos, Brian Sweetman, Sukruti Pongshe, Xiaodong Guo, and Richard Penn. A mathematical model of blood, cerebrospinal fluid and brain dynamics. *Journal of Mathematical Biology*, 59(6): 729–759, December 2009. ISSN 1432-1416. (Cited page 99.)
- [105] Cristian Lorenz, I.-C. Carlsen, Thorsen M. Buzug, Carola Fassnacht, and Jürgen Weese. Multi-scale line segmentation with automatic estimation of width, contrast and tangential direction in 2D and 3D medical images. In *Proceedings of the First Joint Conference on Computer Vision, Virtual Reality and Robotics in Medicine and Medical Robotics and Computer-Assisted Surgery (CVRMed–MRCAS’97), Grenoble, France, March 19–22, 1997*, volume 1205 of *Lecture Notes in Computer Science*, pages 233–242, Berlin, Heidelberg, 1997. Springer-Verlag. (Cited page 37.)
- [106] Arvid Lundervold, Torfinn Taxt, Lars Ersland, and Anne-Marie Fenstad. Volume distribution of cerebrospinal fluid using multispectral MR imaging. *Medical Image Analysis*, 4(2):123–136, June 2000. (Cited pages 29, 44, and 45.)
- [107] François Magendie. *Leçons sur les fonctions et les maladies du système nerveux*, volume 1. Ébrard, Paris, 1839. (Cited pages 12 and 17.)
- [108] Jean-François Mangin, Vincent Frouin, Isabelle Bloch, Jean Régis, and Jaime López-Krahe. From 3D magnetic resonance images to structural representations of the cortex topography using topology preserving deformations. *Journal of Mathematical Imaging and Vision*, 5(4):297–318, December 1995. (Cited page 30.)
- [109] Jean-François Mangin, Fabrice Poupon, Édouard Duchesnay, Denis Rivière, Arnaud Cachia, D. Louis Collins, Alan C. Evans, and Jean Régis. Brain morphometry using 3D moment invariants. *Medical Image Analysis*, 8(3):187–196, September 2004. (Cited page 65.)

- [110] Jean-François Mangin, Florence Tupin, Vincent Frouin, Isabelle Bloch, Rozenn Rougetet, Jean Régis, and Jaime López-Krahe. Deformable topological models for segmentation of 3D medical images. In Yves Bizais, Christian Barillot, and Robert Di Paola, editors, *14th International Conference on Information Processing in Medical Imaging (IPMI'95), Ile de Berder, France, June 26–30, 1995*, volume 3 of *Computational Imaging and Vision*, pages 153–164, Dordrecht, The Netherlands, 1995. Kluwer Academic Publishers. ISBN 978-0-7923-3593-1. (Cited page 30.)
- [111] Rashindra Manniesing, Max A. Viergever, and Wiro J. Niessen. Vessel enhancing diffusion: A scale space representation of vessel structures. *Medical Image Analysis*, 10(6):815–825, December 2006. (Cited page 37.)
- [112] Peter Mansfield and Peter K. Grannell. NMR 'diffraction' in solids? *Journal of Physics C: Solid State Physics*, 6(22):L422–L426, November 1973. (Cited page 20.)
- [113] Daniel S. Marcus, Tracy H. Wang, Jamie Parker, John G. Csernansky, John C. Morris, and Randy L. Buckner. Open access series of imaging studies (OASIS): Cross-sectional MRI data in young, middle aged, nondemented, and demented older adults. *Journal of Cognitive Neuroscience*, 19(9):498–507, September 2007. (Cited page 69.)
- [114] Anthony Marmarou, Angelo L. Maset, John D. Ward, Sung Choi, Danny Brooks, Harry A. Lutz, Richard J. Moulton, J. Paul Muizelaar, Antonio Desalles, and Harold F. Young. Contribution of CSF and vascular factors to elevation of ICP in severely head-injured patients. *Journal of Neurosurgery*, 66(6):883–890, June 1987. (Cited page 6.)
- [115] Anthony Marmarou, Kenneth Shulman, and James Lamorgese. Compartmental analysis of compliance and outflow resistance of the cerebrospinal fluid system. *Journal of Neurosurgery*, 43(5):523–534, November 1975. (Cited page 18.)
- [116] Anthony Marmarou, Harold F. Young, Gunes A. Aygok, Satoshi Sawauchi, Osamu Tsuji, Takuji Yamamoto, and Jana Dunbar. Diagnosis and management of idiopathic normal-pressure hydrocephalus: a prospective study in 151 patients. *Journal of Neurosurgery*, 102(6):987–997, June 2005. (Cited pages 6 and 20.)

- [117] Mitsunori Matsumae, Ron Kikinis, István Mórocz, Antonio V. Lorenzo, Marilyn S. Albert, Peter MCL. Black, and Ferenc A. Jolesz. Intracranial compartment volumes in patients with enlarged ventricles assessed by magnetic resonance-based image processing. *Journal of Neurosurgery*, 84(6):972–981, June 1996. (Cited pages 17, 29, 44, and 45.)
- [118] Mitsunori Matsumae, Ron Kikinis, István Mórocz, Antonio V. Lorenzo, Tamás Sándor, Marilyn Albert, Peter McL. Black, and Ferenc A. Jolesz. Age-related changes in intracranial compartment volume normal adults assessed by magnetic resonance imaging. *Journal of Neurosurgery*, 84(6):982–991, June 1996. (Cited page 17.)
- [119] T. Meindl, S. Wirth, S. Weckbach, O. Dietrich, M. Reiser, and S. O. Schoenberg. Magnetic resonance imaging of the cervical spine: comparison of 2D T2-weighted turbo spin echo, 2D T2*-weighted gradient-recalled echo and 3D T2-weighted variable flip-angle turbo spin echo sequences. *European Radiology*, 19(3):713–721, March 2009. (Cited page 22.)
- [120] William Mestrezat. *Le liquide céphalo-rachidien normal et pathologique: valeur clinique de l'examen chimique*. PhD thesis, Université de Montpellier, Faculté de Médecine, 1911. (Cited page 12.)
- [121] Raul D. Millán, Laura Dempere-Marco, Jose M. Pozo, Juan R. Cebal, and Alejandro F. Frangi. Morphological characterization of intracranial aneurysms using 3-D moment invariants. *IEEE Transactions on Medical Imaging*, 26(9):1270–1282, September 2007. (Cited page 65.)
- [122] Sanae Miri, Nicolas Passat, and Jean-Paul Armspach. Topology-preserving discrete deformable model: Application to multi-segmentation of brain MRI. In *Proceedings of the 3rd International Conference on Image and Signal Processing (ICISP 2008), Cherbourg-Octeville, France, July 1–3, 2008*, volume 5099 of *Lecture Notes in Computer Science*, pages 67–75, Heidelberg, 2008. Springer-Verlag. (Cited page 30.)
- [123] Alexander Monro. *Observations on the structure and functions of the nervous system*. Creech & Johnson, Edinburgh, 1783. (Cited page 5.)
- [124] Bénédicte Mortamet, Donglin Zeng, Guido Gerig, Marcel Prastawa, and Elizabeth Bullitt. Effects of healthy aging measured by intracranial compartment volumes using a designed MR brain database. In James S. Duncan and Guido Gerig, editors, *Proceedings of the 8th International Conference on Medical Image*

- Computing and Computer-Assisted Intervention (MICCAI 2005)*, Palm Springs, CA, USA, October 26–29, 2005, volume 3749 of *Lecture Notes On Computer Science*, pages 383–391, Heidelberg, 2005. Springer-Verlag. (Cited page 17.)
- [125] Charles R. Noback, Norman L. Strominger, Robert J. Demarest, and David A. Ruggiero. *The human nervous system: Structure and function*. Humana Press, Totowa, New Jersey, 6th edition, 2005. ISBN 978-1-5882-9039-7. (Cited pages 11, 16, and 17.)
- [126] Jacques Noterman. Petite histoire de la circulation du LCR et du traitement de l'hydrocéphalie. *Revue Médicale de Bruxelles*, 28(2):131–136, April 2007. (Cited page 11.)
- [127] John E.A. O'Connell. The vascular factor in intracranial pressure and the maintenance of the cerebrospinal fluid. *Brain*, 66(3):204–228, September 1943. (Cited pages 13 and 18.)
- [128] Erik Odeblad and Gunnar Lindström. Some preliminary observations on the proton magnetic resonance in biological samples. *Acta Radiologica*, 43: 469–476, August 1955. (Cited page 13.)
- [129] Regis Olry. Short history of vascular injections, with special reference to the heart vessels. *Journal of International Society of Plastination*, 13(1):7–11, June 1998. (Cited page 11.)
- [130] A. O. Olukoga, J. Bolodeoku, and D. Donaldson. Origins of cerebrospinal fluid analysis in clinical diagnosis. *Journal of Clinical Pathology*, 50(3):187–192, March 1997. (Cited pages 11, 12, and 17.)
- [131] Darko Orešković and Marijan Klarica. The formation of cerebrospinal fluid: Nearly a hundred years of interpretations and misinterpretations. *Brain Research Reviews*, 64(2):241–262, September 2010. (Cited page 18.)
- [132] Darko Orešković and Marijan Klarica. Development of hydrocephalus and classical hypothesis of cerebrospinal fluid hydrodynamics: Facts and illusions. *Progress in Neurobiology*, 94(3):238–258, August 2011. (Cited page 18.)
- [133] B. K. Oowler, K. C. Fong, and Z. Czosnyka. Importance of ICP monitoring in the investigation of CSF circulation disorders. *British Journal of Neurosurgery*, 15(5):439–440, October 2001. (Cited page 6.)

- [134] M. Paldino, A.Y. Mogilner, and M.S. Tenner. Intracranial hypotension syndrome: a comprehensive review. *Neurosurgical Focus*, 15(6):ECP2, December 2003. (Cited page 6.)
- [135] W. M. Palm, R. Walchenbach, B. Bruinsma, F. Admiraal-Behloul, H. A. M. Middelkoop, L. J. Launer, J. van der Grond, and M. A. van Buchem. Intracranial compartment volumes in normal pressure hydrocephalus: Volumetric assessment versus outcome. *American Journal of Neuroradiology*, 27(1):76–79, January 2006. (Cited pages 29, 44, and 45.)
- [136] Gabriel Peyré, Mickaël Péchaud, Renaud Keriven, and Laurent D. Cohen. Geodesic methods in computer vision and graphics. *Foundations and Trends in Computer Graphics and Vision*, 5(3–4):197–397, March 2010. (Cited page 79.)
- [137] Ian Piper. Head injury. Physiology and management of severe closed injury. Chapter 6, pages 101–120. Chapman & Hall, London, 1997. ISBN 978-0-4125-8540-1. (Cited page 5.)
- [138] E. Purcell, H. Torrey, and R. Pound. Resonance absorption by nuclear magnetic moments in a solid. *Physical Review*, 69(1–2):37–38, January 1946. (Cited page 13.)
- [139] Heinrich I. Quincke. *Die Technik der Lumbalpunktion*. Urban & Schwarzenberg, Berlin & Vienna, 1891. (Cited page 12.)
- [140] R Development Core Team. *R: A language and environment for statistical computing*. R Foundation for Statistical Computing, Vienna, 2011. ISBN 3-900051-07-0. (Cited pages 44 and 69.)
- [141] H. Raboel, J. Bartek, Jr., M. Andresen, B.M. Bellander, and B. Romner. Intracranial pressure monitoring: invasive versus non-invasive methods – a review. *Critical Care Research and Practice*, vol. 2012, March 2012. (Cited page 6.)
- [142] Harold L. Rekate. The definition and classification of hydrocephalus: a personal recommendation to stimulate debate. *Cerebrospinal Fluid Research*, 5:2, January 2008. (Cited page 18.)
- [143] Harold L. Rekate. A consensus on the classification of hydrocephalus: its utility in the assessment of abnormalities of cerebrospinal fluid dynamics. *Child’s Nervous System*, 27(10):1535–1541, October 2011. (Cited page 31.)

- [144] Harold L. Rekate, Trimurti D. Nadkarni, and Donna Wallace. The importance of the cortical subarachnoid space in understanding hydrocephalus. *Journal of Neurosurgery: Pediatrics*, 2(1):1–11, July 2008. (Cited page 6.)
- [145] Maryam E. Rettmann, Duygu Tosun, Xiaodong Tao, Susan M. Resnick, and Jerry L. Prince. Program for assisted labeling of sulcal regions (PALS): Description and reliability. *NeuroImage*, 24(2):398–416, January 2005. (Cited pages 53 and 54.)
- [146] Wilhelm C. Röntgen. Über eine Neue Art von Strahlen: Vorläufige Mitteilung. *Sitzungs Berichte der Physikalisch-Medizinischen Gesellschaft in Würzburg*, 137: 132–141, 1895. (Cited page 13.)
- [147] Jamie B. Rosenberg, Ariel L. Shiloh, Richard H. Savel, and Lewis A. Eisen. Non-invasive methods of estimating intracranial pressure. *Neurocritical Care*, 15(3):599–608, December 2011. (Cited page 6.)
- [148] Andrea Rueda, Oscar Acosta, Michel Couprie, Pierrick Bourgeat, Jurgen Fripp, Nicholas Dowson, Eduardo Romero, and Olivier Salvado. Topology-corrected segmentation and local intensity estimates for improved partial volume classification of brain cortex in MRI. *Journal of Neuroscience Methods*, 188(2):305–315, May 2010. (Cited page 30.)
- [149] Toyofumi Saito and Jun-Ichiro Toriwaki. New algorithms for Euclidean distance transformation on an N-dimensional digitized picture with applications. *Pattern Recognition*, 27(11):1551–1565, November 1994. (Cited page 32.)
- [150] Laurent Sakka, Guillaume Coll, and Jean Chazal. Anatomy and physiology of cerebrospinal fluid. *European Annals of Otorhinolaryngology, Head and Neck Diseases*, 128(6):309–316, December 2011. (Cited pages 11, 17, and 18.)
- [151] Yoshinobu Sato, Shin Nakajima, Hideki Atsumi, Thomas Koller, Guido Gerig, and Shigeyuki Yoshida. Three-dimensional multi-scale line filter for segmentation and visualization of curvilinear structures in medical images. *Medical Image Analysis*, 2(2):143–168, June 1998. (Cited pages 37, 38, and 39.)
- [152] Wouter I. Schievink. Spontaneous spinal cerebrospinal fluid leaks and intracranial hypotension. *JAMA*, 295(19):2286–2296, May 2006. (Cited page 5.)
- [153] Johannes Schindelin, Ignacio Arganda-Carreras, Erwin Frise, Verena Kaynig, Mark Longair, Tobias Pietzsch, Stephan Preibisch, Curtis Rueden, Stephan Saalfeld, Benjamin Schmid, Jean-Yves Tinevez, Daniel James White, Volker

- Hartenstein, Kevin Eliceiri, Pavel Tomancak, and Albert Cardona. Fiji: an open-source platform for biological-image analysis. *Nature Methods*, 9(7):676–682, June 2012. (Cited pages 42 and 60.)
- [154] Florent Ségonne. *Segmentation of medical images under topological constraints*. PhD thesis, Massachusetts Institute of Technology, Cambridge MA, USA, 2005. (Cited page 30.)
- [155] James A. Sethian. *Level set methods and fast marching methods: Evolving interfaces in computational geometry, fluid mechanics, computer vision, and materials science*. Cambridge University Press, Cambridge, 2nd edition, 1999. ISBN 978-0-5216-4557-7. (Cited pages 38, 43, 81, and 83.)
- [156] Mehmet Sezgin and Bülent Sankur. Survey over image thresholding techniques and quantitative performance evaluation. *Journal of Electronic Imaging*, 13(1):146–165, January 2004. (Cited page 32.)
- [157] Linda G. Shapiro and George C. Stockman. *Computer vision*. Prentice-Hall, Upper Saddle River, NJ, 2001. ISBN 978-0-1303-0796-5. (Cited page 32.)
- [158] David Shprecher, Jason Schwalb, and Roger Kurlan. Normal pressure hydrocephalus: Diagnosis and treatment. *Current Neurology and Neuroscience Reports*, 8(5):371–376, September 2008. (Cited page 20.)
- [159] Sigurdur Sigurdsson, Thor Aspelund, Lars Forsberg, Jesper Fredriksson, Olafur Kjartansson, Bryndis Oskarsdottir, Palmi V. Jonsson, Gudny Eiriksdottir, Tamara B. Harris, Alex Zijdenbos, Mark A. van Buchem, Lenore J. Launer, and Vilmundur Gudnason. Brain tissue volumes in the general population of the elderly: The AGES-Reykjavik study. *NeuroImage*, 59(4):3862–3870, February 2012. (Cited page 17.)
- [160] Janina Skipor and Jean-Claude Thiery. The choroid plexus – cerebrospinal fluid system: Undervaluated pathway of neuroendocrine signaling into the brain. *Acta Neurobiologiae Experimentalis (Warsaw)*, 68(3):414–428, 2008. (Cited page 17.)
- [161] Alan Smillie, Ian Sobey, and Zoltan Molnar. A hydro-elastic model of hydrocephalus. *Journal of Fluid Mechanics*, 539:417–443, September 2005. (Cited page 99.)
- [162] Travis B. Smith and Krishna S. Nayak. MRI artifacts and correction strategies. *Imaging in Medicine*, 2(4):445–457, August 2010. (Cited page 30.)

- [163] D. Soler, T. Cox, P. Bullock, D. M. Calver, and R. O. Robinson. Diagnosis and management of benign intracranial hypertension. *Archives of Disease in Childhood*, 78(1):89–94, January 1998. (Cited page 5.)
- [164] John T. Sullivan, Sharon Grouper, Matthew T. Walker, Todd B. Parrish, Robert J. McCarthy, and Cynthia A. Wong. Lumbosacral cerebrospinal fluid volume in humans using three-dimensional magnetic resonance imaging. *International Anesthesia Research Society*, 103(5):1306–1310, November 2006. (Cited page 29.)
- [165] Emanuel Swedenborg. *The brain, considered anatomical, physiological and philosophically*, volume 1: The cerebrum and its parts. James Speirs, London, 1882. (Cited page 11.)
- [166] Olena Tankyevych, Hughes Talbot, Petr Dokladál, and Nicolas Passat. Direction-adaptive grey-level morphology. Application to 3D vascular brain imaging. In *Proceedings of the 16th IEEE International Conference on Image Processing (ICIP'09)*, Cairo, Egypt, November 7–10, 2009, pages 2261–2264, Washington, DC, USA, 2009. IEEE Computer Society Press. (Cited page 37.)
- [167] Nitin K. Tanna, Mark I. Kohn, David N. Horwich, Paul R. Jolles, Robert A. Zimmerman, Wayne M. Alves, and Abass Alavi. Analysis of brain and cerebrospinal fluid volumes with MR imaging: impact on PET data correction for atrophy. Part II. aging and alzheimer dementia. *Radiology*, 178(1):123–130, January 1991. (Cited pages 17, 29, 44, and 45.)
- [168] Xiaodong Tao, Xiao Han, Maryam E. Rettmann, Jerry L. Prince, and Christos Davatzikos. Statistical study on cortical sulci of human brains. In *Proceedings of the 17th International Conference on Information Processing in Medical Imaging (IPMI 2001)*, Davis, CA, USA, June 18–22, 2001, volume 2082 of *Lecture Notes in Computer Science*, pages 475–487, Heidelberg, 2001. Springer-Verlag. (Cited page 62.)
- [169] G. M. Teasdale, R. Grant, B. Condon, J. Patterson, A. Lawrence, D. M. Hadley, and D. Wyper. Intracranial CSF volumes: Natural variations and physiological changes measured by MRI. In Fabian Isamat, Antony Jefferson, Friedrich Loew, and Lindsay Symon, editors, *Proceedings of the 8th European Congress of Neurosurgery, Barcelona, Spain, September 6–11, 1987*, volume 42 of *Acta Neurochirurgica Supplementum*, pages 230–235, Vienna, 1988. Springer. (Cited page 17.)

- [170] Bertrand Thirion, Guillaume Flandin, Philippe Pinel, Alexis Roche, Philippe Ciuciu, and Jean-Baptiste Poline. Dealing with the shortcomings of spatial normalization: Multi-subject parcellation of fMRI datasets. *Human Brain Mapping*, 27(8):678–693, August 2006. (Cited page 79.)
- [171] Duygu Tosun, Maryam E. Rettmann, Xiao Han, Xiaodong Tao, Chenyang Xu, Susan M. Resnick, Dzung Pham, and Jerry L. Prince. Cortical surface segmentation and mapping. *NeuroImage*, 23(Suppl. 1):S108–S118, 2004. (Cited pages 53 and 54.)
- [172] Wen-Hsiang Tsai. Moment-preserving thresholding: A new approach. *Computer Vision, Graphics, and Image Processing*, 29(3):377–393, March 1985. (Cited page 32.)
- [173] A. Tsunoda, H. Mitsuoka, K. Sato, and S. Kanayama. A quantitative index of intracranial cerebrospinal fluid distribution in normal pressure hydrocephalus using an MRI-based processing technique. *Neuroradiology*, 42(6):424–429, June 2000. (Cited pages 29, 44, and 45.)
- [174] R. Shane Tubbs, Payman Vahedi, Marios Loukas, Mohammadali M. Shoja, and Aaron A. Cohen-Gadol. Hubert von Luschka (1820–1875): his life, discoveries, and contributions to our understanding of the nervous system. *Journal of Neurosurgery*, 114(1):268–272, January 2011. (Cited page 12.)
- [175] J. A. L. Vanneste. Diagnosis and management of normal-pressure hydrocephalus. *Journal of Neurology*, 247(1):5–14, January 2000. (Cited pages 6 and 20.)
- [176] B. Venkatesh, P. Scott, and M. Ziegenfuss. Cerebrospinal fluid in critical illness. *Critical Care and Resuscitation*, 2(1):42–54, March 2000. (Cited page 17.)
- [177] Andreas Vesalius. *De humani corporis fabrica libri septem*. Johannes Oporinus, Basel, 1543. (Cited pages 11 and 12.)
- [178] Renée Veysseyre. *Statistiques et probabilités pour l'ingénieur*. Aide-mémoire. Dunod, Paris, 2^e edition, 2006. (Cited page 44.)
- [179] Luc Vincent. Morphological grayscale reconstruction in image analysis: Applications and efficient algorithms. *IEEE Transactions on Image Processing*, 2(2):176–201, January 1993. (Cited pages 37, 38, and 40.)

- [180] Mark E. Wagshul, Per K. Eide, and Joseph R. Madsen. The pulsating brain: A review of experimental and clinical studies of intracranial pulsatility. *Fluids and Barriers of the CNS*, 8(1):5, January 2011. (Cited page 18.)
- [181] Wayne Wakeland and Brahm Goldstein. A review of physiological simulation models of intracranial pressure dynamics. *Computers in Biology and Medicine*, 38(9):1024–1041, September 2008. (Cited page 99.)
- [182] Nicolas Wiest-Daesslé, Sylvain Prima, Pierrick Coupé, Sean Patrick Morrissey, and Christian Barillot. Rician noise removal by non-local means filtering for low signal-to-noise ratio MRI: Applications to DT-MRI. In *Proceedings of the 11th International Conference on Medical Image Computing and Computer-Assisted Intervention (MICCAI 2008)*, New York, NY, USA, September 6–10, 2008, volume 5242 of *Lecture Notes in Computer Science*, pages 171–179, Berlin, Heidelberg, 2008. Springer-Verlag. (Cited page 30.)
- [183] Kathleen P. Wilkie, Gurjit Nagra, and Miles Johnston. A mathematical analysis of physiological and molecular mechanisms that modulate pressure gradients and facilitate ventricular expansion in hydrocephalus. *International Journal of Numerical Analysis and Modeling, Series B*, 3(1):65–81, 2012. (Cited page 99.)
- [184] A. Wählin, K. Ambarki, R. Birgander, N. Alperin, J. Malm, and A. Eklund. Assessment of craniospinal pressure-volume indices. *American Journal of Neuroradiology*, 31(9):1645–1650, October 2010. (Cited page 6.)
- [185] Roni Yagel, Daniel Cohen, and Arie Kaufman. Discrete ray tracing. *IEEE Computer Graphics and Applications*, 12(5):19–28, September 1992. (Cited page 89.)
- [186] M. Yoshihara, A. Tsunoda, K. Sato, S. Kanayama, and A. Calderon. Differential diagnosis of NPH and brain atrophy assessed by measurement of intracranial and ventricular CSF volume with 3D FASE MRI. In Anthony Marmarou, Ross Bullock, Cees Avezaat, Alexander Baethmann, Donald Becker, Mario Brock, Julian Hoff, Hajime Nagai, Hans-J. Reulen, and Graham Teasdale, editors, *Intracranial Pressure and Neuromonitoring in Brain Injury*, volume 71 of *Acta Neurochirurgica Supplements*, pages 371–374. Springer, Vienna, 1998. (Cited pages 29, 44, and 45.)
- [187] Hyuk Jin Yun, Kiho Im, Jin-Ju Yang, Uicheul Yoon, and Jong-Min Lee. Au-

tomated sulcal depth measurement on cortical surface reflecting geometrical properties of sulci. *PLoS ONE*, 8(2):e55977, February 2013. (Cited page 62.)

- [188] G. W. Zack, W. E. Rogers, and S. A. Latt. Automatic measurement of sister chromatid exchange frequency. *Journal of Histochemistry and Cytochemistry*, 25(7):741–753, July 1977. (Cited page 32.)

PUBLICATIONS

Material from this dissertation was already presented in the following publications:

Journals

- [1] J. Hodel, P. Besson, A. Rahmouni, E. Petit, A. Lebret, B. Grandjacques, O. Outteryck, M.A. Benadjaoud, A. Maraval, A. Luciani, J.-P. Pruvo, P. Decq, X. Leclerc. 3D mapping of cerebrospinal fluid local volume changes in patients with hydrocephalus treated by surgery: preliminary study. *European Radiology* **24**(1):136–142, 2014.
- [2] A. Lebret, J. Hodel, A. Rahmouni, P. Decq, E. Petit. Cerebrospinal fluid volume analysis for hydrocephalus diagnosis and clinical research. *Computerized Medical Imaging and Graphics* **37**(3):224–233, 2013.
- [3] J. Hodel, A. Lebret, E. Petit, X. Leclerc, M. Zins, A. Vignaud, P. Decq, A. Rahmouni. Imaging of the entire cerebrospinal fluid volume with a multistation 3D SPACE MR sequence : feasibility study in patients with hydrocephalus. *European Radiology* **23**(6):1450–1458, 2013.

International conferences

- [4] A. Lebret, Y. Kenmochi, J. Hodel, A. Rahmouni, P. Decq, E. Petit. Relief map of the upper cortical subarachnoid space. In *Proceedings of the 27th International Congress and Exhibition on Computer Assisted Radiology and Surgery (CARS 2013), Heidelberg, Germany, June 26–29, 2013*, volume 8(Suppl 1), pages S282–S284, Heidelberg, 2013, Springer.
- [5] A. Lebret, E. Petit, B. Durning, J. Hodel, A. Rahmouni, P. Decq. Quantification of the cerebrospinal fluid from a new whole body MRI sequence. In *Proceedings of SPIE Medical Imaging 2012 : Computer-Aided Diagnosis, San Diego, CA, USA, February 04–09, 2012*, volume 8315, pages 83153H–83153H–7, 2012.